Dynamical measurements of the Spin Hall angle

Dissertation

zur Erlangung des Doktorgrades

der Naturwissenschaften (Dr.rer.nat)

der Fakultät für Physik

der Universität Regensburg

vorgelegt von

Oleksandr Talalaevskyy

aus Kiew

März 2017

Contents

Introduction

Spintronics is a relatively new research field emerged in last two decades. This field emphasizes on the spin degree of freedom of the electron and its interaction with electrical and magnetic fields. The historical backgrounds of the field started in year 1924, when Ellet and Wood[1] studied the degree of polarization of mercury vapor fluorescence. They discovered that the degree of polarization depends strongly on the orientation of the experimental setup with respect to magnetic field of the Earth. The observed effect was the Hanle effect. The fluorescence was depolarized by the Earth´s transverse magnetic field. Later these results were explained by Hanle. This was followed by the work of Brossel and Kastler[2] who created a non-equilibrium distribution of angular magnetic moments by optical excitation, manipulated it by applying a magnetic field and measured the intensity of the luminescence polarization. In 1936 Nevill Mott built his two current model, that explained the high resistivity of ferromagnetic metals. The conductivity was expressed as a superposition of two different contributions each of them corresponded to an opposite spin direction. With this, Mott showed a possibility to manipulate the transport properties with magnetism.

Despite the concept was already known for a long time, the new era of this field started only recently. Significant progress in technology of nanofabrication allowed producing structures where all "spin based" effects become much easier to observe. Here we refer to the 2-D (thin films) and 1-D (nanodots) structures. The first big "jump" in this research area was triggered by discovery of Giant magnetoresistance**(**GMR) in 1988. Albert Fert and Peter Grünberg found out that the electrical resistance of a trilayer (Ferromagnet\Normal metal\Ferromagnet) strongly depends on the magnetization orientation. If both layers are magnetized parallel to each other, the resistance of the trilayer is much smaller than in case when they are magnetized antiparallel. This effect found the application in computer hard drives and magnetic random access memory (MRAM). The efficiency of the magneto resistance is defined as difference between maximum and minimum resistance of the trilayer divided by the maximum resistance. Another effect- tunnel magnetoresistance (TMR) was found by Moodera[3] and simultaneously by Miyazaki[4] in 1995. The structure for TMR elements looks very similar to the structure of GMR. TMR requires a trilayer (Ferromagnet\Insulator\Ferromagnet). These trilayers are called magnetic tunnel junctions (MTJ) and have a magnetoresistance efficiency much higher than GMR structures. In TMR there is no direct current flow through the structure because of the insulating layer. However, there is a tunneling effect and the probability of tunneling of the electron strongly depends on

its spin. So if the current is injected into a first magnetic layer of the trilayer we can get almost 100 percent spin polarized current (spin current) in the second magnetic layer. Nowadays the most effective „spin polarizes“ are MTJs with MgO insulating layers. Another interesting concept is that of a “pure” spin current. One way to create a pure spin current is the Spin Hall (SHE) effect which was observed first by Kato[5] and Wunderlich[6] in 2004. The physics of the SHE is the following: If we pass an electrical current through a metal with large spin-orbit coupling, the electrons with opposite spins deflect in opposite directions. Thus, a transverse spin current is created. The most remarkable feature for further applications is the fact that SHE creates a spin current without a charge current (pure spin current). The carrier of the spin is an electron, but if the electrons are moving in opposite directions the resulting charge current is zero. The Onsager relations show that there should be an effect reciprocal to SHE. Indeed, the Inverse spin Hall effect (ISHE) was observed in 2006 separately by Saitoh[7], Zhao[8] and Valenzuela[9]. In the ISHE a spin current creates a transverse charge current. In order to detect both effects a ferromagnetic (FM) layer should be brought in contact with a metal where the current flows. In case of SHE the spin current flows into the FM providing an extra torque on the magnetization vector. Depending on the electrical current polarity the provided torque can either increase or decrease the amplitude of the magnetization precession which means it can vary the Gilbert damping parameter. A lot of experiments showed successful manipulation of the damping parameter[10 11]. In most cases platinum (Pt) was used as NM layer due to its large spin-orbit coupling. One of the materials that is used as a ferrimagnetic layer is Yttrium-iron-garnet ($Y_3Fe_5O_{12}$) (YIG). YIG is one of the most widely used materials for studying high frequency magnetization dynamics due to its extremely low Gilbert damping parameter, which can reach values as low as $5 \cdot 10^{-5}$ for YIG spheres[12]. Its high Curie temperature and high chemical stability[13] makes the material attractive in addition to its interesting magnetic properties. Consequently the material is used for building delay lines, RF filters, attenuators, resonators, Y-junctions and other high frequency devices. The spin wave (SW) propagation in YIG allows transporting the information without transport of the electrical current. Kajiwara et al[14] demonstrated successful transport of the signal for a distance of 1 mm via the SWs and successful conversion of this signal into a voltage via spin pumping. This can be potentially interesting for the computer applications. Studying SW propagation in YIG films and in ultra-thin YIG layers has become interesting lately since high quality ultra-thin YIG films have only become available recently using standard deposition techniques such as pulsed layer deposition (PLD)[15 16 17 18 19 20] or sputter deposition[21 22 23]. In this PhD thesis we perform a broad study of magnetic properties of thin sputtered YIG films.

The first chapter is dedicated to the physical principles of ferromagnetism, magnetization dynamics and ferromagnetic resonance (FMR). From postulation of the Landau-Lifshitz equation we derive the

equilibrium condition for the magnetization vector, the expression for the magnetic susceptibility tensor and equations for the eigenfrequencies of a magnetic ellipsoid. A phenomenological explanation of relaxation mechanisms in a ferromagnetic body is provided. The second chapter is dedicated to SW propagation in thin magnetic films. The dispersion relation for Damon-Eschbach (DE) and other modes is derived from Maxwell´s equations. The third chapter is dedicated to the theory of SHE, ISHE, and spin pumping. The physical principles of these effects are described. We derive relations for the spin currents through the ferromagnetic/normal metal interface and describe its influence on the Gilbert damping parameter. In the fourth chapter we give a detailed description of the experimental setups and methods that were used for sample preparation and characterization. Chapter five is dedicated to the experimental results. The characterization of thin sputtered YIG films starts with structural analysis. X-ray reflectivity and atom force microscopy (AFM) measurements are performed to characterize the thickness and the surface roughness of the grown films. Thereafter, we perform the magnetic characterization of our samples. We determine the Gilbert damping, saturation magnetization and magnetic anisotropy of the YIG films. Further we study the propagation of the SWs and their mode structure in microstructured YIG stripes. The SW attenuation length is extracted from these measurements. SW attenuation length characterizes efficiency of magnetic material as a media for the SW transport. Furthermore, we investigate the spin pumping at the interface between YIG and different metals. The milestone of the experimental part is the measurement of the SHE in YIG/Platinum interfaces and calculation of the spin Hall angle. The thesis is summarized with the conclusion.

1. Magnetization Dynamics

1.1 Ferromagnetism

All ferromagnetic materials possess a magnetic moment even without magnetic bias field. This is called spontaneous magnetization. Spontaneous magnetization distinguishes ferromagnets from paramagnets that could be magnetized by external magnetic field. This happens when magnetic moments of the electrons are ordered in one direction. The magnetic moment of the electron consists of the electrons moment (spin) and orbital moment. According to Pauli principle all the internal electron orbitals have two electrons with opposite spin in each energy state. That means that these electrons can not contribute to ferromagnetism. Only the electrons from the internal partially filled shells can contribute to the ferromagnetism. The reason for spontaneous magnetization is the exchange energy. As we know from quantum mechanics the wave functions of two electrons depends on the relative orientation of their spins. For the electron system it can also be defined as the energy released when two or more electrons exchange their positions. If two electrons with parallel spins are placed in the same state, this state will be forbidden by the Pauli principle. One can imagine an "extra force" acting on the electrons and trying to push the electrons away from each other. The operator of the exchange energy H_{ex} of two particles with spins S_1 and S_2 can be written as follows:

$$H_{ex} = 2\, I(r_{12})\, \vec{S}_1\, \vec{S}_2 \tag{1.1}$$

The value of the exchange integral $I(r_{12})$ decreases rapidly with the increase of distance r_{12} between the two particles. We should note that the ferromagnet order can be easily destroyed by the temperature. For ferromagnets the critical temperature is called Curie temperature. For yttrium iron garnet (Yig) the Curie temperature is 560 K. Let us consider a fully magnetized ferromagnetic at the temperature below the Curie temperature. In this case instead of every single magnetic moment one can derive the magnetization $\overrightarrow{\mathrm{M}}$ as follows:

$$\overrightarrow{\mathrm{M}} = \frac{\sum \vec{M}_{local}}{\Delta V} \tag{1.2}$$

Here $\sum \vec{M}_{local}$ is the sum of all moments of the small volume ΔV.

The magnetic induction $\vec{B}$ can be expressed as follows:

$$\vec{B} = \mu_0(\vec{H} + \overrightarrow{\mathrm{M}}) \tag{1.3}$$

The magnetic induction defined in eq. (1.3) enters the Maxwell equations and is a fundamental quantity in electrodynamics.

One of the most important tasks in magnetism is describing the motion of the magnetization vector $\vec{M}$ and its equilibrium position. The equilibrium position corresponds to the direction of the magnetization vector such that the free energy of the system is minimal. For most magnetic systems it can be described as sum of 4 components: exchange, demagnetization, anisotropy and Zeeman energy. In this case the equilibrium condition is written as follows:

$$\delta \int U_{mag}\, dV = 0 \tag{1.4}$$

$$U_{mag} = E_{ex} + E_{an} + E_{dem} + E_z \tag{1.5}$$

where U_{mag} is the total free energy. We briefly discuss all the components in the eq. (1.5). The first term is the exchange energy. It consists of uniform and non-uniform parts. The non-uniform part has spatial derivatives of magnetization.

$$E_{ex} = -\frac{1}{2}\Lambda M^2 + \frac{1}{2}\Lambda_1 \frac{\partial \vec{M}}{\partial x}\frac{\partial \vec{M}}{\partial y} \tag{1.6}$$

The values of the constants Λ and Λ_1 depend on the exchange integral from eq. (1.1)

The second term in eq. (1.5) is the anisotropy energy. In ferromagnets there are often directions, which are energetically preferred for the magnetization vector. The reason for this is the spin-orbit interaction. The most energetically favorable directions are called anisotropy axes. The rotation of the spins with respect to the lattice changes the shape of the electron clouds of the atom. As the consequence the exchange energy of the system also changes. Such anisotropy is also called magneto-crystalline. So if demagnetization and Zeeman energy contributions are excluded, the magnetization vector points along the anisotropy axis. Depending on the crystal system there can be one or more anisotropy axes. For the cubic lattice (iron) the anisotropy can be expressed as

$$E_{an,cubic} = -\frac{K_1}{2}\left(\alpha_x^4 + \alpha_y^4 + \alpha_z^4\right) \tag{1.7}$$

where K_1- first order anisotropy constant, α_x,α_y,α_z are the direction cosines $\alpha_{ijk} = \vec{M}_{ijk} / M$.

Another case is the uniaxial anisotropy. In many systems there is only one energetically favored axis.

The anisotropy of the thin film consists of the in- and out-of plane contributions and can be expressed as

$$E_{an,uni} = -K_{un}^{\perp}\,\alpha_z^2 - K_{un}^{||}\left(\frac{\vec{M}\hat{n}}{M_s}\right)^2 \tag{1.8}$$

where $K_{un}^{\perp}$ and $K_{un}^{||}$ are the in- and out-of plane anisotropy constants, $\hat{n}$ – the unit vector of the in-plane easy axis and M_s is the saturation magnetization.

The demagnetization energy comes from the stray fields created by the magnetization on the sample boundary. In order to reduce the total energy of the system the demagnetizing magnetic field is created inside the ferromagnetic body. Its direction is always opposite to the direction of the magnetization. This field influences the ferromagnetic resonance frequency. The derivation of this field and its influence on FMR is provided in subchapter 1.4.

The last term in eq. (1.5) is the Zeeman energy. Zeeman energy is the energy of the magnetic moment in the external field. Its value is just a product of the magnetization and the magnetic field.

$$E_Z = -\mu_0 \vec{H}\vec{M} \tag{1.9}$$

1.2 Landau-Lifshitz equation

The equation that describes the motion of the magnetization vector is called Landau- Lifshitz equation.

$$\frac{\partial \vec{M}}{\partial t} = -\gamma_0 \mu_0 \vec{H} \times \vec{M} \tag{1.10}$$

where $\gamma_0 = 176\ \frac{GHz}{T}$ is the electron gyromagnetic ratio and $\mu_0 = 4\pi \cdot 10^{-7}\ \frac{V\,s}{A\,m}$. Further we use the constant $\gamma = \gamma_0\mu_0 = 220000\ \frac{m}{A\,s}$ for convenience. Equation (1.10) works only for hypothetical magnetic media without dissipation. Let us consider the magnetic moment and the magnetic field as a sum of constant and variable components $\vec{H}=\vec{H}_0+\vec{h}_{\sim}$, $\vec{M}=\vec{M}_0+\vec{m}_{\sim}$. Another assumption is that the amplitudes of the variable parts are much smaller than the constant parts: $h_{\sim}<<H_0$, $m_{\sim}<<M_0$. For FMR this condition is fulfilled. Putting this equation into the Landau-Lifshitz and leaving only constant components we get

$$\vec{M}_0 \times \vec{H}_0 = 0 \tag{1.11}$$

This relation defines the equilibrium position of the vector $\vec{M}_0$. In case of an isotropic ferromagnet this vector is oriented with the magnetic field. In the first approach after the substitution explained above, the Landau-Lifshitz can be written as

$$\frac{\partial \vec{m}_\sim}{\partial t} + \gamma \vec{m}_\sim \times \vec{H}_0 = -\gamma \vec{M}_0 \times \vec{h}_\sim \tag{1.12}$$

This equation is already linear for $h_\sim$ and $m_\sim$ so it could be solved using the method of complex amplitudes. For this, the complex amplitudes should be introduced:

$$\vec{m}_\sim = \vec{m}\, e^{i\omega t} \qquad \vec{h}_\sim = \vec{h}\, e^{i\omega t} \tag{1.13}$$

where ω is the oscillation frequency. For the complex amplitudes $\vec{h}$ and $\vec{m}$ eq. (1.12) can be rewritten

$$i\omega \vec{m} + \gamma \vec{m} \times \vec{H}_0 = -\gamma \vec{M}_0 \times \vec{h} \tag{1.14}$$

Let us make a projection of eq. (1.14) on the axes in the Cartesian system. The field $\vec{H}_0$ and magnetization $\vec{M}_0$ are parallel to z-axis.

$$\begin{aligned} i\omega m_x + \gamma m_y H_0 &= \gamma M_0 h_y \\ i\omega m_y - \gamma m_x H_0 &= -\gamma M_0 h_x \\ i\omega m_z &= 0 \end{aligned} \tag{1.15}$$

Solving the equation system (1.15) we will get a relation for the magnetic susceptibility

$$\begin{aligned} m_x &= \chi h_x + i\chi_a h_y \\ m_y &= \chi h_y - i\chi_a h_x \\ m_z &= 0 \end{aligned} \tag{1.16}$$

$$\chi = \frac{\gamma \omega_H M_0}{\omega_H^2 - \omega^2} \qquad \chi_a = \frac{\gamma \omega M_0}{\omega_H^2 - \omega^2} \qquad \omega_H = \gamma H_0$$

where χ and χ_a are the symmetric and the anti-symmetric components of the susceptibility. The obtained equation (1.16) could be rewritten in the tensor form.

$$\vec{m} = \boldsymbol{\chi}\vec{h} \tag{1.17}$$

$$\boldsymbol{\chi} = \begin{pmatrix} \chi & i\,\chi_a & 0 \\ -i\,\chi_a & \chi & 0 \\ 0 & 0 & 0 \end{pmatrix}$$

The obtained solution reveals several important properties of the magnetization precession. First thing to note is that the longitudinal component of the magnetic field *h* does not cause a change of magnetization *m*. However, the transverse components h_x and h_y excite the magnetization not only in the directions parallel to themselves but also in the direction perpendicular to each other. The perpendicular components are shifted by π/2 and - π/2 which can be seen from the multipliers *i* and –*i* in tensor (1.17). As a result the tensor is non-symmetric with asymmetric components. The second important consequence of the solution of the Landau-Lifshitz equation is that the dependence of the magnetic susceptibility tensor on the magnetic field H_0 has the Lorentz line shape. In fact, for the case without dissipation these components of the tensor become infinitely large when:

$$\omega = \omega_H = \gamma H_0 \tag{1.18}$$

Relation (1.18) is a condition for ferromagnetic resonance. For any real system there is always some dissipation in the magnetic media that causes components of the susceptibility tensor (1.17) to be finite. However, relation (1.18) is still fulfilled.

1.3 Consideration of the damping. Energy dissipation mechanisms

Now to finish describing the motion of the magnetization vector, $\vec{M}$ we have to consider dissipation. There are several ways to do this. One way is to modify the Landau-Lifshitz equation by adding an extra term that corresponds to energy loss in the system:

$$\frac{\partial \vec{M}}{\partial t} = -\gamma \vec{H} \times \vec{M} + \alpha \frac{\vec{M}}{M_0} \times \frac{\partial \vec{M}}{\partial t} \tag{1.19}$$

Here α is a dissipation parameter in Gilbert form or Gilbert damping parameter. Taking the same assumptions for magnetic field and magnetization as in the non-dissipative case we get the following relation in zero approximation:

$$\vec{M}_0 \times \vec{H}_0 = 0 \tag{1.20}$$

This means that the equilibrium position of the magnetization vector $\vec{M}_0$ does not depend on the presence of damping in the system. Using the same method of complex amplitudes we linearize eq. (1.19):

$$i\omega\vec{m} + \gamma\vec{m} \times \vec{H}_0 + \frac{i\alpha\omega}{M_0}\vec{m} \times \vec{M}_0 = -\gamma\vec{M}_0 \times \vec{h} \tag{1.21}$$

Projections of eq. (1.21) on the axes in the Cartesian system bring us to following equation system:

$$i\omega m_x + \gamma m_y H_0 + \frac{i\alpha\omega}{M_0} m_y M_0 = \gamma M_0 h_y$$

$$i\omega m_y - \gamma m_x H_0 - \frac{i\alpha\omega}{M_0} m_x M_0 = -\gamma M_0 h_x \tag{1.22}$$

$$i\omega m_z = 0$$

The solution of this equation system gives us the susceptibility tensor in the same form as in eq. (1.17)

$$\boldsymbol{\chi} = \begin{pmatrix} \chi & i\ \chi_a & 0 \\ -i\ \chi_a & \chi & 0 \\ 0 & 0 & 0 \end{pmatrix} \tag{1.23}$$

But here the tensor components are already complex numbers $\chi = \chi' - i\chi''$, $\chi_a = \chi_a' - i\ \chi_a''$

$$\chi' = \frac{\gamma\omega_H M_0(\omega_H^2 - (1-\alpha^2)\omega^2)}{(\omega_H^2 - (1+\alpha^2)\omega^2)^2 + 4\alpha^2\omega^2\omega_H^2} \qquad \chi'' = \frac{\gamma\omega\alpha M_0(\omega_H^2 + (1+\alpha^2)\omega^2)}{(\omega_H^2 - (1+\alpha)\omega^2)^2 + 4\alpha^2\omega^2\omega_H^2} \tag{1.24}$$

$$\chi_a' = \frac{\gamma\omega M_0(\omega_H^2 - (1+\alpha^2)\omega^2)}{(\omega_H^2 - (1+\alpha^2)\omega^2)^2 + 4\alpha^2\omega^2\omega_H^2} \qquad \chi_a'' = \frac{2\gamma\omega_H\alpha M_0\omega^2}{(\omega_H^2 - (1+\alpha^2)\omega^2)^2 + 4\alpha^2\omega^2\omega_H^2}$$

The dependence of tensor components is shown in Fig 1.3.1. The condition of ferromagnetic resonance is $(\omega_H^2 = (1+\alpha^2)\omega^2)$.

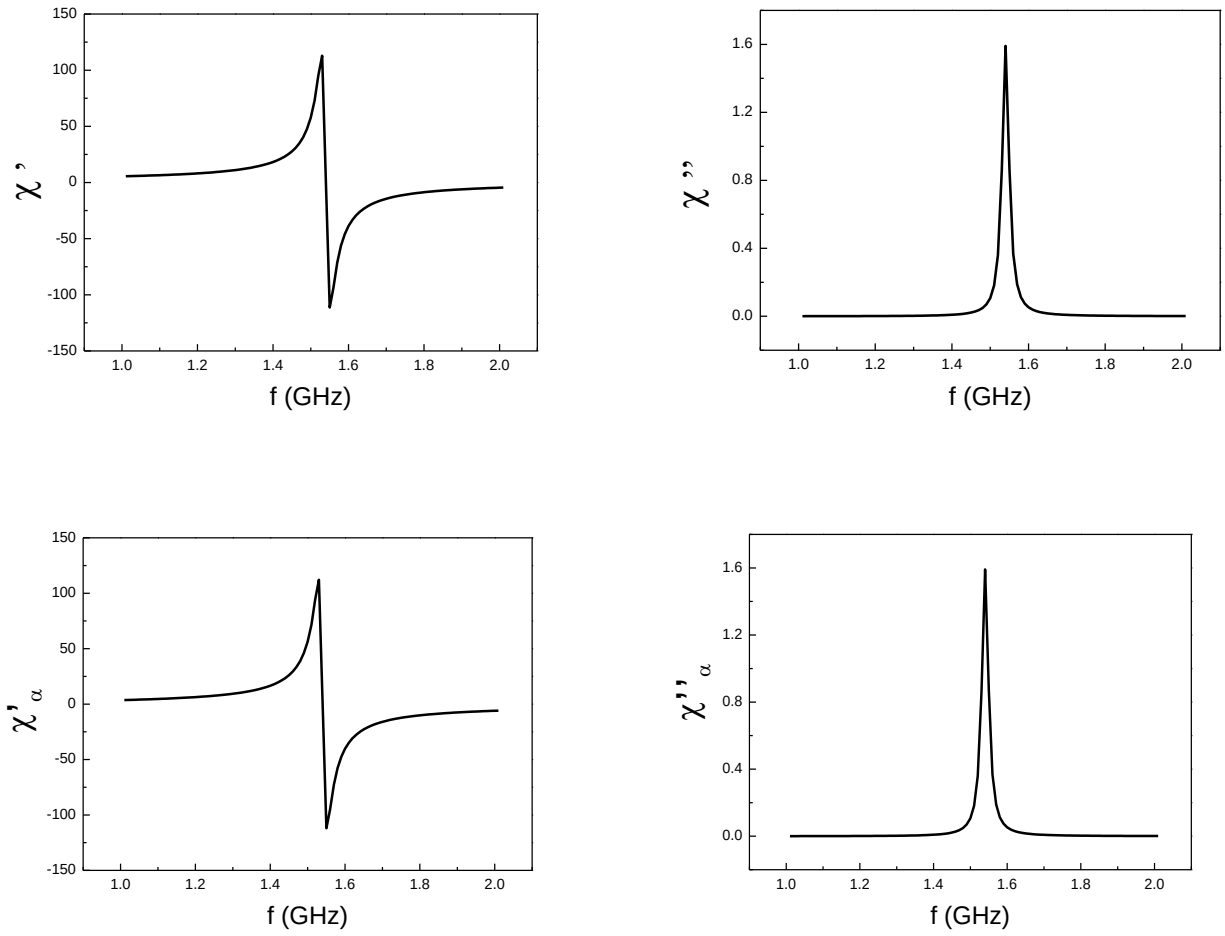

Fig 1.3.1. Real and imaginary parts of the magnetic susceptibility for a YIG sphere. $\alpha = 5 \times 10^{-5}$, $H_0 = 55$ mT, $M_s = 175$ mT.

As it is shown in eq. (1.24) at resonance the absorption has a maximum and the real part of susceptibility is equal to zero (changes sign). For small values of the Gilbert damping α, symmetric and anti-symmetric tensor components have almost the same frequency dependence.

At resonance the tensor components are equal to

$$\chi'_{res} = 0 \qquad \chi''_{res} = \frac{\gamma M_0}{2\alpha\omega} \qquad \chi'_{a\,res} = 0 \qquad \chi''_{a\,res} = \frac{\gamma M_0}{2\alpha\omega} \tag{1.25}$$

Until now we have only postulated the presence of damping in magnetically ordered systems and derived some properties of the magnetization from the Landau-Lifshitz equation, without describing the nature

and physical mechanisms of the damping. Some dissipation processes create energy redistribution inside the magnetic system i.e. new oscillations or spin waves are excited by the initial oscillation. These

processes are called spin-spin relaxation processes. The spin-spin relaxation processes are divided into 2 groups: processes that exist even in ideal crystals and processes caused by impurities or defects in the lattice. For further discussion will switch to the concept of quasi particles to simplify description of the relaxation processes. Any type of magnetic oscillation is called a magnon. The oscillation of the lattice in the solid body is called phonon. Introduction of magnons is made to simplify the description of many processes. For example the well-known process of parametric pumping can be understood much easier in quasi particles concept. The photon of the pumping wave splits into two magnons with the same energies, moving in the opposite directions. The total energy and momentum are conserved:

$$h\omega_{photon} = \quad h\omega_{mag\,1} + h\omega_{mag\,2} \qquad hk_{photon} = \quad hk_{mag\,1} + hk_{mag\,2} \tag{1.26}$$

since the momentum of the photon is zero we can write the following $k_{mag\,1} = -k_{mag\,2}$.

Coming back to the relaxation processes we should note that a magnetic system is never isolated i.e. there is energy exchange with other systems for example lattice, charge carriers or nucleus magnetic system. At the end all the energy is given to the lattice (phonons are created). That's why they are called spin-lattice relaxation processes. The picture below shows in details the possible ways of energy redistribution.

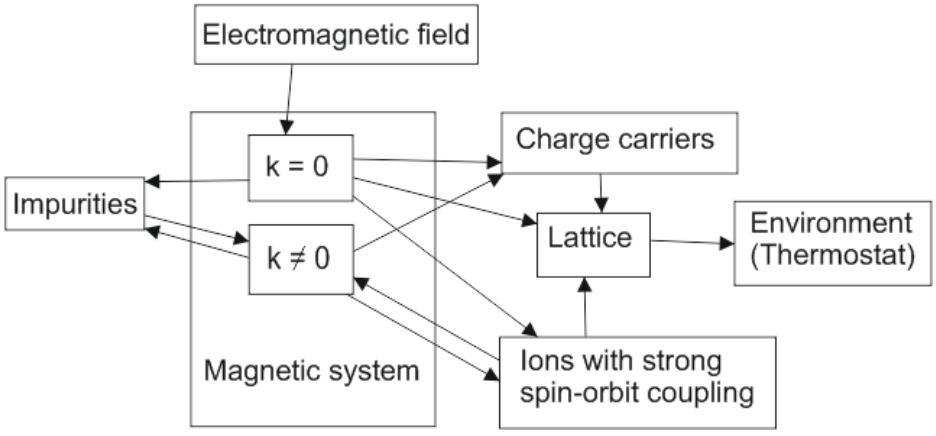

Fig 1.3.2 Energy flows between the systems in a ferromagnetic material.

There are multiple theoretical methods to study the relaxation in ferromagnets. Mostly they are: the method of coupled motion equation and the method of random transitions. The method of the coupled

motion equations is based on the fact that dissipation in the system is caused by interaction of different oscillation types. In case of spin-spin relaxation it could be the oscillations of the magnetic system. In case of spin-lattice relaxation it could be the oscillations of the lattice and magnetic system. In the zero approximation all system oscillations are considered to be independent. The solution of the motion equations returns the eigenoscillations of the system. In the first approximations these oscillations become coupled which causes the energy exchange between the different types of oscillations i.e. dissipation takes place. For the method of random transitions the quantum mechanical perturbation theory is used. The dissipation is just a transition of the system from one quantum state to another. The value of the dissipation corresponds to the "speed" or probability of these transitions. These methods are not described in details, since it requires a complicated math and is beyond the main topic of this thesis.

A brief phenomenological description of those processes that contribute to dissipation is given. The biggest contribution to the linewidth (at room temperatures for YIG) is given by the process of two magnon scattering. This is a spin-spin relaxation process caused by the inhomogeneities. The inhomogeneities could be of different nature: chemical inhomogeneities (defects in the crystal order), variations in the directions of the crystal axes (polycrystallinity), nonuniform strains (mostly caused by dislocations) and geometrical inhomogeneities (for example surface roughness). Due to strong coupling of the oscillations in different points of the ferromagnetic sample, these oscillations could not be considered independent. The coupled oscillations of the whole area between these points should be considered. Since the positions of the inhomogeneities are random, the determination of the oscillations frequencies is statistical. One can expect that the eigenfrequencies of the non-uniform area will group around the eigenfrequencies of the uniform sample. Each group will possess an almost continuous frequency spectrum. If the ferromagnet is excited by a high frequency field, this field will excite a whole group of frequencies. The linewidth of FMR will be broader by the order of the mentioned above frequencies spectrum. We can also describe this process in quasi particle concept as interaction of the magnon with the phonon. The magnon is scattered by the phonon which results in a change of the magnon momentum and energy. Another mechanism is three magnon and four magnon scattering. These spin-spin relaxation processes can take place even in the ideal crystal. The probability of such processes drops with the increase of the number of particles involved i.e. the probability of the 3 magnon scattering is higher than 4-magnon scattering. There are two types of the three magnon processes: magnon splitting and magnon confluence. The figure below illustrates the physical principal of these processes.

Fig 1.3.3 Three magnon scattering and confluence processes.

For all processes energy and momentum conservation should be fulfilled. For the splitting process of the regarded magnons with momentum $h\vec{k}_1$ and energy $h\omega_1$ the conservation law can be written as following:

$$h\omega_1 = h\omega_2 + h\omega_3 \qquad h\vec{k}_1 = h\vec{k}_2 + h\vec{k}_3 \tag{1.27}$$

for confluence

$$h\omega_1 = h\omega_3 - h\omega_2 \qquad h\vec{k}_1 = h\vec{k}_3 - h\vec{k}_2 \tag{1.28}$$

The relaxation process that results in an increase of the total amount of regarded magnons is usually called direct process. If the total amount of regarded magnons decreases the process is called reversed. The sketch for four magnon processes is illustrated below.

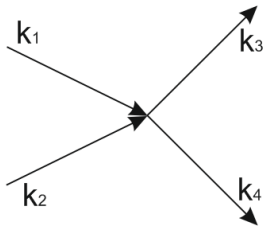

Fig 1.3.4 Four magnon process.

Generally one can see that 3 and 4-magnon processes create magnons with new frequencies in the system. This will result in an effective linewidth broadening.

1.4 FMR in thin films

Previously we described only the process in "infinitely" large ferromagnetic samples. Obviously in real life all the samples have a finite size, and this fact should be considered in order to obtain the correct solutions for the FMR frequencies and fields. The boundary conditions influence strongly the distribution of the magnetic fields inside the ferromagnetic sample. The smaller the sample is, the bigger is the influence of the shape anisotropy. A sample size, which is small compared to the wavelength of the electromagnetic field, allows us to consider the electromagnetic field to be the same as in the absence of the sample. Also, the small size allows us to use a magnetostatic approximation for the determination of the complex amplitudes of the electromagnetic field. If the sample is an ellipsoid, we can use the following magnetostatic result: The magnetic field *H* inside of the ellipsoid placed in the uniform magnetic field H_{ext} is also uniform, and can be expressed as:

$$\vec{H} = \vec{H}_{ext} + \vec{H}_M = \vec{H}_{ext} - N\vec{M} \tag{1.29}$$

Here $\vec{M}$ is the magnetization (also uniform), $\vec{H}_M$ is the demagnetizing field, *N* is the demagnetization tensor. This tensor is symmetric and has only diagonal components in the coordinate system in which the axes coincide with the axes of the ellipsoid. The components of the tensor depend only on the shape of the ellipsoid and the sum is equal to 1:

$$N_x + N_y + N_z = 1 \tag{1.30}$$

The complex amplitudes of the permanent and variable magnetic fields can be written as:

$$\vec{H}_0 = \vec{H}_{ext} - N\vec{M}_0 \tag{1.31}$$

$$\vec{h} = \vec{h}_{ext} - N\vec{m} \tag{1.32}$$

The equilibrium condition in this case is written as:

$$\vec{M}_0 \times \left(\vec{H}_{ext} - N\vec{M}_0\right) = 0 \tag{1.33}$$

Considering (1.36) the linearized equation of motion (1.22) can be written as following:

$$i\omega\vec{m} + \gamma\vec{m} \times \vec{H}_0 + \gamma(N\vec{m}) \times \vec{M}_0 + \frac{i\alpha\omega}{M_0}\vec{m} \times \vec{M}_0 = -\gamma\vec{M}_0 \times \vec{h}_{ext} \tag{1.34}$$

Here $\vec{H}_0$ is extracted from eq. (1.31). To find the solution for the eigenoscillations of the system we can assume that dissipation and the variable components of the magnetic field are equal to zero ($\alpha = 0$, h_{ext}=0). In this case eq. (1.34) can be written as

$$i\omega\vec{m} + \gamma\vec{m} \times \vec{H}_0 + \gamma(N\vec{m}) \times \vec{M}_0 = 0 \tag{1.35}$$

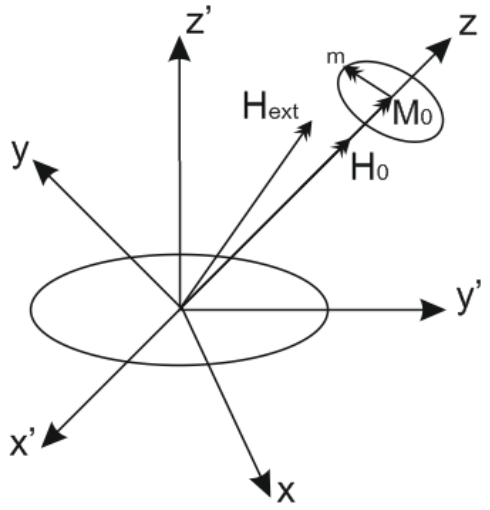

Fig 1.4.1 Axes of the coordinate system(x, y, z) and of the ellipsoid (x', y', z'). In general case they do not coincide. The axis z coincides with the direction of the field H_0.

In the coordinate system, in which the axes do not coincide with the axes of the ellipsoid (see fig 1.4.1), the tensor N has a following form:

$$N = \begin{pmatrix} N_{11} & N_{12} & N_{13} \\ N_{12} & N_{22} & N_{23} \\ N_{13} & N_{23} & N_{33} \end{pmatrix} \tag{1.36}$$

After linearization procedure of eq. (1.35) is written as following:

$$\begin{aligned} (\, i\omega + \gamma N_{12} M_0) m_x + \gamma m_y \left(H_{ext(z)} - N_{33} M_0 + N_{22} M_0\right) = 0 \\ (\, i\omega - \gamma N_{12} M_0) m_y - \gamma m_x \left(H_{ext(z)} - N_{33} M_0 + N_{11} M_0\right) = 0 \end{aligned} \tag{1.37}$$

Solving the system (1.37) one can get the expression for the eigenfrequency of the uniformly magnetized ellipsoid in the general case:

$$\omega_0^2 = (\omega_H + \gamma N_{11} M_0)(\omega_H + \gamma N_{22} M_0) - N_{12}^2 \gamma^2 M_0^2 \quad (1.38)$$

where $\omega_H = \gamma H_0 = \gamma(H_{ext(z)} - N_{33} M_0)$. So at the frequency ω_0, there is resonant energy absorption. This frequency differs from the frequency ω_H where the magnetic susceptibility has a maximum. To simplify the expression (1.38) we can rotate our coordinate system in such way that it axes will coincide with ellipsoid axes. Let us assume the film that lies in the x-y plane. The demagnetizing factors are ($N_x = 0$, $N_y = 0$, $N_z = 1$) Then the tensor will become diagonal and expression (1.38) for the film magnetized in z-direction could be written as:

$$\omega_0^2 = (\gamma H_{ext} + \gamma(N_x - N_z) M_0)\big(\gamma H_{ext} + \gamma(N_y - N_z) M_0\big) \quad (1.39)$$

Expression (1.39) is well known as Kittel formula and is often used to calculate the frequency of ferromagnetic resonance in ferromagnetic samples. Putting the values of the demagnetization factors in (1.39) we obtain the expression for the FMR frequency of the normally magnetized film:

$$\omega_0 = \gamma(H_{ext} - M_0) \quad (1.40)$$

If the film is in-plane magnetized the eq. (1.39) can be written as:

$$\omega_0^2 = (\gamma H_{ext} + \gamma(N_z - N_x) M_0)\big(\gamma H_{ext} + \gamma(N_y - N_x) M_0\big) \quad (1.41)$$

Putting the values of the demagnetization factors in eq. (1.41) we obtain the expression for the FMR frequency of the in-plane magnetized film:

$$\omega_0 = \gamma\sqrt{H_{ext}(H_{ext} + M_0)} \quad (1.42)$$

1.5 Magnetic properties of YIG

In this subchapter we briefly describe YIG since this material is the object of study in this thesis. YIG is an insulating material. The resistivity for bulk samples is about $1 \cdot 10^{12}$ Ohm·cm at room temperature. This means that electrons flowing in the YIG/metal bilayer can not enter the YIG films and will scatter from the interface. This is very important since the only spin transfer mechanism is thus spin pumping at the sample interface. YIG is also a ferrimagnetic material. In ferrimagnets the type of magnetic ordering is similar to antiferromagnet i.e. the unit cell of the material possesses magnetic moments directed in opposite directions (see fig 1.5.1). However, the resulting magnetic moment of the unit cell is not zero since the values of the opposite magnetic moments are different.

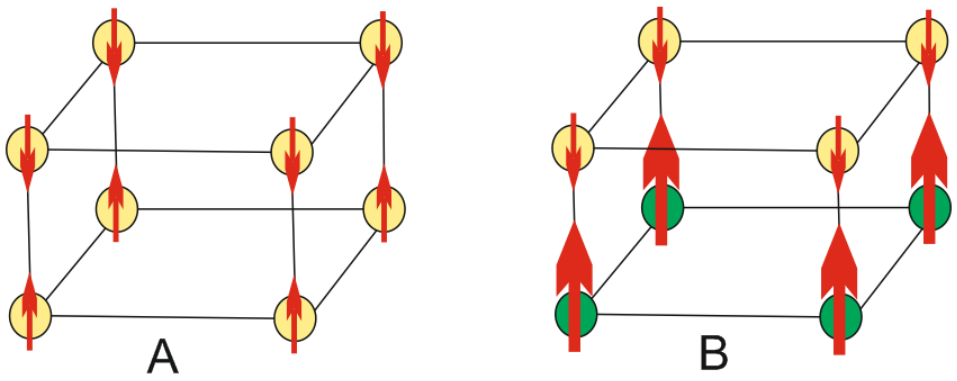

Fig 1.5.1 View of antiferromagnetic (A) and ferrimagnetic (B) ordering in a cubic unit cell. The net magnetic moment in an antiferromagnet is zero in absence of a bias field. In ferrimagnets the values of the opposite magnetic moments are different which results in a net spontaneous magnetization.

In the case of YIG the unit cell is much more complicated. Its magnetic part consists of 20 ions of Fe^{3+} which are placed in the lattice points two different of crystal lattices.12 ions placed in the tetragonal lattice points and 8 ions placed in octagonal lattice points could be separated into 2 sub-lattices with antiparallel magnetization. The exchange energy of such system can be written as follows[24]

$$E_{ex} = -\frac{1}{2}\Lambda_{11}M_1^2 - \frac{1}{2}\Lambda_{22}M_2^2 - \Lambda_{12}M_1M_2 \tag{1.43}$$

where $\Lambda_{11,}\Lambda_{22}$ and Λ_{12} are exchange parameters inside and between the sublattices.

Nevertheless, with application of a magnetic bias field the magnetization precession is the same as for ferromagnetic samples. So for the YIG film the Landau – Lifshitz equation (1.19) and all its consequences described in the previous subchapter are fulfilled. The magnetization of ferrimagnets drops with increase of temperature. Above the Curie temperature magnetic ordering disappears. For YIG the Curie temperature is about 550 K. The most important feature of YIG samples is a very small Gilbert damping parameter i.e. small FMR linewidth at high frequencies.

2. Magnetostatic spin waves

In the previous chapters we described the behavior of uniformly magnetized samples where the spin precession is uniform. That means that all the spins of the sample are oscillating at the same phase. In general the magnetization precession could be non-uniform. Such oscillations are called the spin waves or magnons in quasi-particle terms. In this chapter we derive the dispersion relations for different magnetostatic spin waves from the Maxwell equations.

2.1 Maxwell equations

The Maxwell equations could be written as follows:

$$div\ \vec{B} = 0 \qquad div\ \vec{D} = 4\pi\rho$$

$$rot\ \vec{H} - \frac{1}{c}\frac{\partial \vec{D}}{\partial t} = 4\pi J \qquad rot\ \vec{E} + \frac{1}{c}\frac{\partial \vec{B}}{\partial t} = 0 \tag{2.1}$$

Here $\vec{E}$ and $\vec{D}$ are the vectors of the electric field and electric induction, $\vec{B}$ and $\vec{H}$ are the vectors of magnetic induction and magnetic field, J and ρ are the densities of the current and charge.

Let us make the same assumption as in subchapter 1.2 that magnetic and electric fields are the sum of constant and variable components. The variable parts of the fields are changing as harmonic functions in time. Then we can make the linearization of the system (2.1) and for variable components we get the following:

$$div\ \vec{b} = 0 \qquad div\ \vec{d} = 4\pi\rho$$

$$rot\ \vec{h} - i\frac{\omega}{c}\vec{d} = 4\pi j \qquad rot\ \vec{e} + i\frac{\omega}{c}\vec{b} = 0 \tag{2.2}$$

The vectors of the fields and induction are connected with the material tensors of the magnetic permeability and the electric permittivity.

$$\vec{b} = \overleftrightarrow{\mu}\,\vec{h} \qquad \vec{d} = \overleftrightarrow{\varepsilon}\,\vec{e} \tag{2.3}$$

Putting eq. (2.3) into (2.2) we get the Maxwell equation system for magnetic and electric fields.

$$div\,\overleftrightarrow{\mu}\,\vec{h} = 0 \qquad div\,\overleftrightarrow{\varepsilon}\,\vec{e} = 4\pi\rho$$

$$rot\,\vec{h} - i\frac{\omega}{c}\overleftrightarrow{\varepsilon}\,\vec{e} = 4\pi j \qquad rot\,\vec{e} + i\frac{\omega}{c}\overleftrightarrow{\mu}\,\vec{h} = 0 \tag{2.4}$$

2.2 Magnetostatic approach and Walker equation

The magnetostatic approach is valid for spin waves with wave vectors *k* much smaller than one over the exchange length. For such waves the dipolar interaction plays the most important role. For the small wave vectors *k* ($k \equiv \frac{\omega}{c}$) we can rewrite the system (2.4) as following:

$$div\,\overleftrightarrow{\mu}\,\vec{h} = 0 \qquad rot\,\vec{h} = 0 \tag{2.5}$$

Since $rot\,\vec{h} = 0$ we can introduce a magnetic potential $h = \Delta\psi$ and rewrite eq. (2.5) as:

$$div\,\overleftrightarrow{\mu}\,\Delta\psi = 0 \tag{2.6}$$

Equation (2.6) is sometimes called the generalized Walker equation. For the uniform plane wave the magnetostatic potential has the form of a harmonic function $\psi = \psi_0\, e^{(-ik_x x - ik_y y - ik_z z)}$. Putting this into the eq. (2.6) we get

$$\mu\left(\frac{\partial^2\psi}{\partial x^2} + \frac{\partial^2\psi}{\partial y^2}\right) + \frac{\partial^2\psi}{\partial z^2} = 0 \tag{2.7}$$

In this form the equation was first written by Walker[25].

Walkers equation is very important since we can get the dispersion relations for different spin wave types from it. We have to vary the form of the potential ψ with respect to the boundary conditions of the film and magnetic fields geometry. In the following subchapters we will do this for different types of magnetostatic spin waves.

2.3 Magnetostatic volume and surface waves

One of the cases of the volume magnetostatic waves are forward volume waves (MSFVW). This case occurs when a magnetic film is magnetized normal to its surface, and the wave vector $\vec{k}$ is perpendicular to the magnetization $\vec{M}$ see Fig 2.3.1

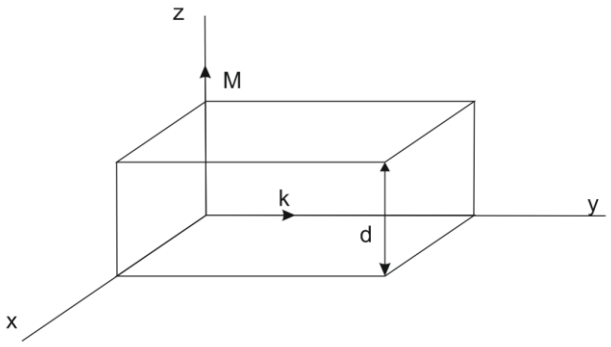

Fig 2.3.1 Geometry of magnetostatic forward volume waves. Here $\vec{M}$ is the magnetization vector, d is the thickness of the ferromagnet, $\vec{k}$ is the wave vector.

The solution of the Walker equation can be written in the following form:

$$\psi = (A\cos k_z z + B\sin k_z z)e^{-iky} \tag{2.8}$$

Putting this in the eq. (2.7) and solving[12] it, we get the dispersion relation for magnetostatic forward volume waves.

$$\omega^2 = \omega_H\left(\omega_H + \frac{\gamma M_0}{1+\frac{(n\pi)^2}{(kd)^2}}\right) \tag{2.9}$$

where *n* is a mode number.

For these waves the group velocity $v_{gr} \equiv \frac{\partial\omega}{\partial k}$ has a positive sign which means that the wave is actually propagating "forward". The frequencies for MSFVW lie in the region $\omega_H \leq \omega \leq \sqrt{\omega_H(\omega_H+\gamma M_0)}$ see fig 2.3.3

The second spin wave type is called magnetostatic backward volume waves (MSBVM) and it occurs in in-plane magnetized films see fig 2.3.2. The solution of the Walker equation can be written as follows:

$$\psi = (A\cos k_x x + B\sin k_x x)e^{-ik_y y - ik_z z} \tag{2.10}$$

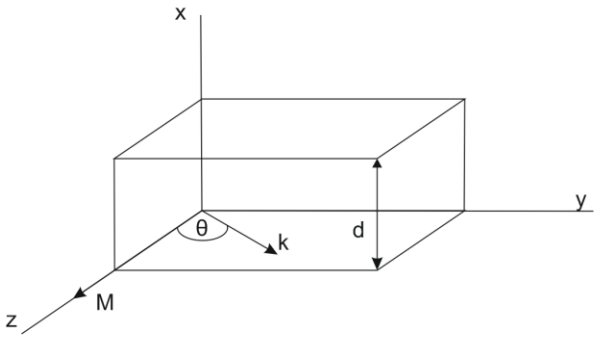

Fig 2.3.2 Geometry of magnetostatic back volume waves. As in previous chapters the coordinate system is taken such that the magnetization vector coincides with the z-axis.

Solving the Walker equation again we get the following dispersion relation

$$\omega^2 = \omega_H \left(\omega_H + \frac{\gamma M_0}{1 + (\cos\theta)^2 \left((\sin\theta)^2 + \frac{(n\pi)^2}{(kd)^2} \right)^{-1}} \right) \tag{2.11}$$

When the angle $\theta = \frac{\pi}{2}$ the spin wave frequency is independent of the wave vector. In the other limiting case when $\theta = 0$ (spin waves propagate in the direction of the magnetization), the frequency of the waves reduces with increasing wave vector. So the vector of the group velocity is antiparallel to the vector $\vec{k}$ and to the vector of the phase velocity $\vec{v}_{ph} = \frac{\omega}{k^2}\vec{k}$. Such waves are called backward waves. We described dispersion relations for the volume waves, where the magnetic potential dependence on the coordinate in the direction perpendicular to the sample surface is described with trigonometric functions. However, the solutions of eq. (2.7) could also be hyperbolic function, and corresponding k-vectors are complex numbers $k^2 < 0$. Such waves do not propagate in the magnetic volume, but can travel along the sample boundary. Let us regard the case when magnetization lies in the sample plane and the wave vector is perpendicular to it. The sample is a thin film with thickness d. The dispersion relation for surface waves in this case was found by Damon and Eshbach[26]

$$\omega^2 = \left(\omega_H + \frac{\gamma M_0}{2} \right)^2 - \frac{(\gamma M_0)^2}{4} e^{-2kd} \tag{2.12}$$

These surface waves are called Damon- Eshbach spin waves.

The relation for the group velocity can be found as $v_{gr} \equiv \frac{\partial \omega}{\partial k}$ and its value is

$$v_{gr} = \frac{d\gamma^2 {M_0}^2 e^{-2kd}}{4\omega} \tag{2.13}$$

In figure 2.3.3 the dispersion relations for all three spin wave types are plotted.

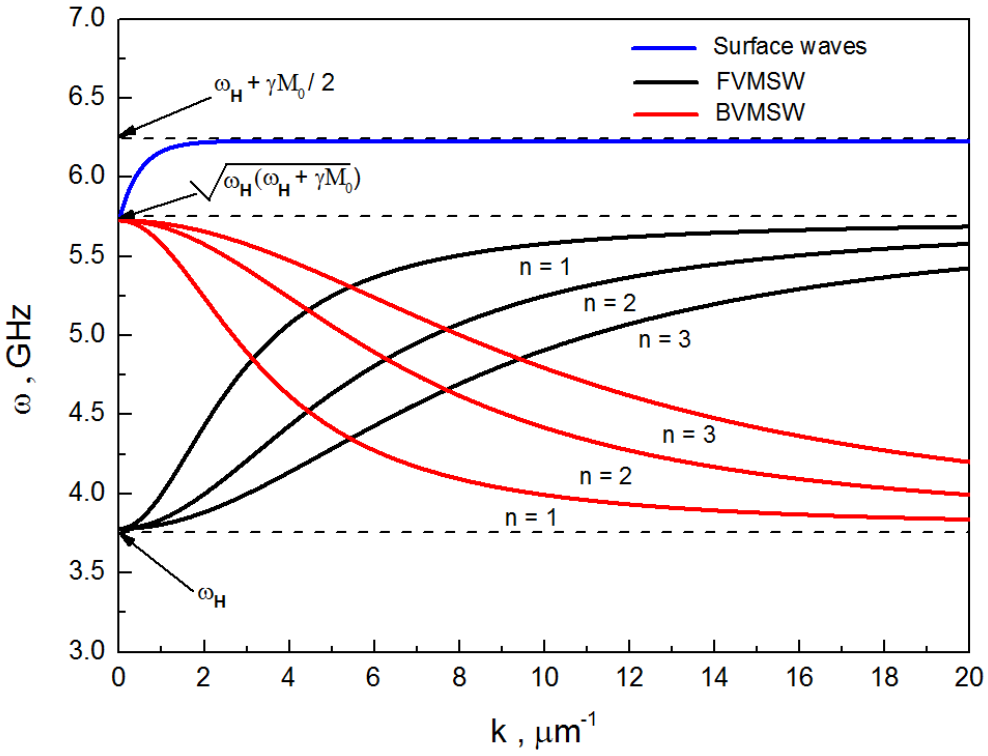

Fig 2.3.3 Dispersion relations for different magnetostatic wave types. The magnetic field is H = 135 mT, the saturation magnetization M_0 = 175 mT (YIG), the film thickness d = 1 μm , n is the mode number for volume waves. The dashed lines show the frequency range for different waves.

Thus, different types of magnetostatic waves can be excited depending on the directions of the vectors $\vec{M}$ and $\vec{k}$ with respect to the sample plane. The range of any dispersion curve can be adjusted by increasing or decreasing of the magnetic field H since $\omega_H = \gamma H$. In this thesis we study the Damon- Eshbach spin wave modes.

3. Spin pumping and spin Hall effect

3.1 Phenomenological explanation of spin pumping

Spin pumping is a very interesting effect that occurs at the interface of a ferromagnet (FM) and a non-magnetic metal (NM). The physical principle of the effect is the following: when the magnetization vector starts the precessional motion a spin current is emitted from the FM to NM through the interface. Experimentally this phenomena was first observed by Mizukami[27 28] and Urban[29]. In their measurements they observed an increased Gilbert damping at FMR due to the flow of spin angular momentum from FM to NM (see fig 3.1.1). The spin polarization of the electrons is parallel to the vector of the magnetization.

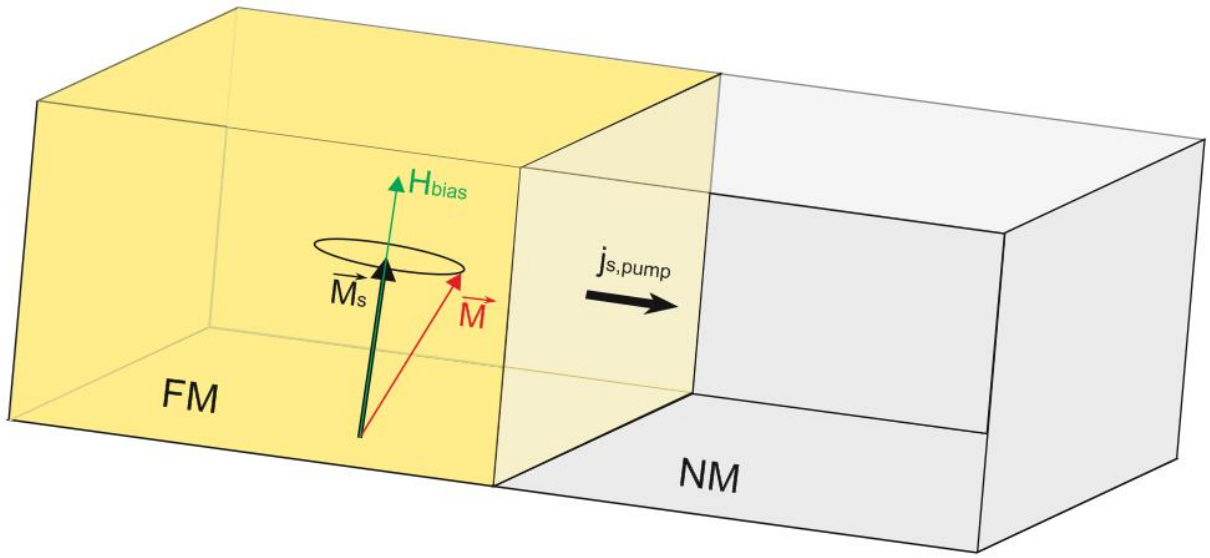

Fig 3.1.1 Spin pumping gives rise to a spin current through the interface which results in an increase of the Gilbert damping.

3.2 Theory of the spin pumping

A theoretical model of spin pumping was developed by Tserkovnyak et al[30 31 32] by modifying the theory of the adiabatic pumping[33 34] with consideration of the spin degree of freedom. In this subchapter we describe quantitatively the spin current flowing through the interface and its influence on the magnetic damping in a material. The FM and NM are regarded as two electron reservoirs connected with a channel able to conduct a spin current dependent chemical potentials $\mu_\uparrow$ and $\mu_\downarrow$. (see fig 3.2.1).

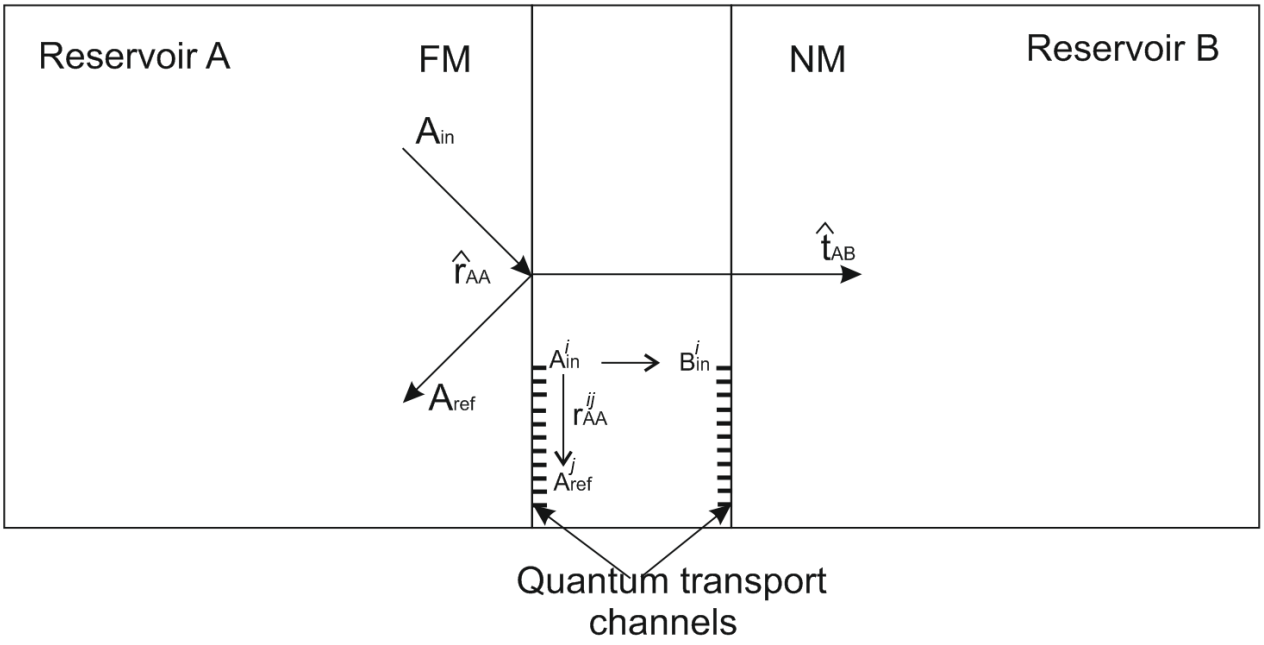

Fig 3.2.1 The interface between the reservoirs is presented as a sum of a large number of the small quantum transport channels. A_{in} and A_{ref} are the overall amplitudes of the incident and reflected electron waves. r^{ij}_{AA} is a probability that an electron that entered channel i with amplitude A^i_{in} will be reflected to the same reservoir through the channel j with amplitude A^j_{ref} . Assuming that the interface has N transport channels, $\hat{r}_{AA}$, $\hat{t}_{AB}$, $\hat{t}_{BA}$, $\hat{r}_{BB}$ will be NxN transmission and reflection matrices.

The transport properties of the channel are described by the spin scattering matrix $\hat{S}$

$$\hat{S} = \begin{pmatrix} \hat{r}_{AA} & \hat{t}_{AB} \\ \hat{t}_{BA} & \hat{r}_{BB} \end{pmatrix} \tag{3.1}$$

where $\hat{r}_{AA}$, $\hat{t}_{AB}$, $\hat{t}_{BA}$, $\hat{r}_{BB}$ are NxN transmission and reflection matrices. Here we consider the NM as a perfect spin sink which means that there is no spin accumulation building up. Such approximation is valid when the transmitted spin current either decays or leaves the interface area very fast. In equilibrium the chemical potentials of both reservoirs are equal $\mu_A = \mu_B$. No electrical current flows through the interface. If a voltage V is applied to the interface, it shifts the chemical potentials with respect to each other $\mu_A - \mu_B = \delta\mu \neq 0$. It also leads to a current flowing through the interface:

$$\delta I = \frac{2e}{h}\delta\mu \sum_i \sum_j \left|t_{ij}\right|^2 \tag{3.2}$$

where t_{ij} is a transmission probability from channel i to channel j. Now let us assume the same interface at FMR and without a voltage application. The magnetization precession periodically changes the spin

This assumption is justified when the precession period is much smaller than the spin flip relaxation times. The adiabatic change of potentials $\mu_\uparrow$ and $\mu_\downarrow$ occurs in the direction parallel to the momentary spin quantization axis. Applying the scattering matrix theory to the adiabatic magnetization precession, one can get the expression for the spin current pumped from FM to NM[30].

$$I_s^{pump} = \frac{h}{4\pi}\left(A_r \vec{n} \times \frac{d\vec{n}}{dt} - A_i \frac{d\vec{n}}{dt}\right) \tag{3.3}$$

Here $\vec{n} = \frac{\vec{M}}{M_s}$ is the unit vector of the magnetization and $A \equiv A_r + iA_i = g^{\uparrow\downarrow}$ is the interface spin mixing conductance, which is a dimensionless parameter. Real and imaginary parts of $g^{\uparrow\downarrow}$ depend on the scattering matrix (3.1). In comparison with the Landau-Lifshitz equation (1.19) the term proportional to the real part of the spin mixing conductance A_r changes the effective damping α, and the imaginary part A_i changes the torque term and gyromagnetic ratio γ. Experimentally A_r can be obtained by comparing the Gilbert damping parameter measured in the ferromagnet and in a FM/NM bilayer. The imaginary part A_i affects the shift of the resonance field. Thus, the modified Landau-Lifshitz equation with consideration of the spin pumping term can be written as follows:

$$\frac{\partial \vec{M}}{\partial t} = -\gamma \vec{H}_{eff} \times \vec{M} + \frac{\alpha \vec{M}}{M_0} \times \frac{\partial \vec{M}}{\partial t} + \frac{\gamma}{V_{FM}} I_s^{pump} \hat{\vec{\sigma}} \tag{3.4}$$

where $\hat{\vec{\sigma}}$ is the spin current polarization and V_{FM} is the volume of a ferromagnet.

The conductance for differently polarized spin currents can be defined as follows:[35]

$$G^{\uparrow} = \frac{e^2}{h}\left[M - \sum_{nm}\left|r_{nm}^{\uparrow}\right|^2\right] = \frac{e^2}{h}\sum_{nm}\left|t_{nm}^{\downarrow}\right|^2 \tag{3.5}$$

$$G^{\downarrow} = \frac{e^2}{h}\left[M - \sum_{nm}\left|r_{nm}^{\downarrow}\right|^2\right] = \frac{e^2}{h}\sum_{nm}\left|t_{nm}^{\downarrow}\right|^2 \tag{3.6}$$

$$G^{\uparrow\downarrow} = \frac{e^2}{h}\left[M - \sum_{nm}(r_{nm}^{\uparrow})(r_{nm}^{\downarrow})^*\right] \tag{3.7}$$

where $G^{\uparrow}$ and $G^{\downarrow}$ describe spin conserving transfer through the interface. The parameter $G^{\uparrow\downarrow}$ provides information about the transfer of spin through the interface and is bounded with dimensionless spin mixing conductance with following relation: $G^{\uparrow\downarrow} = \frac{e^2}{h}\, g^{\uparrow\downarrow}$. Previously, we considered a NM as a perfect sink i.e. no spin accumulation was built in NM in the interface area. However, in real systems there is always some spin accumulation which results in a backflow current I_s^{back} in the direction of the FM. The total spin current flow is defined as follows:

$$I_s^{total} = I_s^{pump} - I_s^{back} \tag{3.7}$$

To define the strength of the backflow current, the parameter $\epsilon = \frac{\tau_{el}}{\tau_{sf}}$, which is the ratio of elastic spin scattering rate τ_{el} and the spin-flip scattering rate τ_{sf}, should be considered[30]. This parameter increases as a function of spin orbit coupling, which is proportional to the atomic number. A material can be considered as a good "spin-sink" if $\epsilon \geq 10^{-2}$. With increase of the parameter ϵ, the efficiency of the spin current relaxations in the NM layer also increases. Correspondingly, the backflow current to FM decreases. Reduction of the spin accumulation can be described by the spin diffusion length[30] as following[34]:

$$\lambda_{sd} = v_F \sqrt{\frac{\tau_{el}\tau_{sf}}{3}} \tag{3.8}$$

where v_F is the electron velocity at the Fermi level.

To take the backflow current and spin accumulation into consideration the effective spin mixing conductance $g_{eff}^{\uparrow\downarrow}$ is introduced instead of $g^{\uparrow\downarrow}$.[29]

$$g_{eff}^{\uparrow\downarrow} = g^{\uparrow\downarrow} \frac{1}{1 + \frac{1}{4\sqrt{\frac{\epsilon}{3}} \tanh \frac{d_{NM}}{\lambda_{sd}}}} \tag{3.9}$$

where d_{NM} is the thickness of the normal metal and λ_{sd} is the spin diffusion length.

For Pt the parameter $\epsilon > 10^{-1}$ which results in relatively small difference between $g^{\uparrow\downarrow}$ and $g_{eff}^{\uparrow\downarrow}$. Additional damping caused by spin pumping[17] can be expressed as follows:

$$\alpha = \alpha_0 + \alpha_{sp} = \alpha_0 + \frac{g\mu_B}{4\pi M_s d_{FM}}\, g_{eff}^{\uparrow\downarrow} \tag{3.10}$$

where g is the Lande factor in FM, μ_B is the Bohr magneton, d_{FM} is the thickness of the FM film. The additional term caused by spin pumping can be easily measured by comparing the FMR linewidth of FM and NM/FM samples.

3.3 Spin Hall effect phenomena

The Spin Hall effect is a complicated quantum-mechanical phenomena. When an electrical current flows through a metal with large spin-orbit coupling, electrons with opposite spins are deflected in opposite directions. This results in a spin current flowing in the direction transverse to the initial electrical current. If the sample has a finite size, the spins with opposite polarizations are accumulated on the opposite sides of the slab (see fig 3.3.1). If a ferromagnetic material is brought into contact with the spin accumulation region, a torque acts on the magnetic moments of this material. This torque transfer occurs either with- or without transfer of electrons through the interface depending on the conductivity of the ferromagnetic.

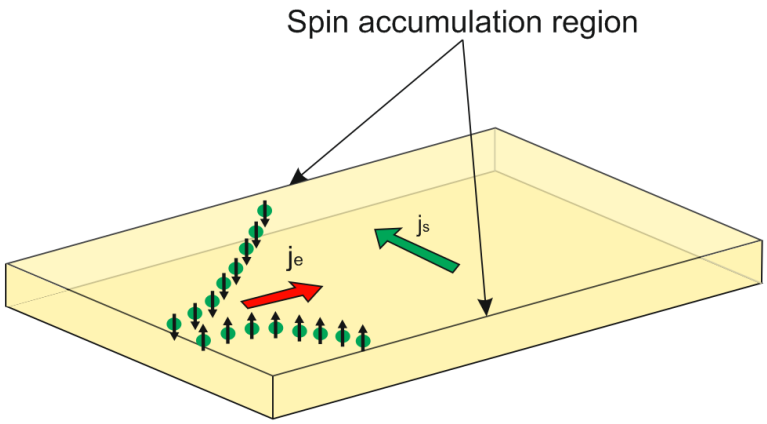

Fig.3.3.1 Phenomenology of the SHE. A charge current I_e is transformed into a pure spin current I_s in the transverse direction.

According to Onsager´s relations there should be an effect reciprocal to SHE, the inverse Spin Hall effect. Indeed if spin current flows in some direction, it is transformed into a charge current in the transverse direction. The SHE and ISHE are characterized by the Spin Hall angle θ_{SH}. This dimensionless parameter shows the efficiency of the transformation of a charge current into a transverse spin current.

A spin current is connected to a charge current with the following relation[36 37]

$$\vec{j}_s = \frac{h}{2e}\theta_{SH}\,\vec{j}_e \times \vec{s}$$

where $\vec{s}$ is a unit vector of the spin polarization, $\vec{j}_s$ and $\vec{j}_e$ are the densities of the spin and charge currents.

The nature of the SHE, ISHE and anomalous Hall effect (AHE) lies in three common mechanisms which were first discussed for the AHE[38]. These mechanisms are separated according to their dependence on the Bloch state transport lifetime τ. The quasi particle scattering range is defined as the inverse value τ^{-1}. The contributions of different mechanisms on the spin Hall conductivity σ_{xy}^{H} vary as τ^1 and τ^0 (which means it is independent from the longitudinal conductivityσ_{xx}). The contribution proportional to τ^1 is usually called the skew scattering contribution σ_{xy}^{H-skew}. The other two contributions proportional to τ^0 are called intrinsic σ_{xy}^{H-intr} and side-jump $\sigma_{xy}^{H-side-jump}$. Thus, the total spin Hall conductivity is derived as follows:

$$\sigma_{xy}^{H} = \sigma_{xy}^{H-skew} + \sigma_{xy}^{H-intr} + \sigma_{xy}^{H-side-jump} \tag{3.12}$$

Further more detailed description of each contribution is given.

3.4 Skew scattering contribution

Skew scattering is an asymmetric feature that occurs in chaotic scattering events in the presence of strong spin-orbit coupling. It has its origin in Mott scattering[39 40]. If an electron with a random spin polarization scatters from an atom, the electron spin is polarized depending on the scattering direction (see fig 3.4.1)

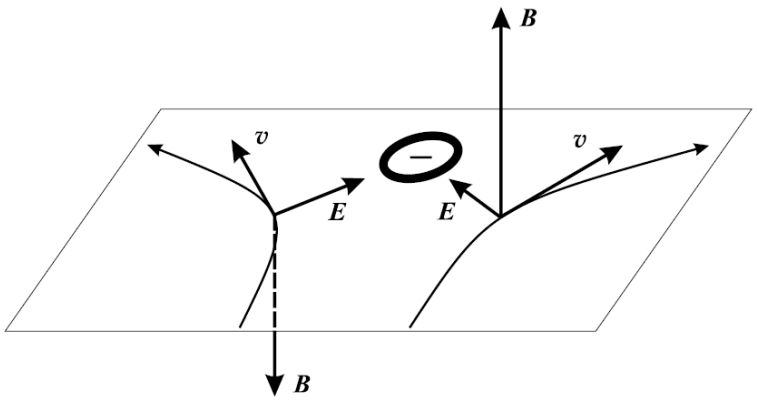

Fig.3.4.1 Scattering of an electron by a negative charge. The electron spin "sees" a magnetic field ($B \sim E \times v$) normal to the plane of the electron trajectory. The field polarizes the electron spin "up" when the electron is deflected to the right. For the electrons deflected to the left the spin polarization is "down".

When an electron is scattered by a negative charge, the spin "sees" a magnetic field (B~ E × v) normal to the plane of the electron trajectory[41] (see fig 3.4.1).The strength of this "spin-orbit" magnetic field depends on the vector *E*, which is obviously larger for atoms with higher atom number Z (heavy atoms). That is why heavy materials such as Pt are the best candidates for studying the SHE. This explanation is purely qualitative and also rather simplified. A more detailed study of this aspect was done by Smit[42 43] . The transition probability from state *n* to state *m* ($W_{n\to m}$) should be equal to the transition probability ($W_{m\to n}$). Here each state of the particle is defined by two parameters: spin (s) and the wave vector (k). The transition probability is given as follows:

$$W_{n\to m} = \frac{2\pi}{h} |\langle n|V|m\rangle|^2 \delta(E_n - E_m) \tag{3.13}$$

where *V* is a perturbation inducing the transition. However, in calculations of the Hall conductivity the microscopic balance fails due to the presence of the asymmetric part of the transition probability

$$W^A_{kk'} = -\tau_A^{-1} k \times k' M_s \tag{3.14}$$

where τ_A^{-1} is Equation (3.14) shows that the scattering probabilities from state k to k' are not equal ($W_{k\to k'} \neq W_{k'\to k}$). This leads to a current proportional to the longitudinal current driven by electric field. A spin Hall resistivity occurs to be proportional to the longitudinal resistivity ρ ($\rho_H^{skew} = \sigma_H^{skew}\rho^2$).

3.5 Side-jump contribution

In the presence of spin orbit coupling the electron Hamiltonian, which consists of potential and kinetic energy gets an extra term H_{SO} defined as follows:

$$H = H_0 + H_{SO} = \frac{h}{2m}\nabla^2 + V(r) + \frac{1}{2m^2c^2}\frac{1}{r}\frac{\partial V}{\partial r}S_Z L_Z \tag{3.15}$$

where S_Z and L_Z are the z-components of the spin and orbital angular momentum, correspondingly. The side-jump contribution is defined[44] as scattering of a Gaussian wave packet from a spherical potential well of radius R given as follows:

$$V(r) = \begin{cases} \frac{h^2}{2m}(k^2 - k_1^2) & (r < R) \\ 0 & (r > R) \end{cases} \tag{3.16}$$

A wave packet with wave vector k suffers a displacement Δy transverse to k (see Fig 3.5.1)

$$\Delta y = \frac{1}{6}k\lambda_c^2 \tag{3.17}$$

where $\lambda_c = \frac{h}{mc}$ is the Compton wavelength.

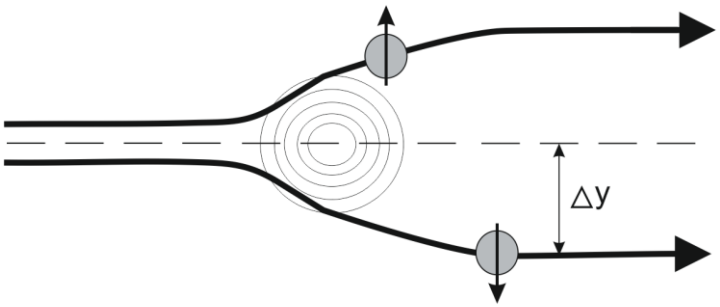

Fig.3.5.1 The electron is deflected by electric fields in the vicinity of the impurity. The time integrated velocity deflection is a side-jump. As in the previous case spin orbit coupling polarizes the spins in the opposite directions.

As noticed in subchapter 3.3 the side jump contribution is independent of the longitudinal conductivity σ_{xx}.

3.6 Intrinsic contribution

This contribution is the easiest to evaluate accurately. The non-equilibrium electron dynamics of the Bloch electrons, accelerated by the electric field, creates an anomalous velocity in the direction transverse to this field (see fig 3.6.1). The intrinsic contribution to the spin Hall conductivity (SHC) depends on the electron band structure of the crystal lattice. The Kubo formula[45] that describes (SHC) has a term proportional to the derivative of effective electron band Hamiltonian with respect to the electron wave vector $\vec{k}$. This term is called a Berry curvature $\vec{b}_n$ [46] [47] [48] and it is responsible for the anomalous electron velocity. For Pt , $\vec{b}_n$ at low temperatures has large peaks for electrons that lie in X and L critical points of the first Brillouin zone (X- center of a square face, L-center of a hexagonal face). With the increase of the temperature the SHC decreases monotonically.

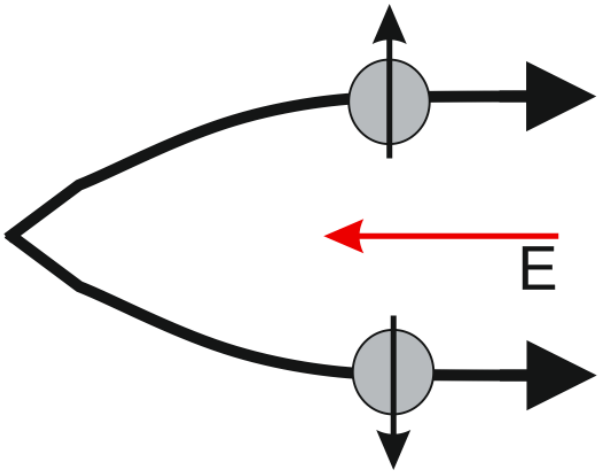

Fig.3.6.1 The non-equilibrium electron dynamics induced by an external electric field gives a rise to a velocity contribution perpendicular to the field direction $\frac{d\langle\vec{r}\rangle}{dt} = \frac{\partial\vec{E}}{h\partial\vec{k}} + \frac{e}{h}\vec{E}\times\vec{b}_n$. *Electrons have an anomalous velocity perpendicular to the electric field related to their Berry phase curvature.*

A detailed mechanism of intrinsic contribution is not discussed within this thesis, due to its complexity and also due to the fact that for the room temperature Pt, the intrinsic contribution to the conductivity is dominated by the skew scattering. In Fig 3.6.2 we just show the calculations of the spin Hall conductivity done by Guo et all[49]

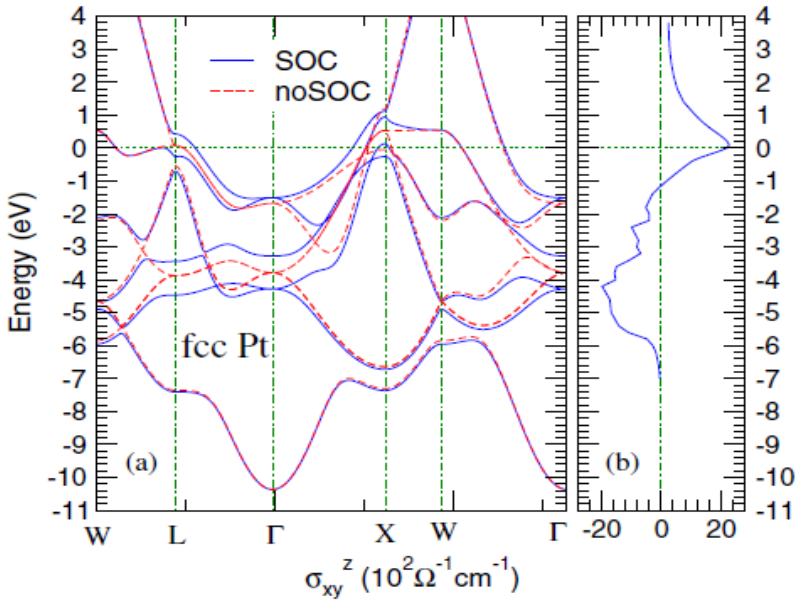

Fig 3.6.2 (a) Relativistic band structure and (b) spin Hall conductivity of face-centered cubic Pt lattice. The zero energy and the dotted line is the Fermi level. The dashed curves in (a) are the scalar-relativistic band structure. From ref Guo et all[49]

As can be seen from Fig 3.6.2(b) the spin Hall conductivity becomes rather small at the Fermi energies higher than 3 eV. It has a peak at the Fermi level of 0 eV and then decreases changing a sign at – 1.1 eV. As the Fermi energy is further lowered the conductivity has another peak at -4.2 eV and then drops to the zero value at -7 eV.

3.7 Experimental approach to SHE measurements

There are several ways to measure the SHE in a ferromagnetic film. For example it can be detected electrically via the ISHE[50]. In our thesis we used the method of modulation of damping (MOD) and we briefly describe it here. Experimental geometry is shown in Fig 3.7.1.

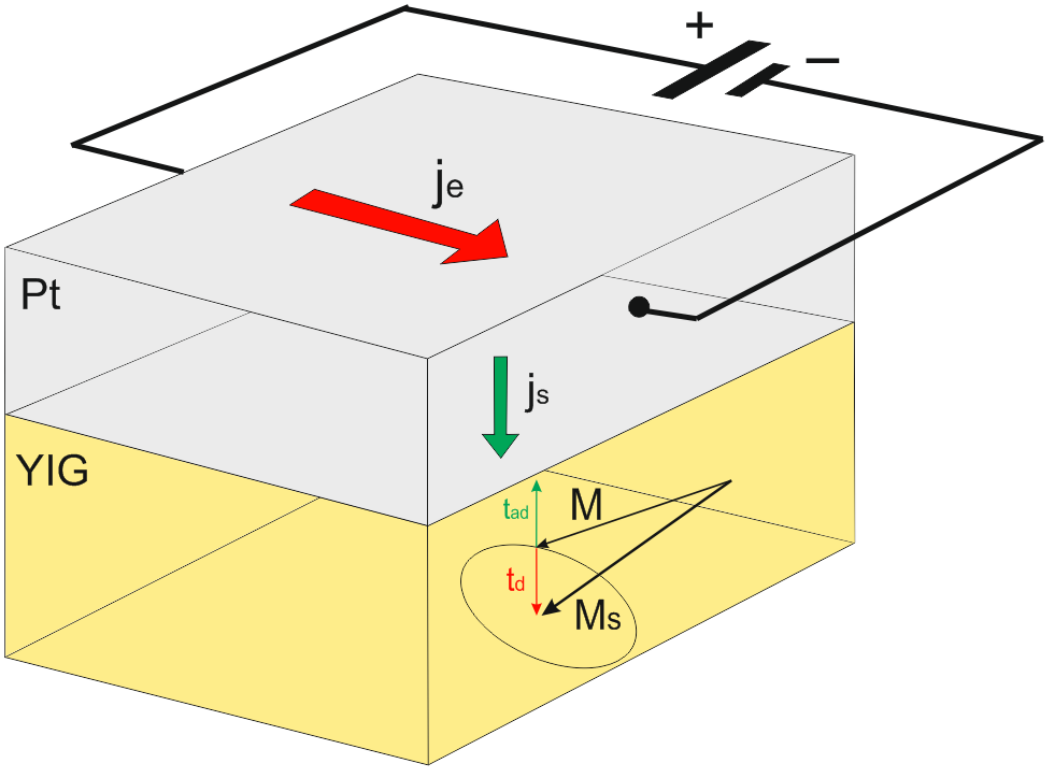

Fig.3.7.1 The MOD experiment for YIG/Pt bilayer. Electrical current j_e flowing through the Pt layer creates a transverse spin current j_s towards the interface via the SHE. A spin accumulation at the interface creates an extra torque that acts on the magnetic moments inside the YIG film. Depending on the polarity of the electrical current in Pt, this torque can either increase the Gilbet damping (damping torque t_d) or decrease it(anti-damping torque t_{ad}).Damping and anti-damping torques are marked red and green correspondingly.

As can be seen the change in the damping is proportional to the spin current flowing towards the interface. The spin current is proportional to the electrical current and the SH angle. Thus the SH-angle can be calculated from measurements of the Gilbert damping change. In our case, the FMR linewidth which is proportional to the Gilbert damping parameter is measured optically.

Magnetization dynamics is assumed to follow the Landau-Lifshitz equation modified with the spin transfer term[51]

$$\frac{\partial \vec{m}}{\partial t} = -\gamma \vec{H} \times \vec{m} + \alpha \frac{\vec{m}}{M_s} \times \frac{\partial \vec{m}}{\partial t} + \gamma \frac{\hbar j_s}{2e\mu_0 M_s d} \times \vec{m} \times \vec{\sigma} \times \vec{m} \tag{3.18}$$

where d is the thickness of the ferromagnet layer , μ_0 is the vacuum permeability, $\vec{\sigma}$ is the direction of the injected spin moment, j_s is the spin current density, e is the electron charge.

If we linearize and solve the equation as it is described in sub chapter 1.2 we can get the following relation for the magnetic susceptibility:

$$\chi' = \gamma M_s \frac{\gamma(H + M_s)(\omega_0^2 - (1-\alpha^2)\omega^2) + \alpha\Delta\,\omega^2}{(\omega_0^2 - (1+\alpha^2)\omega^2)^2 + \Delta^2\omega^2}$$

$$\chi'' = \gamma M_s \omega \frac{\gamma\Delta(H + M_s) - \alpha(\omega_0^2 - (1-\alpha^2)\omega^2)}{(\omega_0^2 - (1+\alpha^2)\omega^2)^2 + \Delta^2\omega^2} \tag{3.19}$$

where $\omega_0^2 = \gamma^2 H(H + M_s)$ is the FMR frequency of the in-plane magnetized film, H is the external magnetic field and Δ is resonance peak linewidth defined as follows[52]:

$$\Delta = \gamma\alpha(M_s + 2H) + \frac{\hbar j_s}{e\mu_0 M_s d} \tag{3.20}$$

The resonance peak linewidth in frequency units Δ can be recalculated in the resonance linewidth in field units dH with the help of the following relation:[12]

$$\Delta = \frac{\gamma^2}{\omega_0}\, dH\, (2H + Ms\,) \tag{3.21}$$

Putting the eq.(3.21) into eq. (3.20) we will get the following relation[53] that connects the FMR-linewidth dH to the density of the spin current flowing towards the interface.

$$dH = \frac{\omega}{\gamma}\left(\alpha + \frac{\hbar j_s}{d\mu_0 M_s e(2H + M_s)}\right) \tag{3.22}$$

Further, this equation is used for calculations of the SH angle.

4. Experimental setups and sample preparation

4.1 FMR setup with coplanar waveguide

The measurement of FMR is one of the most important steps in almost any task related to spin waves, spin pumping and spin Hall effect. These measurements provide information about the Gilbert damping parameter, effective magnetization, sample homogeneity, spin-mixing conductance (for bilayers) and other properties. In fact, FMR characterization defines whether an experimental sample is proper for further more complicated measurements. For example, if the linewidth of the sample is very large, the amplitude of the absorption curve is small or its spectra possesses multiple peaks, it is evidence of poor sample quality i.e. presence of inhomogeneities, etc. The study of more complicated effects on such a sample is either difficult or impossible.

There are several ways to excite ferromagnetic resonance in a magnetic material. The first one is using a coplanar waveguide (CPW) where magnetization precession is excited by a high frequency current flowing in the signal and ground lines of the CPW (see fig 4.1.1). The second way is metal cavity (resonator) measurement. Both methods have their own advantages and both of them are used in this thesis.

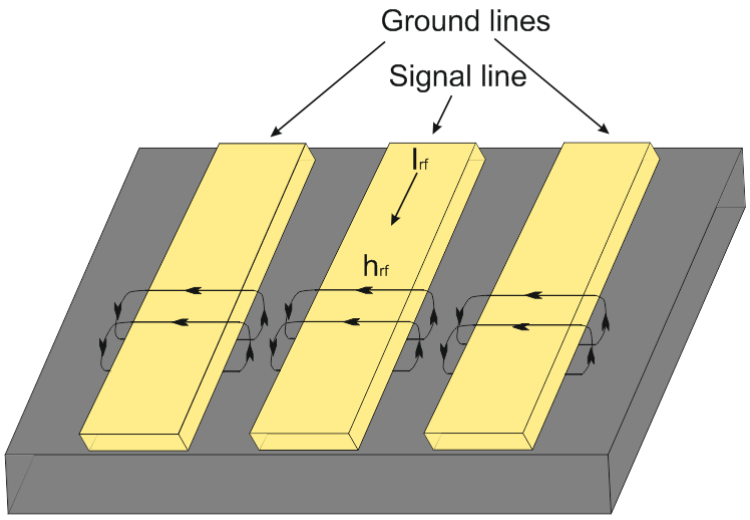

Fig.4.1.1 Geometry of high frequency magnetic fields created by a CPW. Condition for FMR excitation: H_{bias} *perpendicular to* h_{rf} *.*

The CPW method is rather simple in the case of thin full film measurements. The sample is just placed on top of the CPW as shown in fig 4.1.2 (A). The width of the signal line is 1.5 mm and the width of the gap is 0.5 mm for our setup. The impedance is matched to 50 Ohm. The sample is placed in the FMR geometry, the rf-exictation field is perpendicular to the bias field. Microwave currents running in the CPW excite the rf-field which drives the magnetization of the sample out of plane. In ferromagnetic resonance the amplitude of the magnetization oscillation rises and the energy absorbed by the sample increases. This loss of energy can be easily analyzed by measuring the change of the transmitted signal. Such conventional measurements are averaged over large sample surface in the vicinity of the CPW. The absorption curve has a Lorentz shape in the ideal case. Since the Lock-in technique is used, the measured signal is the derivative of the Lorentz curve. A block diagram with the detailed setup description can be found in Appendix. A typical FMR curve for a single frequency is shown in Fig.4.1.2 (B).

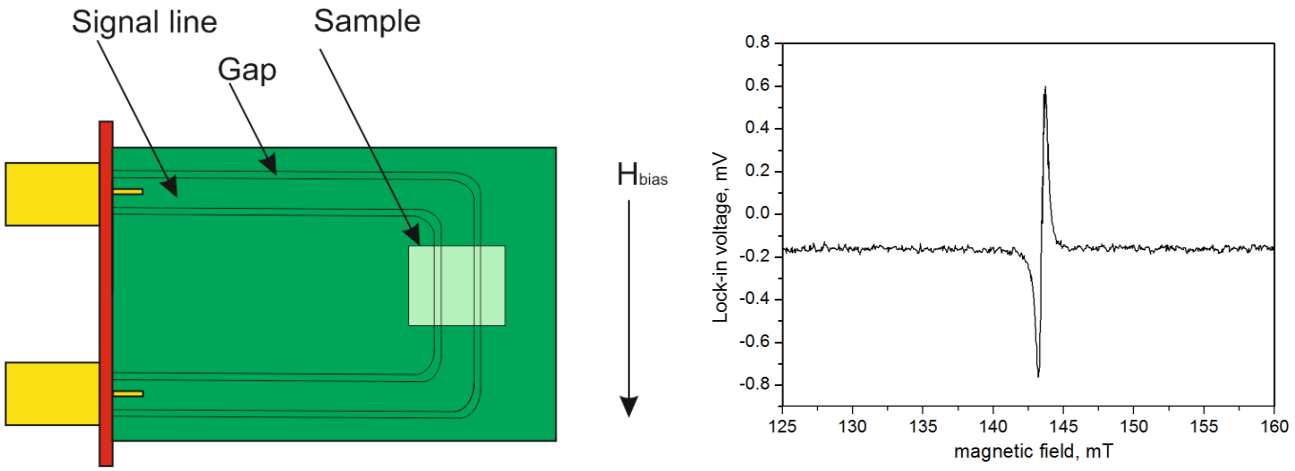

A) B)

Fig.4.1.2 Sample mounted on the CPW in FMR geometry. FMR curve recorded for 6 GHz frequency on a 50 nm thick YIG sample.

Important advantage of this method is that it allows working with very small (less than 1 μm) magnetic objects. In this case the magnetic structure prepared with lithography is placed in the gap between signal and ground lines. The measurement is usually realized with optical methods (Kerr or Faraday effects) since they allow local probing of the sample. The FMR curves are measured for different frequencies and fitted with the Lorentz derivative in order to extract the FMR linewidth. Plotting the dependence of the linewidth on the resonance frequency and performing a linear fit allows to extract the Gilbert damping parameter α. Plotting the dependence of the resonance frequency on the resonance field and

then fitting it with the Kittel formula (1.42) provides information about the effective magnetization and the gyromagnetic ratio.

4.2 FMR setup with cavity

In case of cavity setup the FMR is excited by microwave currents flowing in the walls of the resonator. The physical principle of this method is based on measuring the coupled resonance which allows achieving very high sensitivity, due to the high Q-factor of the metal resonator. This is the most important advantage of cavity measurements. However, these measurements require an accurate adjustment of the coupling and cavity size, which makes them more difficult to perform. This method also does not allow local optical measurements since it is impossible to insert a laser beam into the waveguide system. The physical principle of the setup is rather simple. A high frequency signal of fixed power created by a frequency generator goes into the cavity. The signal is reflected from the rear wall of the cavity and measured afterwards. Since microwave losses in metal waveguides are almost zero, the only source of the losses is the cavity. Measuring the difference between the input power and power reflected from the cavity the dissipation processes inside of the cavity can be characterized. For the Spin Hall effect experiments, we measure the difference between the input and resonator reflected microwave power and its dependence on the magnetic field and the current applied to the YIG/ Pt interface. A more detailed setup description of the setup is given in the Appendix. The most important element is the metal cavity with a ferromagnetic sample inside shown in fig 4.2.1.

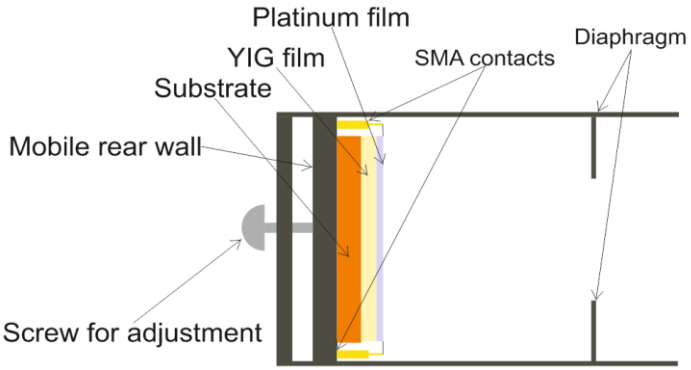

Fig.4.2.1 Schematic picture of the resonator. The sample is glued to the rear wall, so it is permanently positioned in a node of the electric field. For the H_{10} – electromagnetic wave a minimum of the electric field corresponds to a maximum of the magnetic field, so we have conditions for the most effective FMR excitation.

The sample is glued to the rear wall of the resonator which is controlled by an adjustment screw. The resonance frequency of the resonator is adjusted by moving the resonator rear wall. The current for SHE measurements is supplied through two SMA contacts, screwed in small holes in the rear wall. A thin metal wire is soldered to the SMA contact on one side and glued to a Pt film with colloidal silver glue on the other side. Coupling of the resonator to the rest of the microwave tract is realized with the help of a diaphragm. The Q-factor of the resonator is about 300. In this experiment resonance curves of the coupled system (resonator-YIG sample) are measured for different current polarities. The idea of this experiment is described in fig 4.2.2.

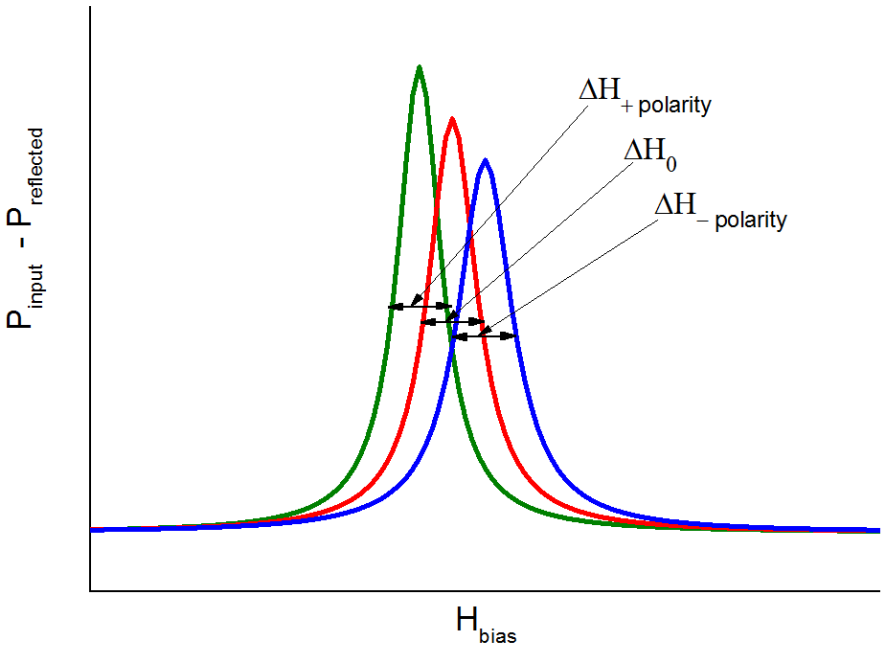

Fig 4.2.2 Basic idea of the cavity-SHE experiment. The dependence of the difference between input and resonator reflected power on the magnetic field for different current polarities. The red line is the absorption curve without current application. Green and blue curves indicate positive and negative current polarities correspondingly. Green and blue curves are shifted with respect to the red curve due to an additional Oersted field arising from the current flow. Extracting the linewidth of the resonance curves allows calculating the change in Gilbert damping due to SHE.

To explain the measurement process the real experimental data obtained in the cavity setup are shown below. The typical data set is presented in fig 4.2.3.

Microwave pulses with pulse width of 160 μs and duty cycle of 0.001 are generated. Such a small duty cycle is needed to reduce heating effects. Figure 4.2.3 shows the signal reflected from the cavity. The figure consists of 6 different insets (A-F) each for the different field. Each inset can be split into three areas marked by the arrows in inset A. For better understanding we describe the signal behavior for each of these areas independently. The first area indicates the absence of microwave pulse. This area is situated within 100 to 170 μs and within 330 to 400 μs on the timescale. The voltage read by oscilloscope is zero since there is no input signal and no reflected signal correspondingly. For any applied magnetic field or applied current this zero level does not change. The second area indicates the microwave pulse. The pulse starts at 170 μs and ends at 330 μs. The resonance of the system is at 2725.3 Oe. At the resonance, the resonator with the sample absorbs maximum energy so the reflected signal decreases. Approaching the resonance by sweeping the field down (insets A and B) reflected power decreases until it reaches its minimum at the resonance field (inset C). The minimum of the reflected signal at -28 mV is marked with the red line in the inset C. Sweeping the field further down, the reflected signal increases again (inset D-F) since the resonator starts to absorb less energy.

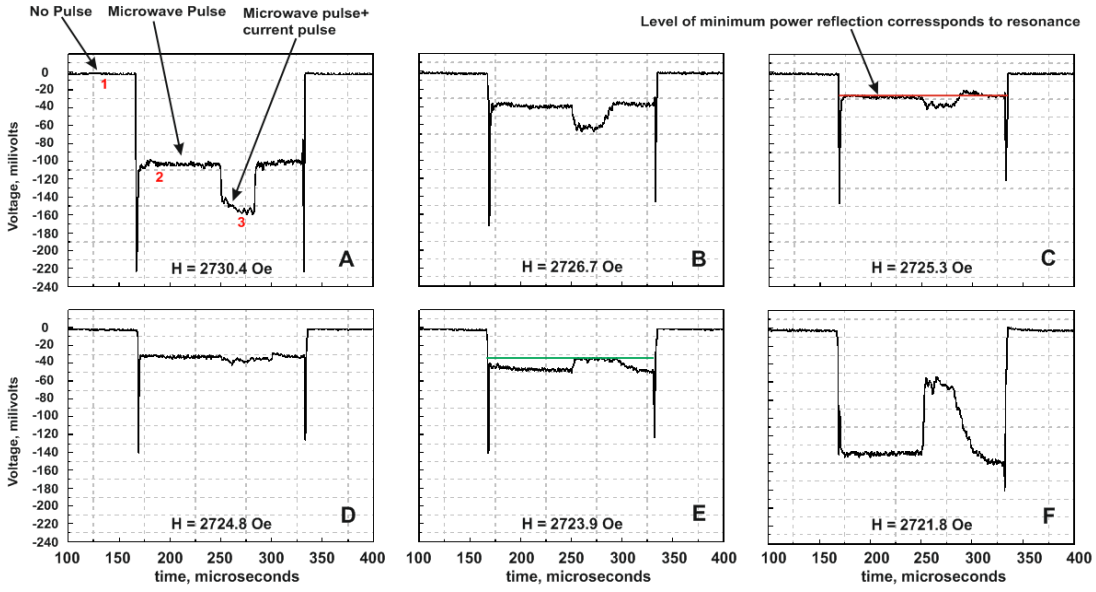

Fig 4.2.3 Typical data set measured in the SHE experiment. The minimum power reflection is smaller in the absence of a current pulse. The current polarity is negative.

The third area indicates the current pulse. The current pulse starts at 250 μs and has a width of 50 μs. Let us assume the current polarity to be negative (we can also assume it positive since it does not play here any role, we just need it to assign the specific current flow direction). As can be seen in inset A the reflection signal is different from the second area. The reason for this is an Oersted field generated by this current. The amplitude of this current pulse for the fixed magnetic field is proportional to the flowing current. In this case the current creates an Oersted field of about 1.5 Oe which points parallel to the bias magnetic field. This means that the actual field during the current pulse (from 250 to 300 μs) is 1.5 Oe larger than the bias field. For inset A, this field value will be 2731.9 Oe which is further from the resonance field of the system, which results in a bigger reflected signal. Sweeping the field further down the third area will repeat the behavior of the second area. After passing the resonance field the signal reflection in area three is smaller than in the second area, since the effective field there is closer to the resonance (insets E, F). The last but the most important detail is the minimum power reflection level in the resonance for the third area. This level is marked by the green line in the inset F and is situated as expected at 2723.9 Oe of the bias field (this corresponds to an effective field of 2725.4 which is the resonance field). The value of the signal is 32.5 mV. The reflected power minimum in presence of the current can not reach the level of the reflected power without a current pulse. That means that the Q-factor of the resonance in the third area is worse than in the second area. This difference can be due to heating of the YIG sample or due to the SHE. This can be easily checked by applying a current of the opposite polarity (now it is positive). Figure 4.2.4 shows the measurements for the positive current polarity. For the second area nothing changed compared to previous case. However, for the third area, the signal has now has the minimum reflection at -13 mV (inset B). Since the Oersted field is now antiparallel to the bias field the ferromagnetic resonance is at 2727.2 Oe (as expected). So, for the positive current polarity we obtain an increase of the Q-factor which proves the presence of the SHE effect in the system.

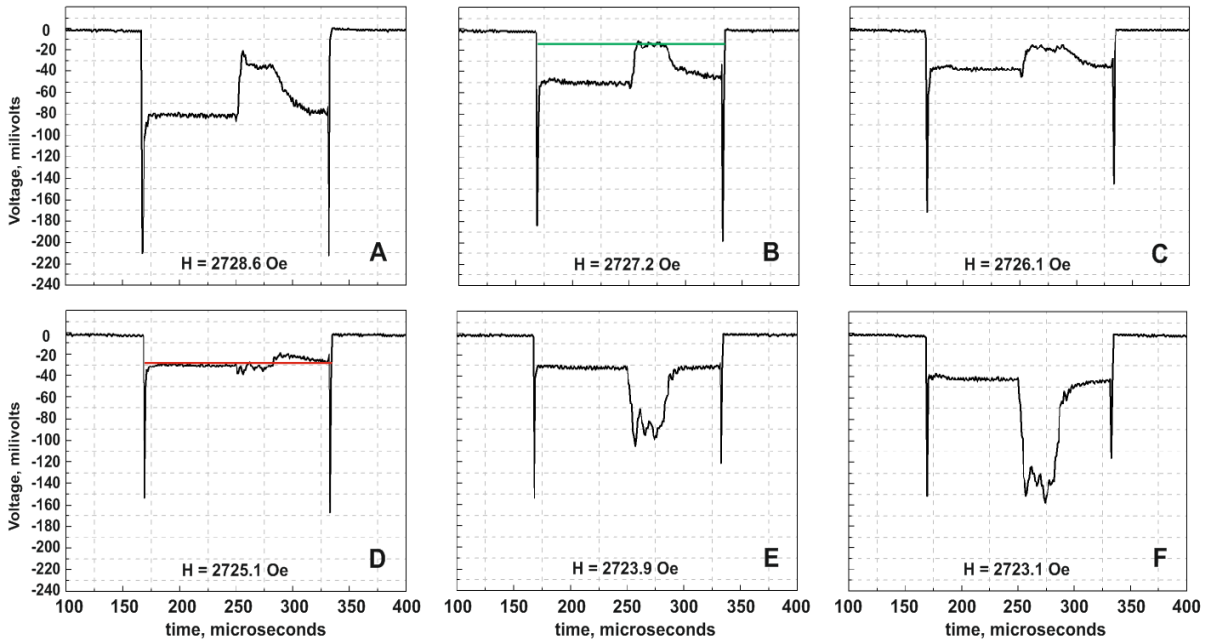

Fig 4.2.4 Typical data set measured in the SHE experiment. The minimum power reflection is smaller in the presence of a current pulse. The current polarity is positive.

4.3 Magneto optical Kerr effect (MOKE)

This method allows to measure magnetization of thin films. The physics of the effect is the following: if light is reflected from a magnetized medium, its polarization changes proportionally to the magnetization of the medium. For example, if the incident beam with linear polarization is reflected from the magnetic medium (for example a ferromagnetic film) light becomes elliptically polarized, and has a principal axis of the ellipse slightly rotated with respect to initial polarization (see Fig 4.3.1). The rotation angle (Kerr angle) is a complex quantity and can be measured with standard optical methods. The physical reason for the Kerr rotation is the difference in the refractive indices for the left and right circular polarized light. Any linearly polarized wave can be presented as a superposition of two waves with right and left circular polarization. If the refractive indices for these waves are different the propagation speed differs correspondingly. It results in elliptical polarization of the initial wave. The refractive indices of the wave polarization are defined as:

$$n = n_0(1 \pm \alpha_k Q) \qquad 4.1$$

Here n_0 is the normal refractive index, α_{k} – is a cosine between the wave vector $\vec{k}$ and magnetization

vector $\vec{M}$, Q is the Voigt constant. In general the Kerr angle can be written as : $\theta_k = \theta_k + i\varepsilon$ where θ_k is the Kerr rotation of the polarization and ε is the elipticity. Further only the Kerr rotation is measured. Our setup is a polar MOKE, which means that Kerr rotation is proportional to out of plane component of the magnetization. All possible MOKE geometries are illustrated in figure below.

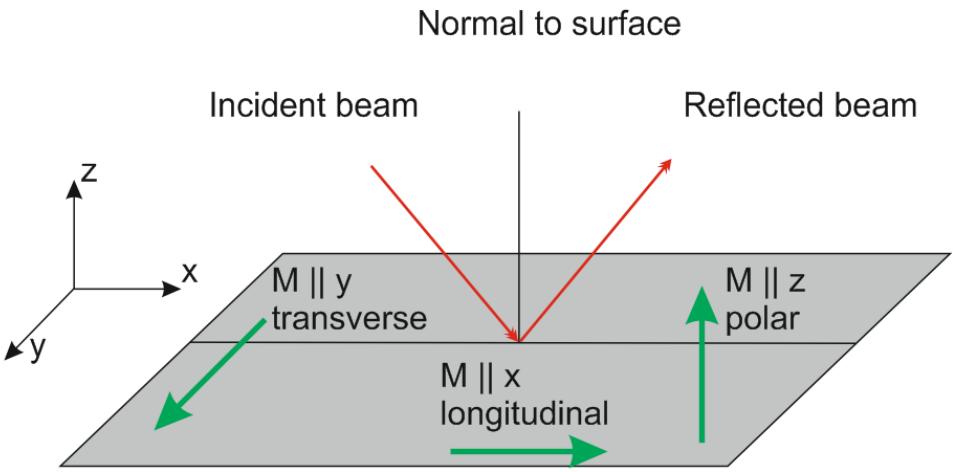

.

Fig 4.3.1 The incident beam polarized in the xz-plane reflects from the ferromagnetic film surface at the same angle. If the film magnetization is perpendicular to the plane it corresponds to polar MOKE geometry (our setup). If it lies parallel to x-axis, it is called longitudinal MOKE. When it is parallel to y-axis it is called transverse MOKE.

Generally, magnetization is not parallel to any of the axis shown in the figure. In this case the impact from all the MOKE components on the polarization rotation angle is measured. However, the longitudinal and transverse components are proportional to the sinus of the angle between the incident beam and the surface normal. If the beam is almost perpendicular to the sample surface (this is fulfilled for our setup) the polar MOKE contribution is measured exclusively.

4.4 Experimental setup for MOKE measurements

Generally, any MOKE setup consists of a light source, polarizer, analyzer and detector. Having passed the polarizer the laser beam gets a determined polarization.

When reflected from the magnetic sample the polarization is rotated by some angle due to the Kerr effect. The analyzer is adjusted so, that without the Kerr rotation the measured signal is zero. When the polarization is rotated by a small angle, the detector measures the signal proportional to that angle. In our setup a Wollaston prism is used as analyzer. A detailed block-diagram of the optical part of the experimental setup with description can be found in the Appendix. For the polar MOKE, in order to measure a Kerr signal, the out of plane component of the magnetization must be created. This is done by running a microwave current through a CPW prepared on the surface of the magnetic film (see Fig. 4.4.1). The coplanar waveguide can excite the uniform magnetic precession (FMR) or spin waves. The microwave signal is created by a frequency generator and measured with a diode-detector. The magnetic field is supplied by an electromagnet with maximum field of about 3000 Oe. The experimental sample is mounted on a stage between the poles of the magnet. In order to use the Lock-in technique we have to modulate some of the experimental parameters. In our case the rf-field is modulated. From the frequency generator the signal goes to the modulator that turns the signal on and off with kHz frequency. From the modulator the signal goes to a attenuator and then to the CPW.

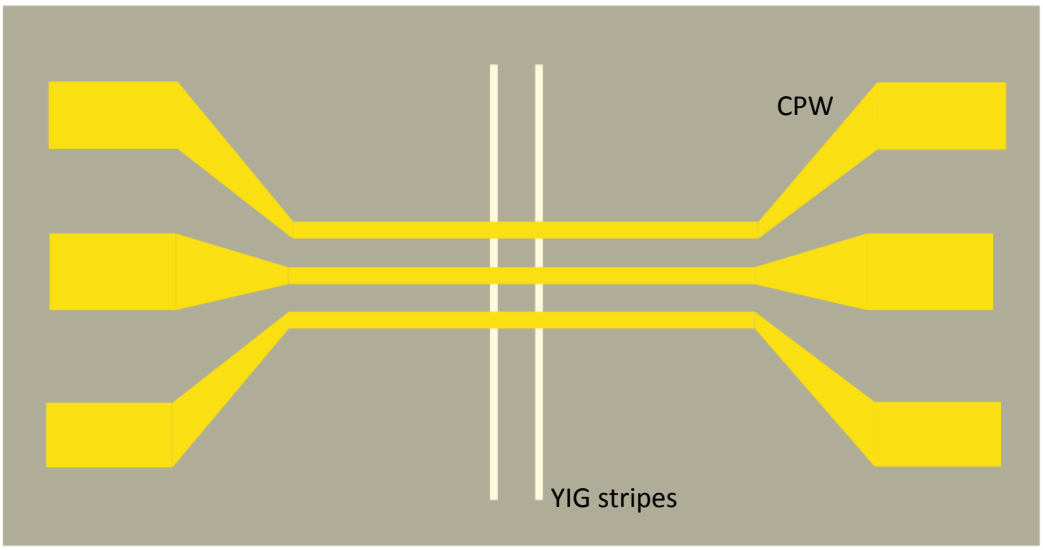

Fig 4.4.1. Schematic top view of the sample for the spin wave measurements. The golden CPW lies on top of the YIG stripes.

Having passed the CPW the signal goes to the detector and then to the PC controlled oscilloscope. Thus the transmitted signal is observed in course of all measurements.

4.5 Time resolved measurements

The microwave signal created by the frequency generator has a cosine-like time dependence. The vector of the out of plane component m_Z has a cosine time dependence $m_Z = m_{Z0} \cos \omega t$ as well. This means that the average value of m_Z over the period is zero.

$$\overline{m_Z} = \frac{\int_0^T m_{Z0} \cos \omega t \, dt}{T}$$

Thus, MOKE measurements in the static mode are not possible since the signal will be also averaged over the large time scale. This problem can be solved by so called time-resolved MOKE experiment, in which the probing laser beam always arrives with a fixed phase shift with respect to the magnetization precession phase.

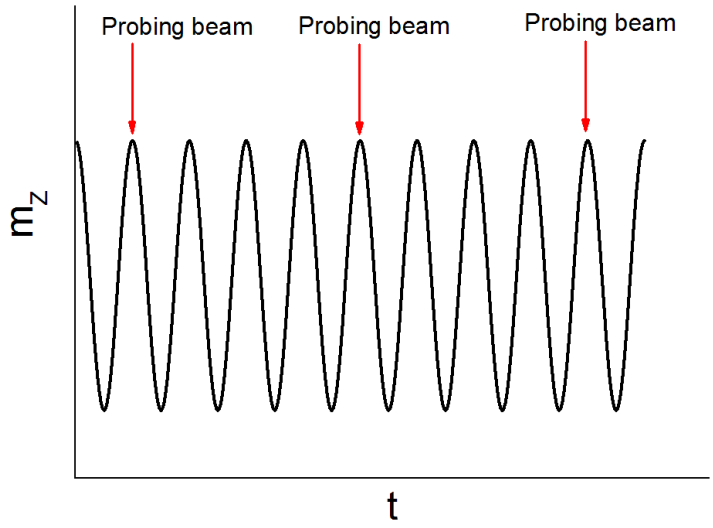

Fig 4.5.1 Time resolved mode of the MOKE measurements. The probing beam arrives at the same phase of the magnetization precession.

Experimentally we adjust and stabilize the shift between the probing beam and excitation field in the CPW. Since the phase shift between the excitation field and magnetization is fixed the condition for TR-MOKE is still fulfilled. In our setup it is realized in the following way (see Fig 4.5.2). The laser controlled by a Synchrolock unit emits light pulses with a repetition rate of 80 MHz. The actual pulsing frequency of the laser is measured by a fast photodiode and the feedback signal goes back to Synchrolock unit.

If the measured frequency differs from 80 MHz, the Synchrolock unit varies the cavity length of the laser to make it 80 MHz. The Synchrolock unit also has a reference signal output which is used as a reference for a signal generator. The delay line between the Synchrolock and the signal generator controls the phase shift. The signal from the signal generator goes through the CPW to the Oscilloscope that is triggered directly by the laser pulse. The PC reads the phase from the oscilloscope and calculates the phase shift with respect to the laser pulse. This phase shift can be controlled by applying a voltage to the delay line. If there is any difference between the desired and measured phases, the feedback signal is sent to the delay line to adjust it.

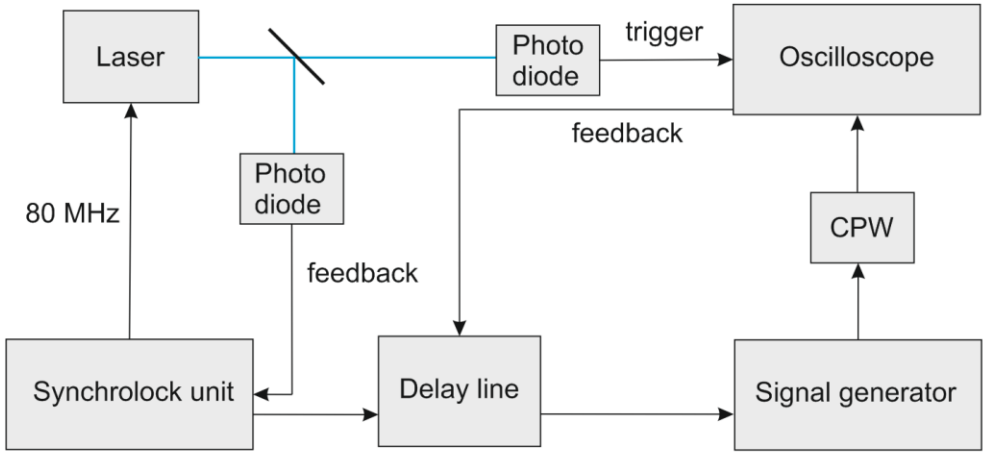

Fig 4.5.2 The phase stabilization system of the TR-MOKE setup. The phase shift between the probing beam and the microwave pulse is controlled by the delay line.

4.6 Sample preparation

The sample for the MOKE measurements is prepared in multiple steps. At the first step the YIG films are deposited on the gallium gadolinium garnet (GGG) substrate with magnetron sputtering. The GGG substrate is chosen since it has the closest lattice parameter to YIG, which allows to improve the interface quality. The thickness and surface roughness is controlled with X-ray diffraction and reflectivity measurements. Sputtering is performed in Argon and Oxygen atmosphere with a sputtering rate of about 1.74 nm/min. The base pressure is $2.6 \cdot 10^{-8}$ mbar and the pressure during deposition is $2.9 \cdot 10^{-3}$ mbar. The proportion between Argon and Oxygen during deposition is 5%. Subsequently, the samples are annealed in air at 850 ^{0}C. Then the YIG full films are obtained.

These samples can be already characterized with the FMR or SQUID measurements. However, for the MOKE experiments the CPW on top of the YIG must be patterned in order to drive the magnetization out of plane. This multi-step procedure combines electron beam lithography (EBL), thermal evaporation, ion beam etching and many other techniques. In this subchapter we describe the sample preparation process for two main experiments of this thesis: spin wave measurements and SHE measurements. The following figure explains step by step the preparation process of the sample for spin wave measurements. The figure is schematic, actual thicknesses proportion is not fulfilled.

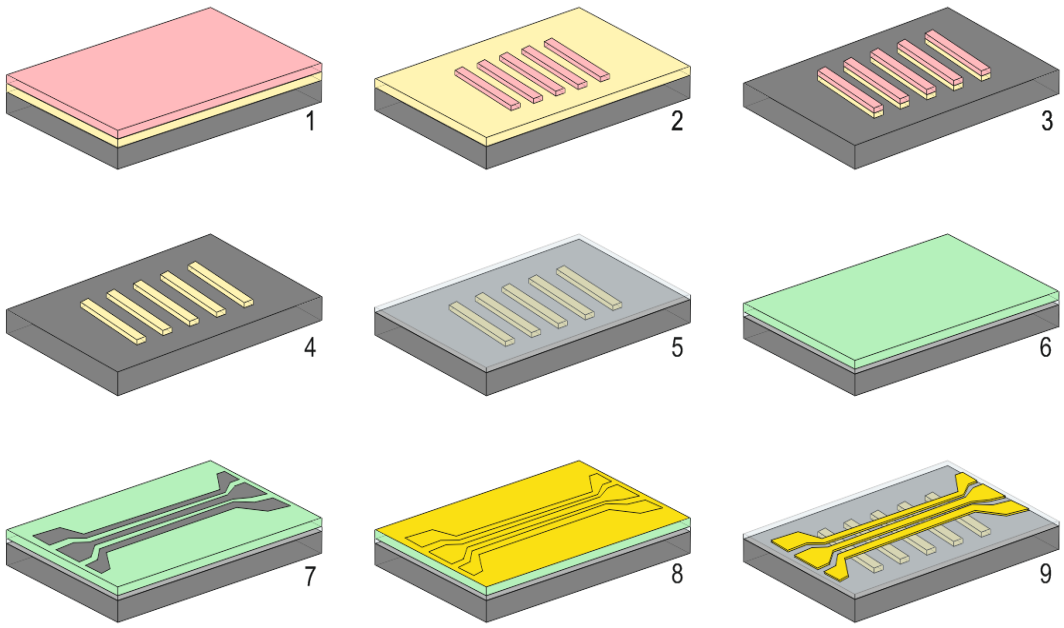

Fig 4.6.1 The step by step preparation process of the samples for the spin wave measurements. The GGG substrate is drawn in dark grey and the YIG film in light yellow color.

In step 1, the YIG/GGG film is covered with negative resist AR-N 7500-18 marked in pink color in the figure. The exposed part of the negative resist stays on the sample after development and protects the selected area. In step 2, electron beam lithography (EBL) is performed to draw the necessary structure on the resist. In our case it is an array of different width stripes, since the spin wave mode structure for different width is studied. Image 2 shows the sample after EBL and development steps. In our experiment a lot of stripes of different width are prepared to excite different spin wave modes. In step 3, sample etching in the chemical assistant ion beam etching (CAIBE) setup is performed, in order to remove all the YIG except of the resist covered ones. The etching is done with argon atoms at a pressure of 10^{-3} mbar, acceleration voltage of 5 volts, 5 amperes beam current with the etching rate of 4.5 nm/min.

In step 4, the sample is placed into the PG remover to remove the resist from the YIG stripes (image 4). In step 5, aluminum oxide (AlOx) is deposited on top of the sample for electrical isolation of the stripe from the CPW. The thickness of the ALD-grown oxide (Atom layer deposition) is varied from 10 to 25 nm depending on the thickness of YIG. In step 6, to fabricate the CPW, positive double layer PMMA resist is put on the sample. The double layer of the resist is put to improve the lateral quality of the future structure. The lower layer is the resist with smaller exposition dose PMMA 50K and the upper layer with higher dose PMMA 200K. The resist is marked green. In step 7, after the EBL the sample is developed and ready for CPW evaporation. In step 8, a golden CPW is evaporated on our structure. Before evaporation the sample surface is pre sputtered for a short time for cleaning purposes. Thereafter, we evaporate Ti/Au bilayer (5-10 nm Ti layer is put for better gold sticking, thickness of gold depends on the parameters of the CPW to match 50 ohm impedance). Step 9 is the lift-off process. The sample is put in acetone in order to remove all the resist with Au on it. The Ti/Au layer stays only in the resist free area (image 7). The sample after the lift-off is shown in image 9 and ready for measurements. It is glued on the sample holder and connected to the socket board with aluminum bond wires.

The sample preparation for the SHE-measurements differs insignificantly.

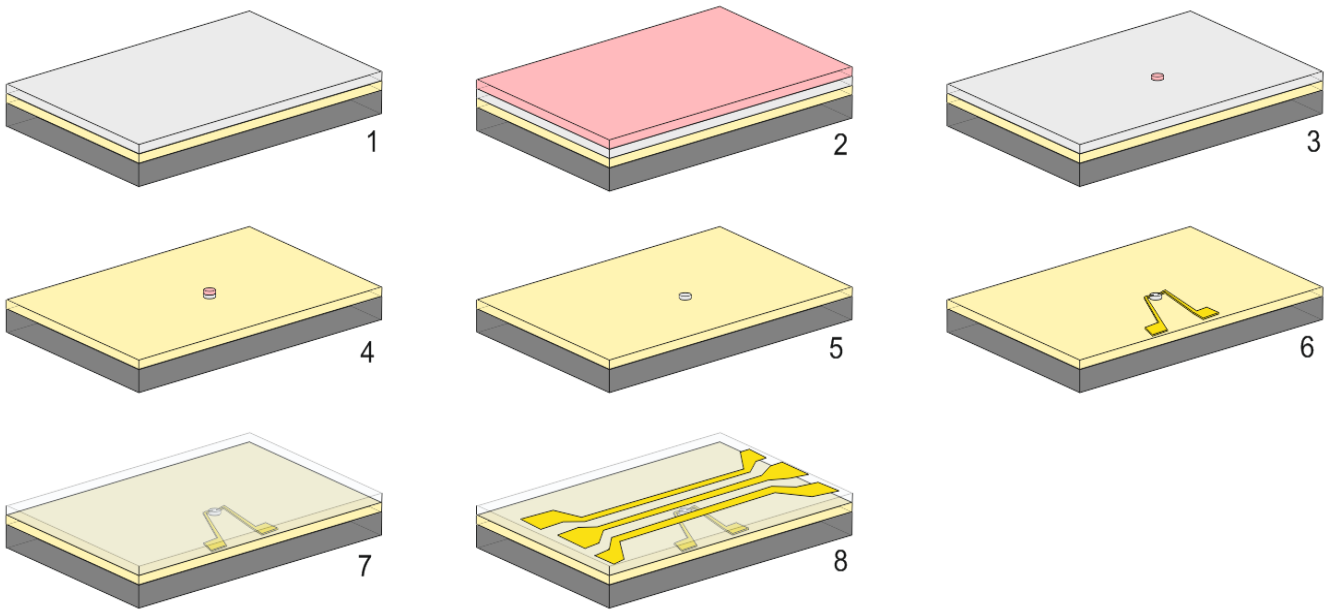

Fig 4.6.2 The step-by-step preparation process of the samples for the spin Hall effect measurements. The GGG substrate is drawn in dark grey and YIG film in light yellow color.

The preparation process is shown in Fig. 4.6.2. In step 1, a 10 nm Pt film is deposited on the YIG sample. Evaporation, sputtering and molecular beam epitaxy deposition techniques are used in different cases. In step 2, the sample is covered with negative resist, a structure is written with EBL and then developed (same procedure as for the spin wave sample). The structure has the shape of a small circle. The Pt structure should be very small to fit in the gap between the ground and signal line of the coplanar waveguide. The gap is about 5 μm, and the structure should be perfectly aligned in the center of the gap where the excited field is perfectly out of plane. In step 4, platinum is etched away. In step 5 the residuals of the resist are removed. In step 6 we deposit gold contacts for current application. This step consists of multiple processes: resist deposition, EBL, development, evaporation, lift-off see Fig 4.6.1 image 6-10. The contacts have a pointed shape and the gap between them is about 300 nm. This is made to obtain maximum current density. Afterwards we put AlOx for the same purposes as in spin wave samples. In the last steps the CPW is deposited on the sample. The Pt circle lies in the middle between the signal and ground line of the CPW. In this position the microwave excitation field of the CPW points normal to the sample surface. The sample is placed in the magnet in such a way that the bias magnetic field lies in the sample plane and is perpendicular to the CPW. In this case the vectors of the magnetic bias field, microwave excitation field and the current, that flows through the Pt circle form the right handed triple of vectors. This is one of the important conditions for successful SHE observation. We should note that the sample preparation process can vary depending on the task. The description given above is just the overview of techniques we used to prepare our samples. However, each part of experiment has its own sample preparation peculiarities, which are briefly described before each experimental result.

5. Experimental results

5.1 Sample characterization

In this sub chapter we perform the structural and magnetic characterization of the thin sputtered YIG. For this purpose 4 samples of different thickness (19, 29, 38 and 49 nm) are grown. The thickness of the samples is controlled by X-ray reflectivity (XRR). The XRR results are presented in figure below.

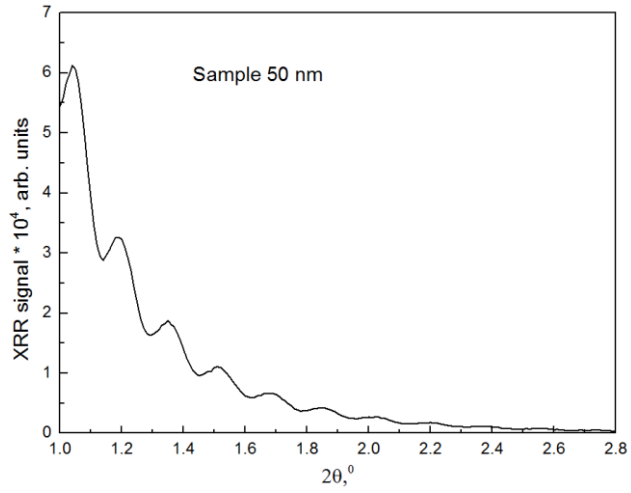

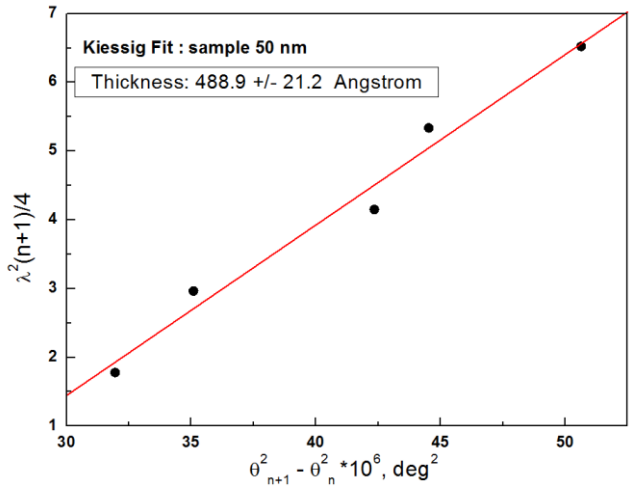

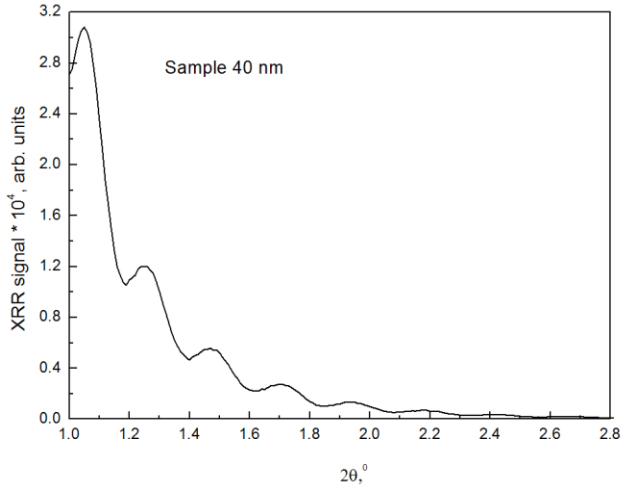

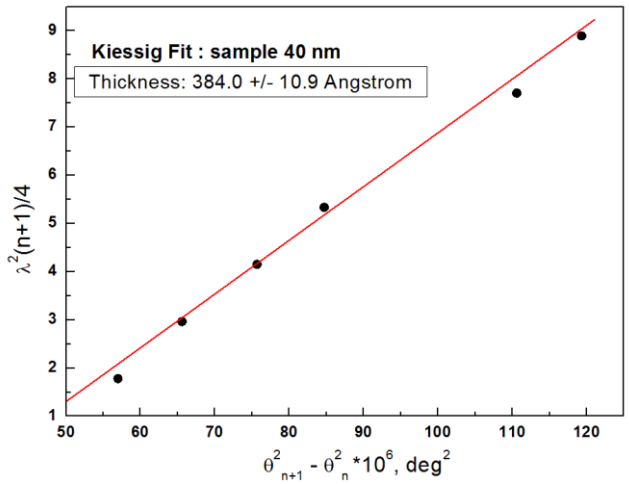

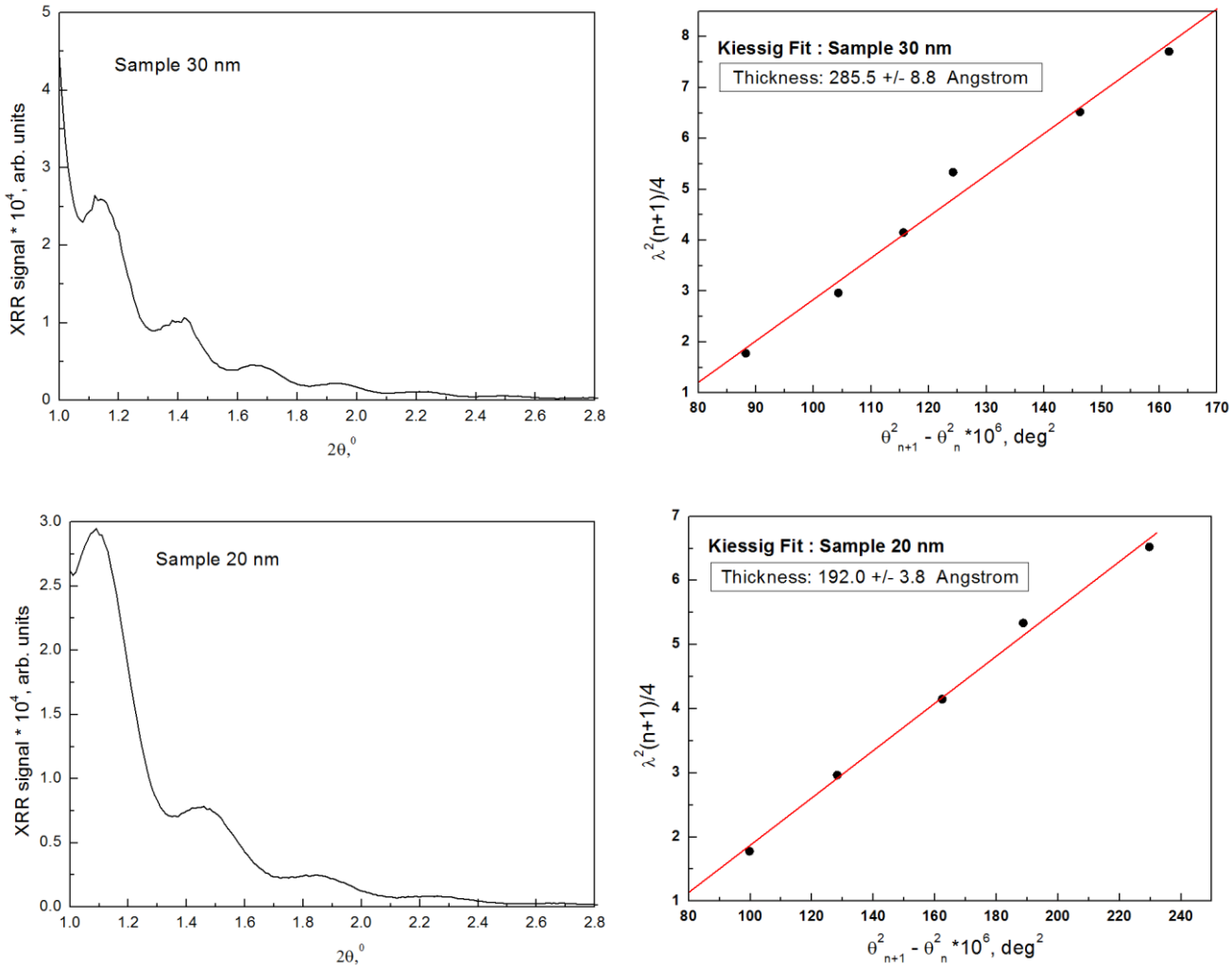

Fig 5.1.1 X-ray reflectivity dependence on the incidence angle and corresponding Kiessig fringes fit. The actual thicknesses of all samples are very close to the planned thicknesses.

The X-rays with wavelength of 1.54 nm fall on the sample at the small angle θ. Part of the beam reflects from the surface at the same angle. The transmitted beam also reflects from the interface between GGG and YIG. The total reflected signal has a maximum when Bragg's law condition is fulfilled:

$$n\,\lambda = 2\,d\sin\theta \tag{5.1}$$

where λ – wavelength of the X-rays, d- distance between two interfering layers (thickness), θ – angle between the X-ray beam and surface. Resulting dependence of the reflected signal on the angle between the incidence beam and the surface decays rapidly with periodic oscillations intensity called Kiessig fringes. This dependence carries information about sample thickness, (distance between neighbor

fringes) surface roughness (slope of the curve) and material density (offset of the decay). In our case we are interested only in the samples thickness. The surface roughness of the samples is measured by AFM and shows a value of 2.5 nm.

Subsequently, room temperature SQUID measurements are done to determine the saturation magnetization. The field is applied in the sample plane. Results of the measurements are presented in the figure below.

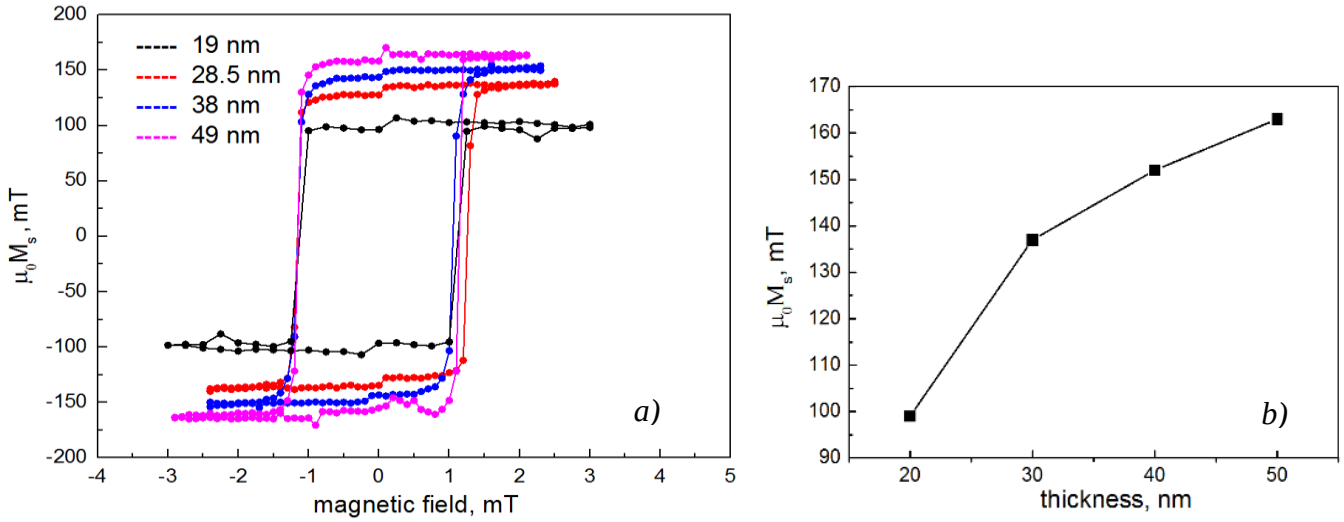

Fig 5.1.2 a) SQUID magnetization loops measured for all sample at room temperature. b) Dependence of the saturation magnetization on the sample thickness.

The saturation magnetization $\mu_0 M_s$ at room temperature is found to be around 163 mT for the 49 nm thick sample and decreases to about 99 mT for the 19 nm thick sample. For thinner samples the magnetization drops further (for 10 nm thick samples $\mu_0 M_s$ ~ 75 mT). The relative error in magnetic moment measurements is about 1 %. Another error is due to the inaccuracy in the measurements of the sample area. During the sputtering the sample is mounted with a kapton tape, the tape covers corners of the sample. This means that the full magnetic surface is smaller than the 8x8 mm^2 substrate. The area covered by the tape is measured with a ruler. One further inaccuracy comes from the presence of the non-magnetic dead layer. This layer is formed because of diffusion of the gadolinium from the substrate to the YIG film. It must be taken into account when calculating the effective sample volume. The thickness of this layer is typically 4-6 nm and it is subtracted from the initial sample thickness.

Thus, the value $\mu_0 M_s$ is calculated as follows:

$$\mu_0 M_s = \frac{\mathrm{M}}{(S_{sub} - S_{corners})(t_{sample} - t_{dead})} \tag{5.2}$$

where M is the total magnetic moment measured by SQUID, S_{sub} is the area of the GGG substrate being the same 8x8 mm^2 for all samples, $S_{corners}$ is the area covered with kapton tape during YIG sputtering, t_{sample} is the sample thickness measured by XRR, t_{dead} is the dead layer thickness. The relative error of magnetization measurements varies from 7% to 13% depending on the thickness of the film. The last step of sample characterization is measuring of FMR for all the samples. The setup used for measurements is CPW-FMR.

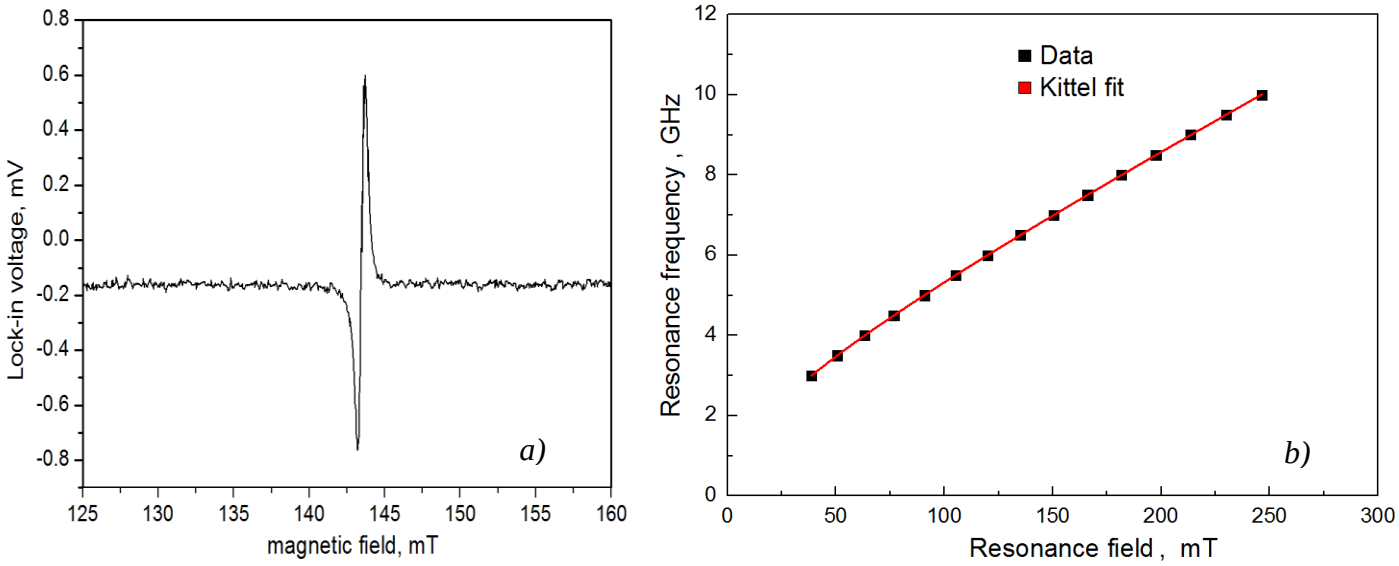

Fig 5.1.3 a) Typical FMR data set measured using lock-in detection and thus showing the derivative of the Lorentzian absorption line. (f=6 GHz). b) Dependence of the FMR frequency on the resonance field for a 38 nm thick sample measured at room temperature.

Dependence of the FMR frequency on the resonance field for the 38 nm sample is plotted in Fig. 5.1.3 b. Fitting it with the Kittel formula allows to extract the gyromagnetic ratio and effective magnetization of the sample. Subsequently, the anisotropy constant can be calculated by using the formula

$$K_{u1} = \frac{\mu_0 H_{anis} M_s}{2} = \frac{\mu_0 (M_{eff} - M_s) M_s}{2} \tag{5.3}$$

where M_{eff} is the effective magnetization extracted from the Kittel fit, M_s is the saturation magnetization measured by SQUID.

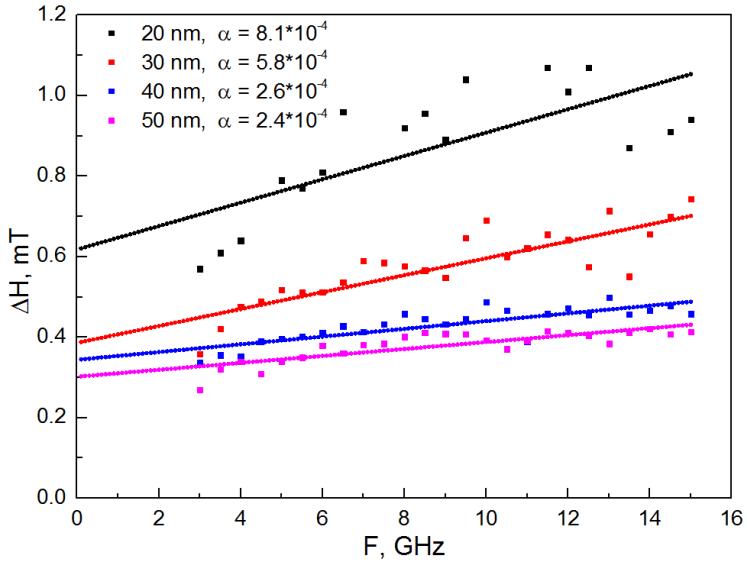

Fig 5.1.4 FMR line width as a function of frequency measured at room temperature for all the samples. The solid lines are linear fits to the data.

Gilbert damping should be strictly proportional to frequency while the zero frequency offset is related to extrinsic contributions to damping such as sample inhomogeneity's and two magnon scattering. Linear fits of the dependence of the FMR line width on frequency give us information about the Gilbert damping parameter. The summary of the sample characterization is presented in the table below.

	19 nm	29 nm	38 nm	49 nm
$\alpha \cdot 10^{-4}$	8±2	5.8±0.7	2.6±0.3	2.4±0.3
ΔH_0 (mT)	0.6±0.06	0.4±0.03	0.3±0.01	0.3±0.01
$\mu_0 M_s$ (mT)	100±8	140±10	150±10	160±10
$\mu_0 M_{eff}$ (mT)	209±1	222±1	227±1	237±1
K_{u1} (J/m^3)	4300±300	4600±300	4500±200	4800±400
g (GHz/T)	28.6±0.6	28.8±0.4	29.0±0.3	28.9±0.1

As can be seen the Gilbert damping rapidly increases with the decrease of the sample thickness. The anisotropy constant is approximately the same for all the samples.

5.2 Spin wave measurements

Following the full magnetic and structural characterization, the samples are patterned into arrays of YIG stripes using the methods described in sub chapter 5.1. The stripe width varies from 2 to 16 μm with step of 2 μm. This is done to study the mode structure dependence on the stripe width. The best spin wave images are recorded for the wide stripes. Since YIG and GGG are transparent materials some reflection layer should be put on top of each stripe in order to get some reflected signal. 8nm gold (Au) film with 3 nm titanium (Ti) is chosen as reflector. In Fig 5.2.1 the sample layout is shown.

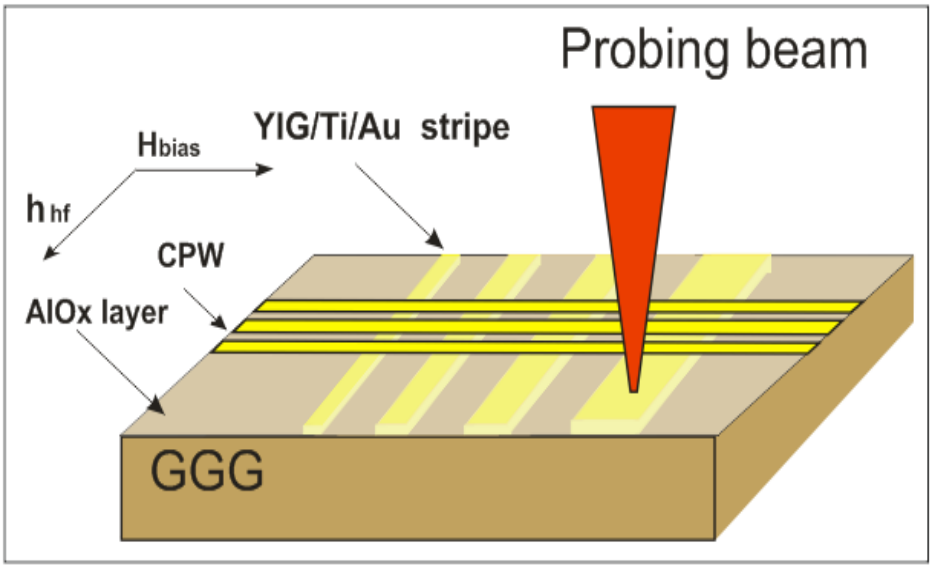

Fig. 5.2.1 A typical view of the sample lay-out. Spin waves are excited by the RF field of the CPW. The laser is focused on the YIG stripe and the sample is scanned using a Piezo stage. The directions of the bias and RF excitation fields correspond to the Damon Eshbach spin wave geometry.

The geometry corresponds to the excitation of Damon Eschbach spin waves. The frequency in all spin wave and spin Hall measurements is 6 GHz. This frequency corresponds to the maximum signal transmission in high frequency part of the MOKE setup. MOKE imaging of the stripes for different magnetic fields is performed. The step of magnetic field changing is 0.5 mT.

Figure 5.2.2 shows MOKE images of the spin waves recorded on the 14 μm wide stripe.

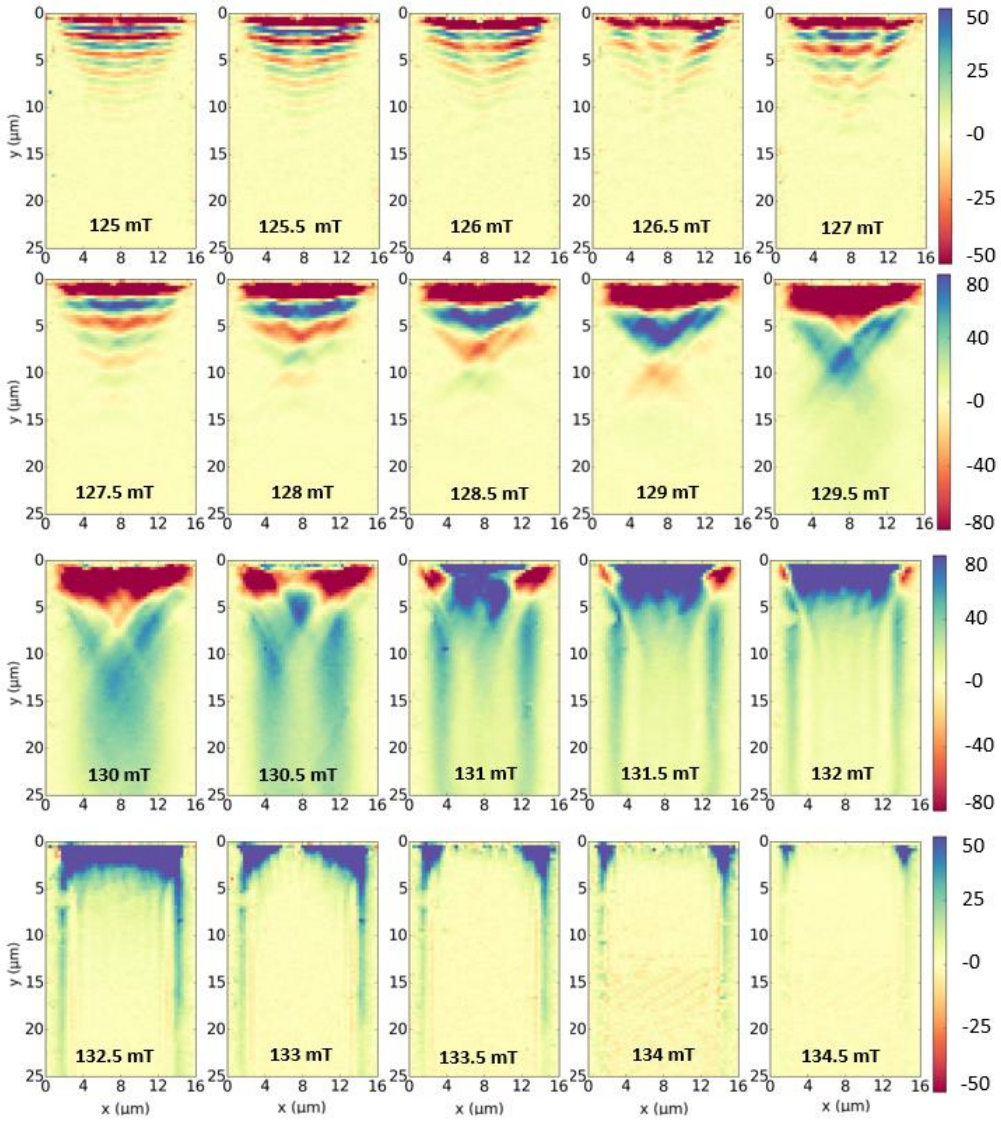

Fig 5.2.2 MOKE images recorded on the 14 µm wide stripe of the 49 nm thick YIG sample. The edge of the ground line of the CPW is placed on position y=0.

At the fields of 125 and 125.5 mT a pattern for the first spin wave is observed. At the fields from 128 to 129.5 mT the typical "X-shape" occurs, resulting from the superposition of the first and third SW modes. Approaching the resonance field at 132 mT a strong uniform excitation is observed in the region near the CPW and "edge" modes at the sample edge. With further increase of the field both excitations decrease. To support our measurements micromagnetic simulations are performed using the Mumax[54] code. We use the following parameters for the simulations $M_s = 1{,}3 \cdot 10^5$ A/m, $A_{ex} = 3.5 \cdot 10^{-12}$, $K_{u1} = 4.79 \cdot 10^3$ J/m^3, $\alpha = 2{,}8 \cdot 10^{-3}$. The results of the simulations are presented in the figure below.

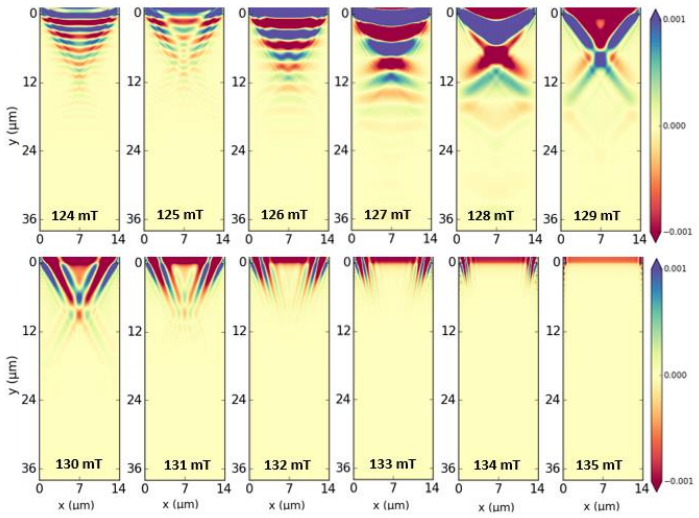

Fig 5.2.3 Simulations of the SW excited by a CPW for the 14 μm wide stripe.

As is seen in Fig 5.2.3, the simulations are in a very good agreement with the experimental data, with the exception of the stripe edges region where no excitation occurs. This mode appears in our experiments because a spurious transverse magnetic field is excited by the current running in the thin Ti/Au layer that covers the YIG film. This current is excited inductively by the CPW. To check this hypothesis SONNET simulations for our stripes are performed. SONNET is an EM simulator (using the method of moments) for every kind of planar structures like microstrip , stripline or coplanar circuits The current distribution in Y-directions is plotted in figure below.

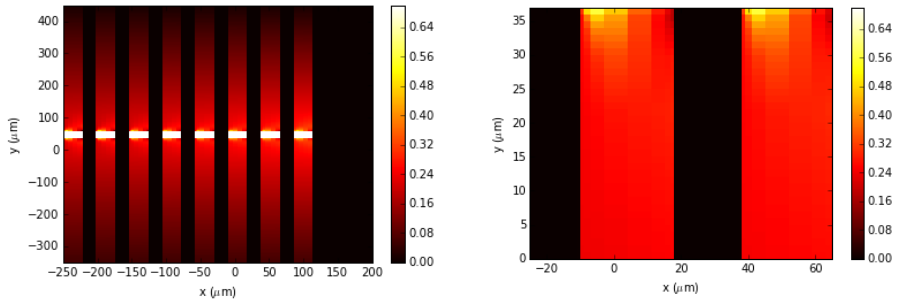

Fig 5.2.4 Sonnet simulations of the electrical current excited by CPW in Au/Ti stripes array. CPW and stripes are separated by 25 nm AlOx layer to prevent direct current flow. The right image is the simulation of the whole stripe array, the left image is the zoomed area between two stripes in the middle.

As indicated a non-zero current flows parallel to the YIG stripes. Obviously, it creates a transverse magnetic field not taken into account in the simulations presented in Fig. 5.2.3. In oder to consider it, new Mumax simulations for the 14 µm stripe excited by the homogeneous transverse field are carried out. The results are presented in the figure below.

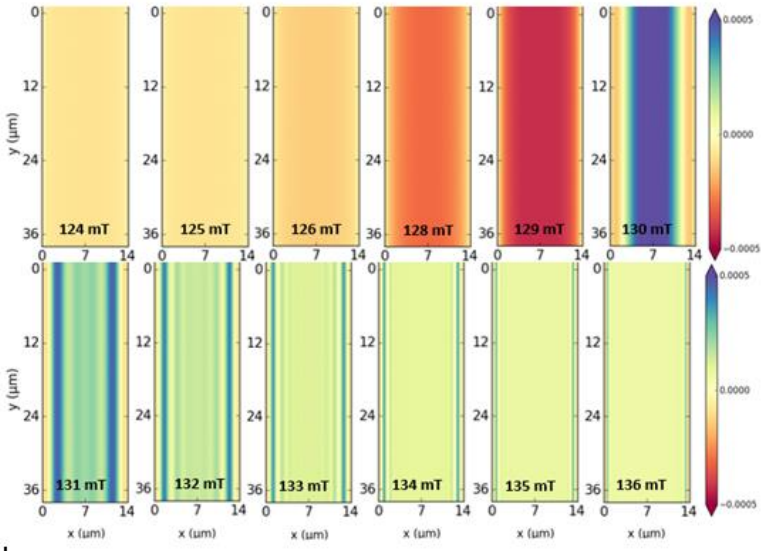

Fig. 5.2.5 Simulations of the edge modes excited by a homogeneous transverse field for the same stripe.

The presence of the edge modes at the same fields as in the experimental data is observed. The modes are excited by a homogeneous transverse field and have the same intensity over the Y-axis. In the spin wave experiments the intensity decreases with increase of the distance for the CPW. This makes sense since the current flowing in the stripes also decreases with the increase of the distance for the CPW. To compare the mode structure linescans along the X-directions for simulations and for experimental data are performed. For that we just plot z(y) dependence for a fixed position on the X-axis.

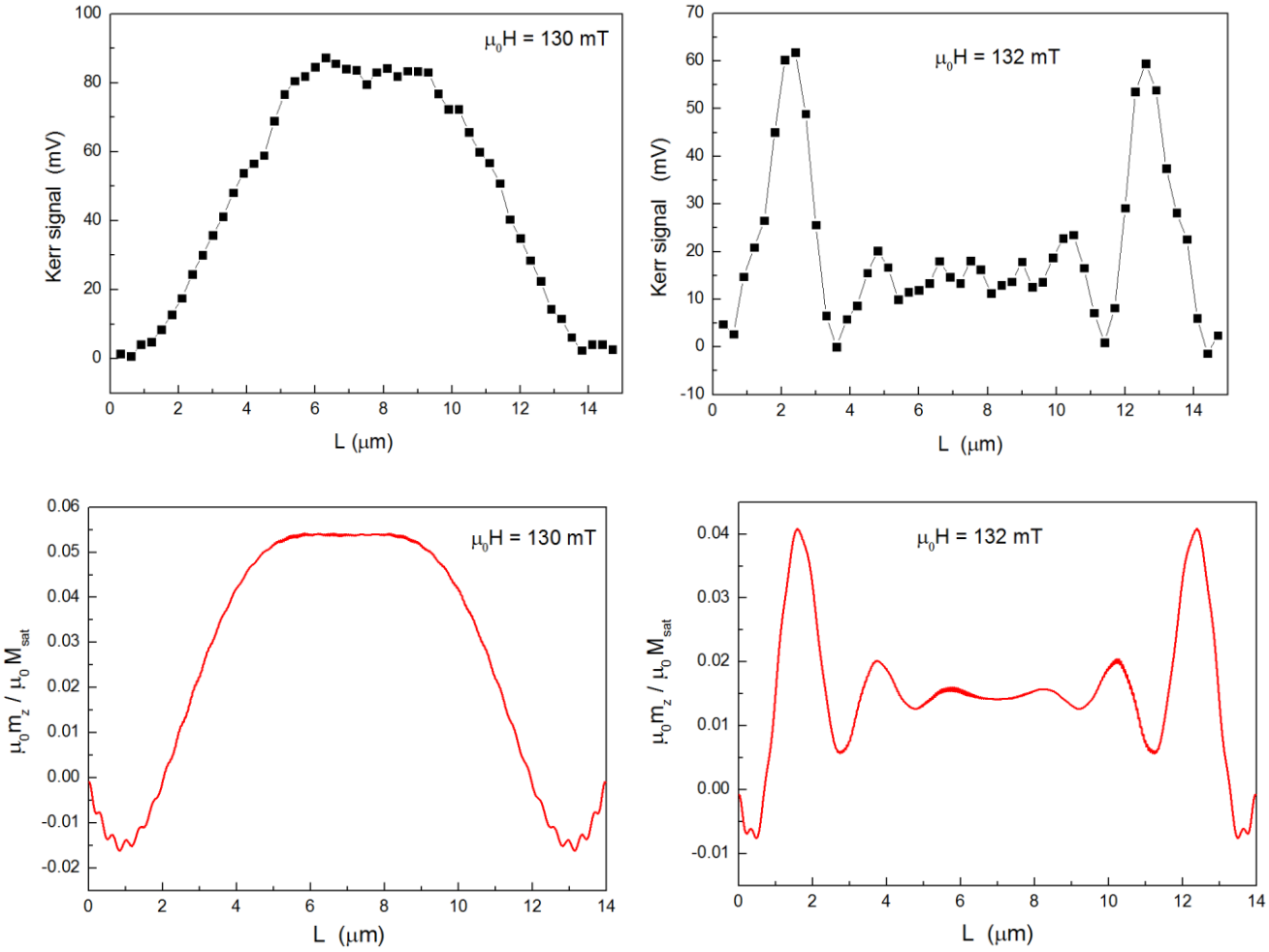

Fig. 5.2.6. Linescans in transverse direction of the experimental data (black dots) and MUMAX simulations (red solid line).

The linescans in X-direction show a high similarity in the mode structure between the experiment and the simulations. Thus, we claim that simulations are in a good agreement with experimental data. In order to characterize the damping of the spin waves the spin wave attenuation length for the first spin wave mode is calculated. To do this, the spin wave image of the first mode (Fig 5.2.2) is taken and the linescan inY-direction for each sample is made. Thereafter we fit obtained the linescan with a damped harmonic oscillator function.

$$z(y) = A_0 \sin(ky + f)\, e^{-y/L} + B_0 \tag{5.3}$$

Here A_0 is the initial spin wave amplitude, k is the wave number, f is the phase, L is the attenuation length, B is the offset.

The dispersion relation for DE spin waves can be written as follows:

$$\omega^2 = \gamma^2 \mu_0^2 \left(\left(H_0 + \frac{M_{eff}}{2} \right)^2 - \left(\frac{M_{eff}}{2} \right)^2 e^{-2kd} \right) \tag{5.4}$$

where M_{eff} is the effective magnetization, H_0 is the external magnetic field, d is the thickness of the sample, k is the wave vector and γ is the gyromagnetic ratio. An equation for the group velocity can be obtained from eq. 5.4.

$$v_{gr} = \frac{\partial \omega}{\partial k} = \frac{d\gamma^2 \mu_0^2 M_{eff}^2 e^{-2kd}}{4\omega} \tag{5.5}$$

From eq. 5.5. the spin wave attenuation length L can be calculated.

$$L = \tau v_{gr} = \frac{d\gamma \mu_0 M_{eff}^2 e^{-2kd}}{2\alpha\omega\left(M_{eff} + 2H_0\right)} \tag{5.6}$$

The attenuation length is a very important parameter characterizing the damping of the spin wave. Its value shows the spin wave propagation distance after which the amplitude of the spin wave drops by a factor of e. Assuming that for our sample thicknesses $e^{-2kd} \approx 1$, the attenuation length can be calculated using the SQUID and FMR data. As is seen from eq 5.6, the attenuation length is proportional to the effective magnetization M_{eff} and to the sample thickness d. Taking into account, that M_{eff} drops with the decreasing d, we expect a rapid decrease of the attenuation length with the sample thickness.

In Fig. 5.2.7 linescans for different thicknesses measured at an excitation frequency of 6 GHz are shown.

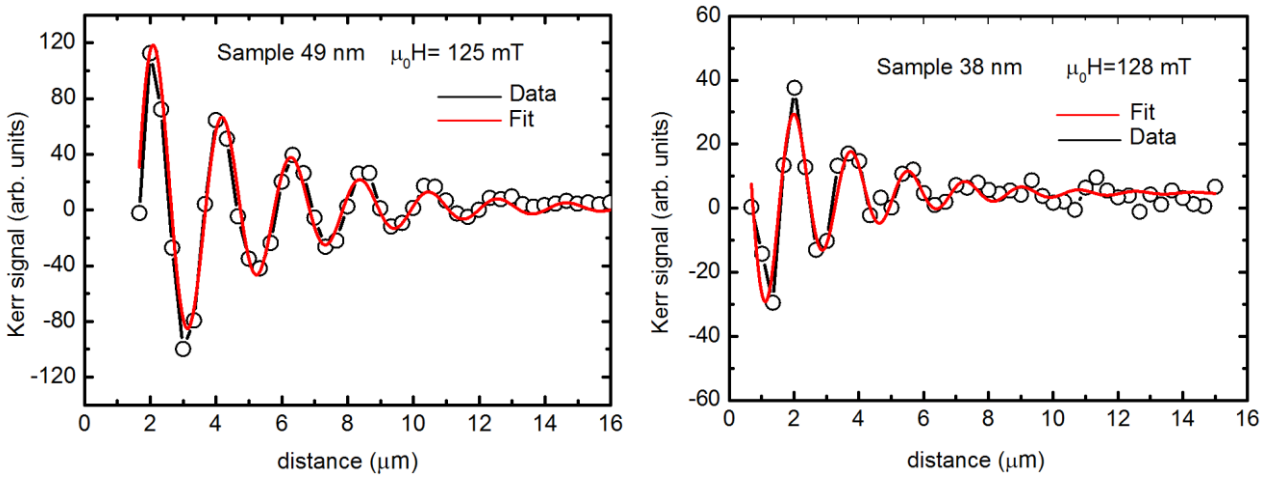

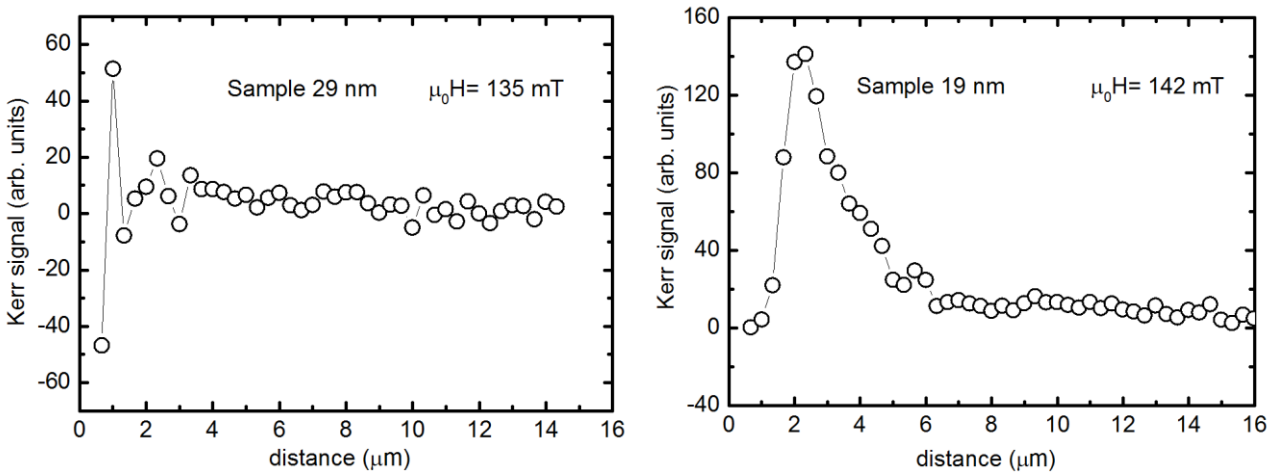

Fig. 5.2.7 Dependence of the spin wave amplitude on the distance from the CPW. All measurements are performed for 6 GHz excitation frequency.

As expected, the attenuation length L drops with decreasing thickness of the sample. For the 29 nm thick sample the oscillations become aperiodic and for 19 nm are not excited at all.

The summary of the spin wave attenuation length measurements and corresponding fits are presented in the table below.

	L_{att} fitted from the images (μm)	L_{att} calculated from equation 5.6 (μm)
Sample 38 nm	2.7±0.2	3.0
Sample 49 nm	3.6±0.2	3.7

It is significant, that for the fitting the value of the Gilbert damping parameter α= 0.002 is used. It is approximately 10 times larger than α measured in FMR experiments (see fig 5.4.). The reason is that the Ti/Au layer significantly alters the magnetic damping of the system by acting as a spin sink. Apparently, the interface between YIG and the Ti/Au bilayer has a descent spin pumping, which increases the total damping. A detailed study of this effect is provided in the next sub chapter. However, to prove this hypothesis, comparative measurements of the spin wave attenuation length for different materials are performed. To do this a single 25 nm thick YIG film with deposited stripes of different materials is taken. Thus, the same initial magnetic properties for all stripes are guaranteed. The first stripe is prepared from Ti 3 nm /Au 8 nm bilayer as reference one. The width of each stripe is 10 μm. The second stripe is made of aluminum with thickness of 20 nm. As aluminum is a very light metal, it correspondingly has a very low spin-orbit coupling. For aluminum longer spin wave propagation and larger attenuation length

are expected. Several nanometers of aluminum layer on top of the film oxidize and form Al/Alox bilayer. It is not very crucial, since even 10 nm of metal layer is sufficient to get some reflected light. The third stripe is prepared from MgO 5 nm /Au 10 nm bilayer. The 5 nm thick MgO layer lying underneath should prevent the spin pumping into the Au layer. For this stripe we expect larger spin wave attenuation length than for the reference Ti/Au stripe. The sample layout is presented in the figure below.

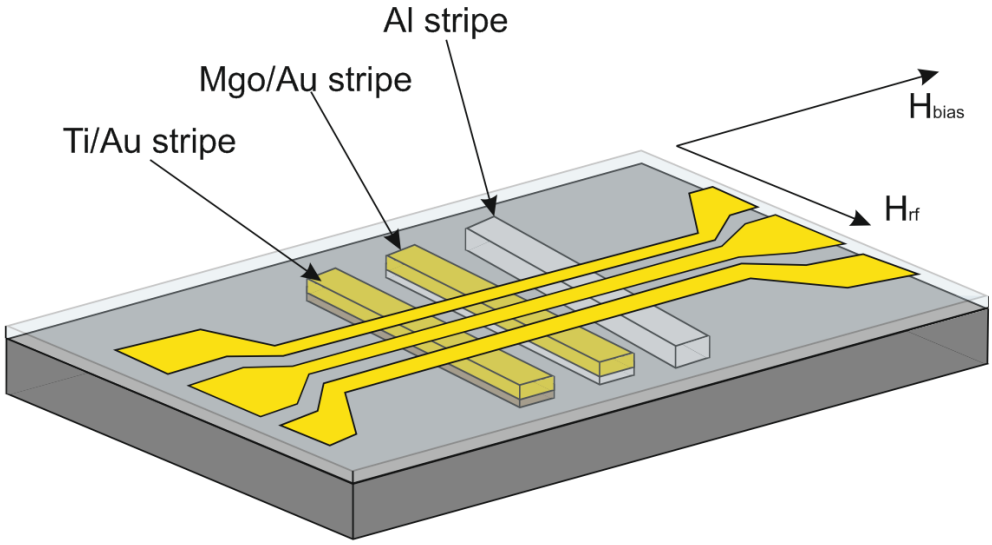

Fig. 5.2.8 Sample layout for spin wave comparative measurements. The field geometry corresponds to excitation of Damon-Eshbach spin waves.

The results of the comparative measurements are presented in figure 5.2.9.

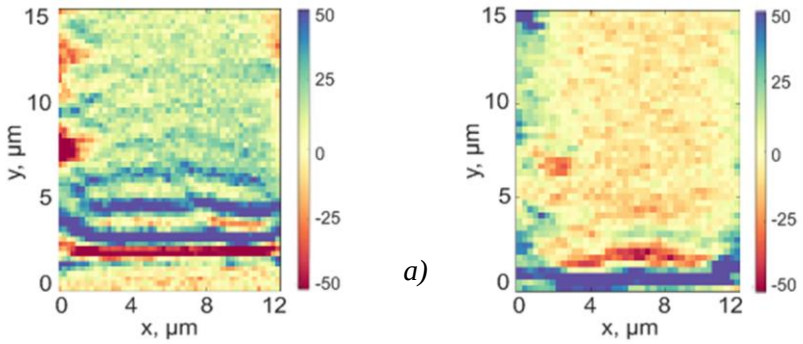

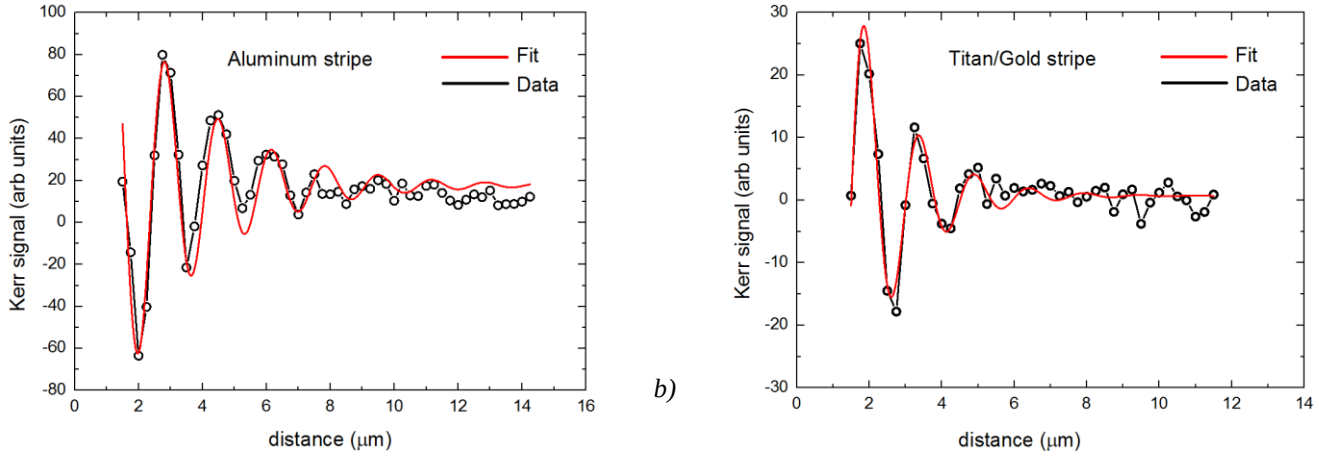

Fig. 5.2.9. a) Spin wave imaging on the Al (left) and Ti/Au (right) stripes. The excitation frequency is 6 GHz. The spin wave propagates further for the Al stripe, as expected. b) The Y-direction linescans with fitting of the upper images. The values for the attenuation length obtained from linescans fit are 2.8±0.3 μm for Al and 1.5 μm±0.2 for Ti/Au.

As expected, the attenuation length with the Aluminum layer is much larger than with the Ti/Au. Unfortunately, we have not measured the spin wave attenuation length for the stripes covered with MgO/Au. The reason for this are strange reflection conditions that occurred on these stripes. In figure 5.2.10 the topography images of MgO/Au (left picture) and Ti/Au stripes (right picture) are shown. The maximum reflection signal is in the CPW region (blue area at the bottom of the image). The thickness of the CPW is 150 nm.

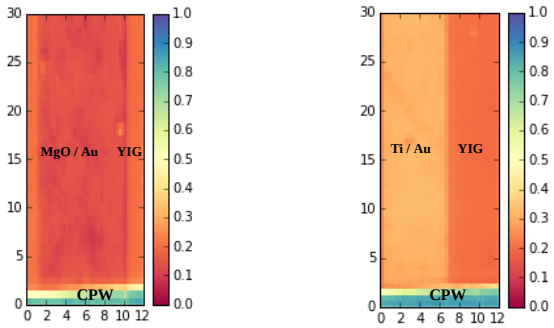

Fig. 5.2.10 Unusual change of the reflection in the area of YIG/MgO/Au. The reflected signal in this area is much weaker than on the pure YIG film.

The reflected signal of the YIG surface has an intensity of 0.2-0.22 a.u. As expected, the reflected signal from the Ti/Au surface is much larger: 0.39-0.43 a.u.

However for MgO/Au stripes the reflected signal is even smaller than for the uncovered YIG surface (0.11-0.13 a.u). Though MOKE images for MgO stripes are measured, these results can not be considered trustworthy since it is not clear how the extra MgO/Au layer on top of YIG can reduce the reflection. This effect is similar to an anti-reflection coating. However, the film thicknesses do not match the condition $d_{film} = \frac{n\,\lambda_{laser}}{4}$. A more probable reason is just some error in the stripe preparation process. Nevertheless, the comparative measurements of the spin wave attenuation length on YIG/Ti/Au and YIG/Al show that Ti/Au is a rather poor choice for capping layer because it alters the magnetic damping in the interface.

An attempt is made to optimize the spin wave experiments by finding the best thickness of the reflective layer. For that a big array (over 100) of the Au stripes on top of thick 150 nm YIG film is prepared. The gap between the stripes is 6 μm. The thickness of the Au layer varies from 1 to 36 nm with step of 0.3-0.5 nm. Under each Au layer there is 3 nm of Ti. Even though the Ti layer increases the damping it is suitable for comparison measurements. Here the optimal thickness of Au for the MOKE is measured, therefore the absolute value of the damping is not so important. The details of the sample preparation are shown in figure 5.2.11.

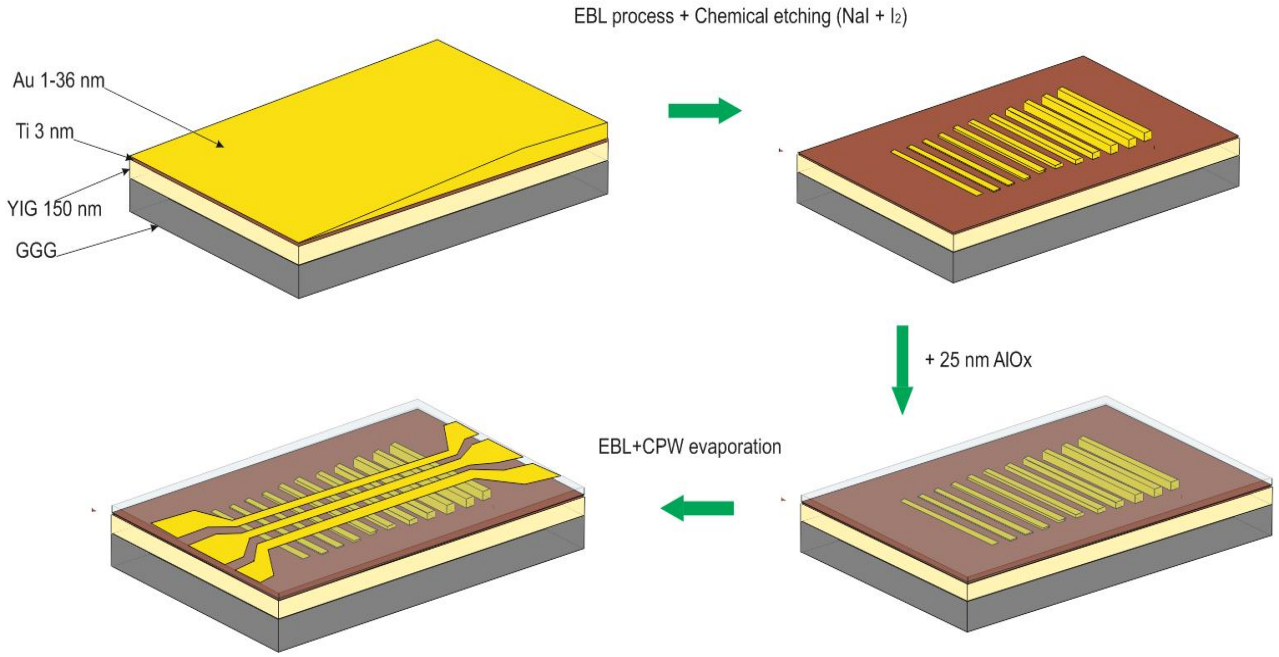

Fig. 5.2.11 The sample preparation process for the MOKE experiments optimization.

Initially the gold layer is grown on top of YIG/Ti bilayer. The stripe patterns are drawn with EBL and then after development process the gold is etched away with NaI + I_2 solution. The etching rate at room temperature is 1.5 nm/sec. This solution does not interact with the Ti layer. Thereafter, we put AlOx insulation layer and prepare the CPW on top of it.

The 3 nm Ti layer is grown by thermal evaporation. Before deposition of the Au layer, the sample is pre-sputtered for 1 minute. The Au layer is grown by MBE since it is the only setup capable to grow wedge type material. This is realized by a slowly moving shutter that partially covers the sample at the beginning of the evaporation process. During the process the shutter moves, slowly exposing more and more of the sample area. As a result, material grown with a slope is obtained. The angle of the wedge depends only on the speed of the shutter. Thereafter we prepare an array of stripes and the CPW for spin wave excitation with standard methods described previously. At first the spin wave imaging in the area with very thin (about 1.5 nm) and thickest (36 nm) stripes is performed. All images are recorded at the frequency of 6 GHz and magnetic field 122 mT. The scanning area is varied for different images. Results of the measurements are presented in figure 5.2.12.

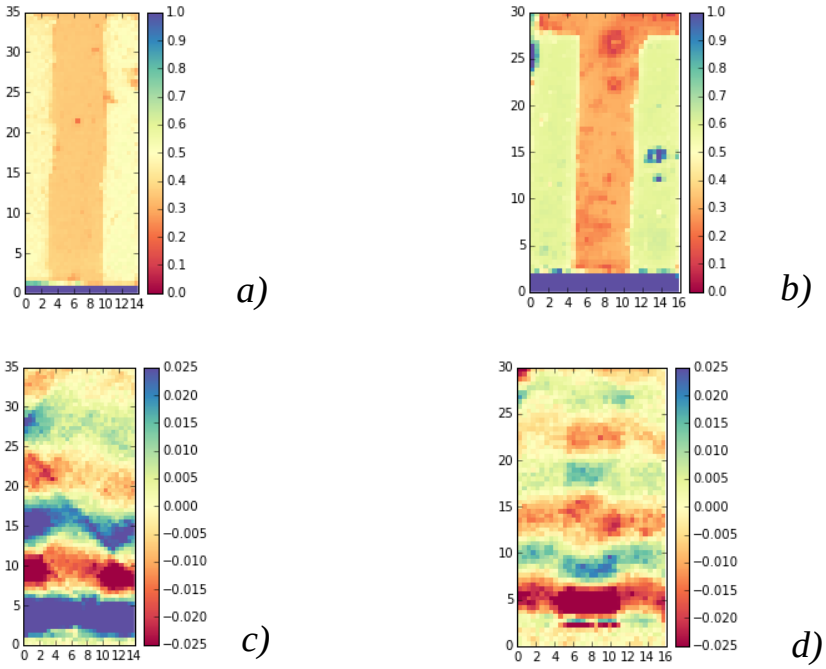

Fig. 5.2.12 a) Topography image of 2 thin stripes and the gap between them. b) Topography image of 2 thick stripes and the gap between them c) and d) corresponding Kerr images. The spin waves can be seen better on the stripe for the thin stripes and in the gap for the thick stripes. This means there is a certain thickness between 1 nm and 36 nm that corresponds to the best conditions for spin wave observation.

To find the optimal thickness of the reflecting layer the FMR spectra in the gap of the coplanar waveguide is measured. Here the term “gap” means the gap between the signal line and the ground line of the CPW, not the gap between two Ti/Au stripes. However, during the measurements the problem occurs that the amplitude of the FMR signal measured by MOKE strongly depends on the measurement position (see Fig 5.2.13). For example the FMR amplitude measured in the point B can be different from the amplitude in the point C. The reason is that transmission of the CPW is not the same all over its length, causing additional reflections of the microwaves, e.t.c.

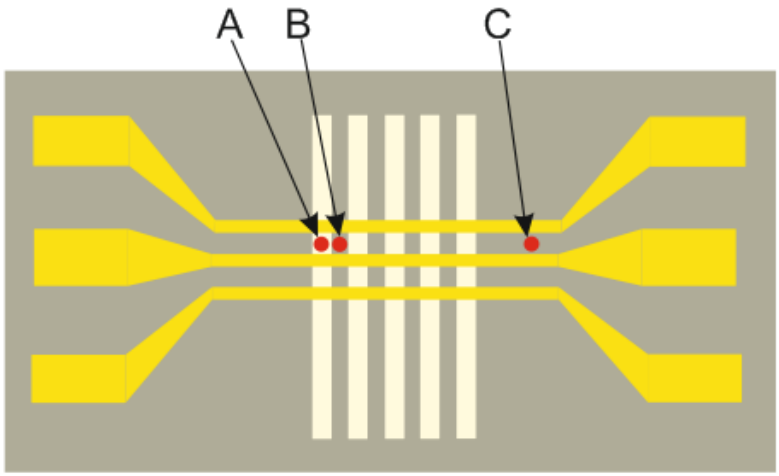

Fig 5.2.13 Sample layout for the measurements of the optimal thickness of the reflective layer. Red circles mark different measurement positions. To exclude an error coming from the transmission change over the CPW length, the ratio between FMR amplitudes in the stripes gap (point “B”) and on the neighbor stripes (point “A”) is measured.

In this case the measurement of FMR amplitudes on the stripes of different thickness and subsequent comparison make no sense. Thus, the ratio between amplitude in the gap between the stripes to amplitude on the stripe is measured. Since the thickness of the Ti layer is same everywhere the FMR amplitude in the gap depends only on the excitation efficiency. Assuming this efficiency is the same for the gap and for the neighbour stripe, the ratio FMR_amplitude_gap / FMR_amplitude stripe can be measured. We claim that this ratio is independent on the measurement position. We can call this normalized amplitude of the FMR. By measuring this ratio for different stripes thickness dependence of this ratio on thickness of reflecting layer is built. The minima of this dependence corresponds to the optimal thickness. The typical FMR spectrums measured with MOKE are shown in figure 5.2.14

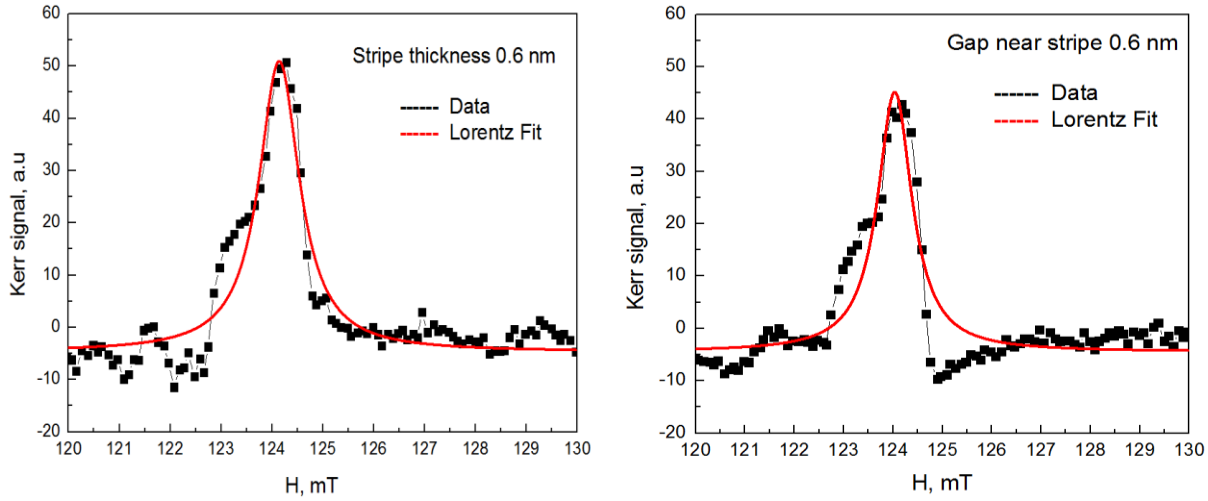

Fig. 5.2.14. FMR curves measured with MOKE on stripe (left image) and in the neighbour gap. Experimental curve (black dots) is fitted with Lorentz curve (red solid line).The amplitude is estimated as difference between the y- offset and the value in the peak of the function.

The FMR spectra is fitted with Lorentz curve $y = y_{offset} + \frac{2A}{\pi}\frac{\Delta H}{(4(H-H_{res})^2+\Delta H^2)}$

here ΔH is the FMR linewidth; H_{res} is the resonance field, A is the area under the curve, y_{offset} is the y-axis offset of the curve. The magnetic field H is an independent variable. The amplitude as the difference between the y-axis offset and peak value of each curve is estimated. The summary of the measurements is presented in figure 5.2.15

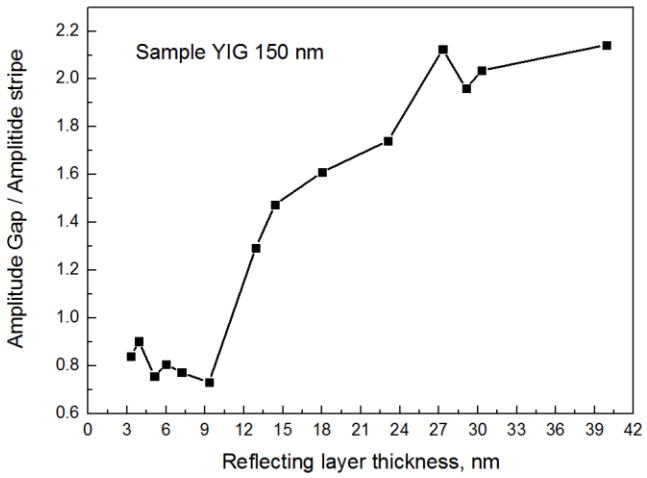

Fig. 5.2.15 Dependence of the normalized FMR-amplitude on the thickness of the reflecting layer. The optimal thickness of reflecting layer lies between 6 and 10 nm.

It significant, that the real FMR experimental curve shown in Fig. 5.2.14 does not have the perfect Lorentz shape, so the accuracy of these measurements is not very high. These measurements show that the optimal thickness lies somewhere between 6 and 10 nm. Nevertheless, these measurements have shown that the thickness of the reflecting layer used in all our spin wave experiments is close to optimal. Another interesting feature shown in these measurements is a possibility of spin wave imaging through a relatively thick metal layer. Figure 5.2.12 d) shows that the spin wave pattern is clearly seen through almost 40 nm (3 nm Ti + 36 nm Au) metal layer. The question arises whether we probe directly the spin waves in YIG film with the laser through a thick metal layer, or it is a spin accumulation signal in Au layer created by the spin pumping from YIG film.

5.3 Spin pumping in YIG/Ti interfaces

In the previous sub-chapter various spin wave propagation experiments are performed using thin Ti/Au bilayers as reflective layers. However, the spin wave attenuation length indicates that the Gilbert damping parameter of YIG changes drastically after depositing Ti/Au on top of the film. This can happen in case of large spin pumping into the Ti film. This result is rather unexpected since titanium is a relatively light metal compared to gold and platinum which traditionally show large effects of spin pumping. To check this, a detailed study of the YIG/Ti interfaces with ferromagnetic resonance is performed. The Gilbert damping parameter for two sample thicknesses 40 and 50 nm is measured. The 8x8 mm^2 sample is taken and cut into four pieces. For convenience we will call them S1, S2, S3, S4. For each sample the dependence of the FMR-linewidth on the frequency is measured and the Gilbert damping parameter is extracted. Thereafter 25 nm of AlOx is put on top of S2 and S4. This layer is put as a buffer layer to prevent spin pumping to the metal layers which are deposited later. For S2 and S4 the Gilbert damping parameter is measured once again. As expected, just the AlOx layer does not change the damping. Finally, we deposit 10 nm of Au on samples S3 and S4 and 10 nm of Ti on samples S1 and S2. Thus, we get one sample where Au is deposited directly on YIG and one where it is separated with AlOx layer. The identical sample pair for titanium is prepared. The sample preparation process is presented in figure 5.3.1

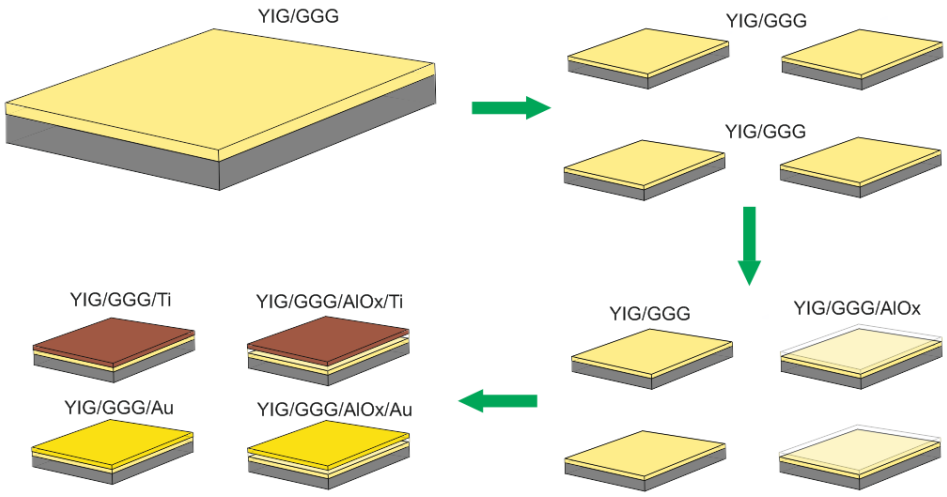

Fig. 5.3.1 The sample preparation process for spin pumping measurements. After each preparation step the Gilbert damping parameter is measured.

Thereafter, the Gilbert damping for each sample is once again measured. Results of the measurements are presented in figure 5.3.2.

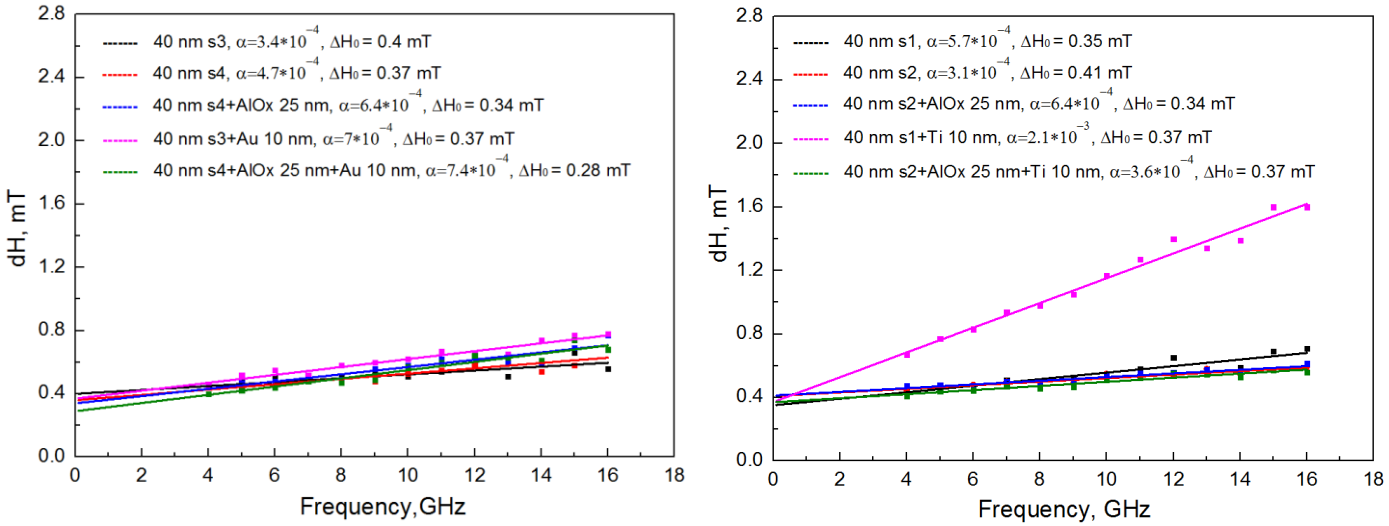

Fig. 5.3.2 Dependence of the FMR linewidth on resonance frequency for the 40 nm sample. A big change of the Gilbert damping occurs only in case when Ti is in direct contact with YIG. When it is separated by the AlOx layer the damping remains unchanged. Thin Au layer does not influence the damping.

The same measurements for the 50 nm YIG sample are repeated. The results are quantitatively the same.

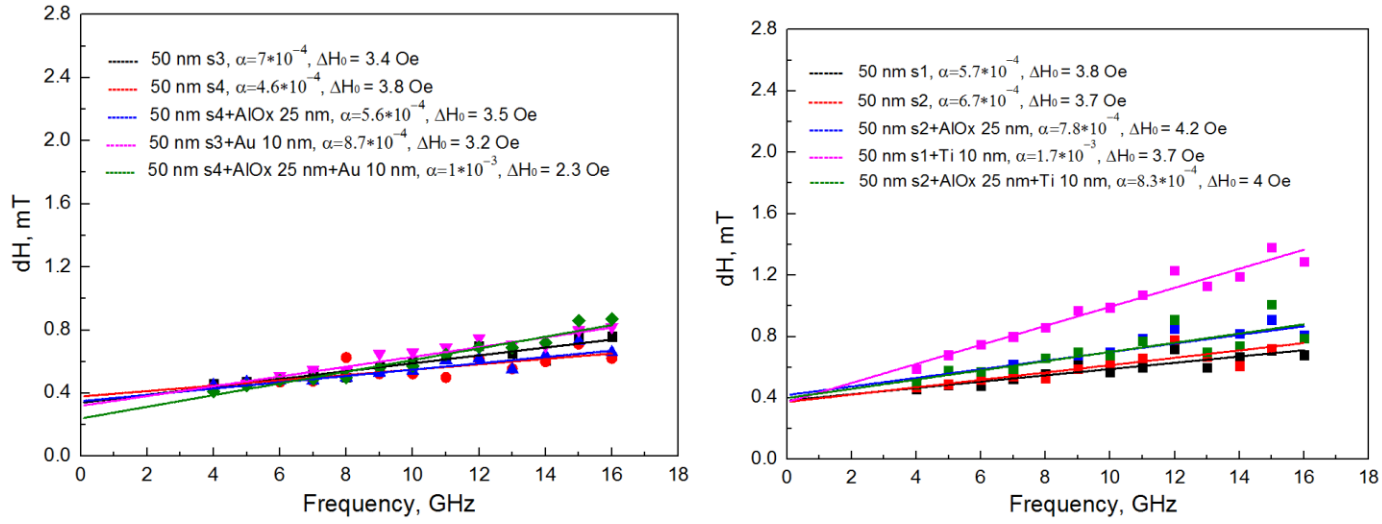

Fig. 5.3.3 Dependence of the FMR linewidth on resonance frequency for 50 nm sample. As previously the biggest change of the damping occurs in case of YIG/Ti interface.

These measurements prove our hypothesis about the spin pumping in thin Ti films. The Gilbert damping parameter measured by FMR for YIG/Ti films $\alpha \approx 0.002$ is in a very good agreement with Gilbert damping parameter measured in spin wave experiments. The spin-mixing conductance for YIG/Ti bilayers is calculated using the formula 5.7

$$G_{eff} = \frac{d\mu_0 M_s(\alpha_{YIG/Ti} - \alpha_{YIG})}{g\mu_B} \tag{5.7}$$

An evaluation using equation 5.7 with the parameters (M_s = 152 mT, thickness d = 40 nm, electron g-factor g = 2, μ_B – Bohr magneton) leads to an effective spin mixing conductance of. $4.1 \cdot 10^{17}$ m^{-2} which is approximately three times smaller than for YIG/Pt interfaces[55]. The resistance of the Ti film is measured with a four probe method. The obtained resistivity turns out to be extremely high and has a value of $3.58 \cdot 10^{-6}$ Ω·m. The literature value for the bulk titanium is $4.2 \cdot 10^{-7}$ Ω·m.

Since large spin pumping is present in YIG/Ti we perform Inverse spin Hall Effect (ISHE) measurements for our samples. The typical structure for ISHE experiment is shown in figure 5.3.4

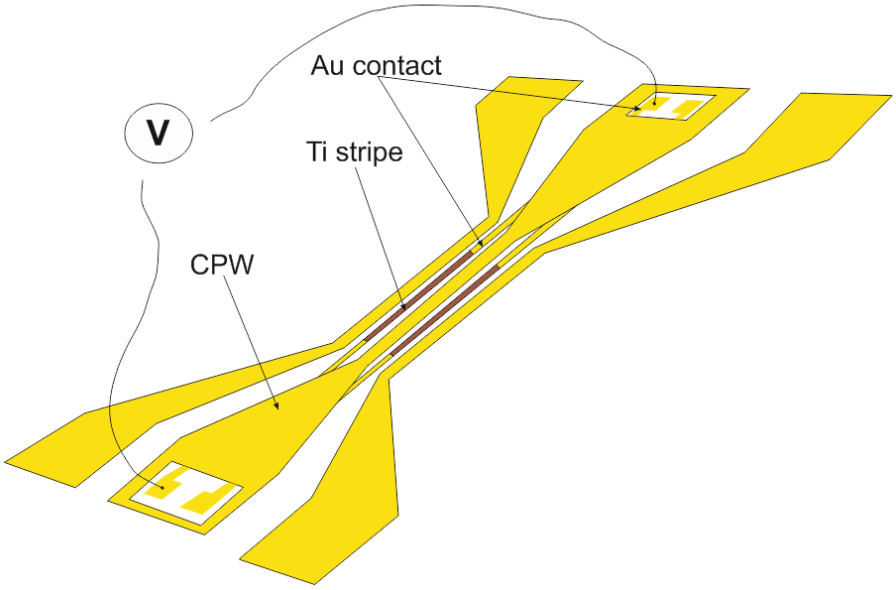

Fig. 5.3.4 The sample layout for ISHE measurements. The YIG/Ti stripe is placed in the gap between the signal and ground line of the CPW.

The spin pumping in YIG/Ti bilayer should result into a spin accumulation at the interface, and measureable ISHE voltage. Unfortunately no ISHE created voltage measured for this sample.

5.4 Spin Hall effect measurements in thin sputtered YIG films

Measurements of the SHE in YIG/Pt bilayers has several objectives. First, we want to study the influence of the current flowing through the Pt layer on the FMR in YIG. The idea is to manipulate the Gilbert damping in YIG[56] with SHE as it was done for other magnetic materials[10 11] and to calculate the spin Hall angle for Pt. In the experiment the FMR linewidth of YIG is tuned by an electrical current flowing in Pt and measured optically by MOKE. The second objective is to reduce the Gilbert damping to zero and observe the onset of the autooscillations[57 58 59]. The experimental sample consists of Pt circles[57] with Au current contacts. This structure is placed between signal line and ground line as it was described in the sample preparation part. We measured the dependence of the linewidth on the applied current for two current polarities for a YIG 30 nm/ Pt 12 nm sample. The results are presented in Fig 5.4.1

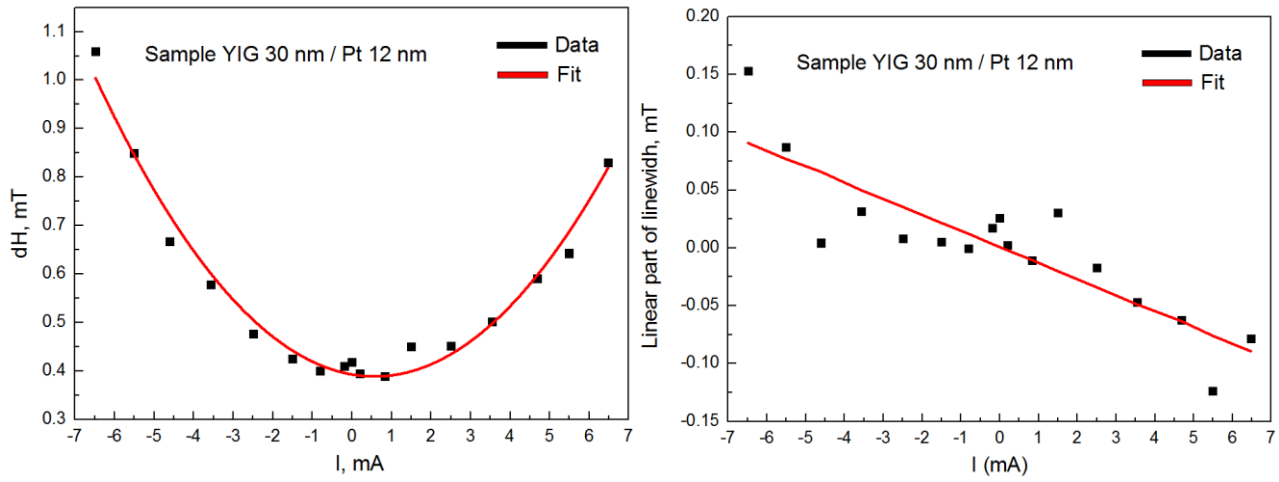

Fig 5.4.1 A) Dependence of the linewidth on the applied current for two current polarities (black dots) and its fit with a second order polynomial $dH = AI^2 + BI + C$ (red line). B) Linear part of the first graph plotted by subtracting the quadratic part and the offset from the raw data. The linear part corresponds to the SHE contribution.

Here, the dependence of the FMR-linewidth on the current has a parabolic form. The linewidth is fitted with a second order polynomial $dH = AI^2 + BI + C$, where I is the applied current. The quadratic part of the polynomial corresponds to Joule heating that is present in the system. Heating effects in SHE experiments are parasitic since heat destroys ferromagnetic ordering. Unfortunately, for these samples the influence of heat is very high since gallium gadolinium garnet is a poor heat sink. The linear part of the polynomial corresponds to the SHE and carries the information about the SH-angle.

To calculate the spin current density we use the formula derived in sub chapter 3.7.

$$dH = dH_0 + dH_{SHE} = \frac{\omega}{\gamma}\left(\alpha + \frac{\hbar j_s}{d\mu_0 M_s e\left(2H + M_{eff}\right)}\right) \tag{5.8}$$

where $\gamma = 28\frac{GHz}{T}$ is the gyromagnetic ratio, d is the thickness of the YIG layer, ω the rf frequency, M_s and $M_{eff}$the saturation and effective magnetization, j_s the spin current density, e the electron charge, ħ thereduced Planck constant.

Knowing the spin current density, the spin Hall angle θ can be extracted.

$$\theta = \frac{j_s}{j_e} = \frac{t\mu_0 M_s e\left(2H + M_{eff}\right)}{\omega\hbar}\frac{\gamma d H_{SHE}}{j_e} \tag{5.9}$$

where j_e is the electrical current density, μ_0 the vacuum permeability. The second term $\frac{dH_{SHE}}{j_e}$ can be extracted directly from the graph by linear fitting. The parameter $B = \frac{dH}{I} \sim \frac{dH_{SHE}}{j_e}$ can be recalculated into $\frac{dH_{SHE}}{j_e}$ by dividing it on the sample area S, for rectangular sample and current contacts. If the sample and current contacts have different shapes[37], COMSOL simulations are used to calculate the current density. Equation (5.9) characterizes the "effective" spin Hall angle measured directly in the experiment. However, the "effective" spin current that diffuses into a ferromagnet is smaller than, the actual spin current generated in Pt layer. This is due to the interface transparency[60] which is not equal to 100 % in our case. The interface transparency T can be calculated as follows[61]:

$$T = \frac{G^{\uparrow\downarrow} tanh\frac{d}{2\lambda}}{G^{\uparrow\downarrow} coth\frac{d}{\lambda} + \frac{\sigma_{Pt}}{\lambda}\frac{h}{2e^2}} \tag{5.10}$$

$$G^{\uparrow\downarrow} = G_{eff}\frac{\frac{\sigma_{Pt}}{\lambda}\frac{h}{2e^2}}{\frac{\sigma_{Pt}}{\lambda}\frac{h}{2e^2} - G_{eff}} \tag{5.11}$$

where σ_{Pt} is the conductivity of Pt, λ the spin diffusion length, h the Planck constant and G_{eff} the effective spin mixing conductance see (5.7). The actual or "intrinsic" spin Hall angle is normalized to the interface transparency $\theta_{int} = \frac{\theta}{T}$. The measurements results are summarized in the table below.

Quadratic part of the polynomial A	0.0123 mT/mA^2
Linear part of the polynomial B,	0.0142 mT/mA
Polynomial offset $C \equiv dH_0$	0.39 mT
Spin Hall angle, θ	0.026
Interface transparency T	0.18
Intrinsic spin Hall angle, $\theta_{in} = \theta/T$	0.141

As is seen, the SHE contribution to the FMR linewidth is overwhelmed by the heat. To increase the spin pumping different methods of Pt growth on YIG are studied. Initially one piece of YIG film is cut into 3 pieces. Then, the Gilbert damping parameter is measured for each of them. Then 10 nm of Pt is grown on each of them with thermal evaporation, molecular beam epitaxy (MBE) and sputtering techniques. Finally, the damping parameter is measured again for each sample. The results are presented in Fig 5.4.2.

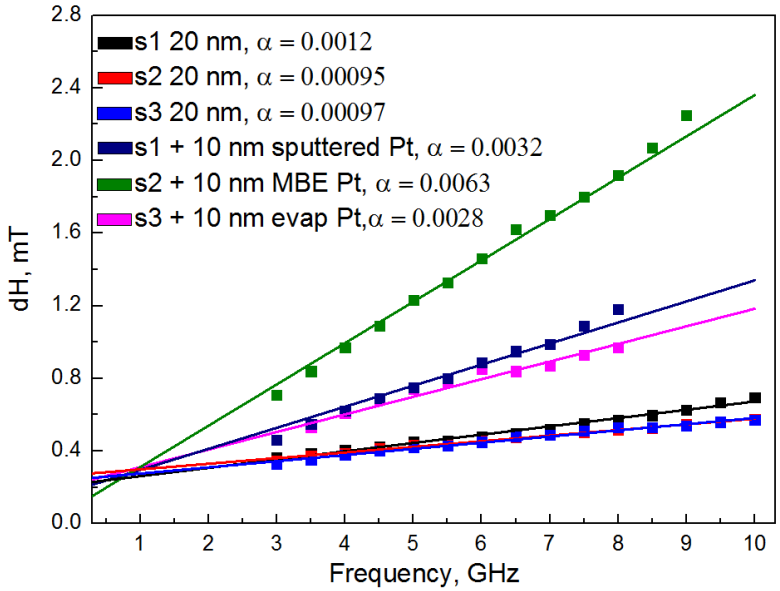

Fig 5.4.2 Measurements of the damping parameter of YIG 20 nm / Pt 10 nm sample for different Pt deposition methods. Evaporated and sputtered Pt/YIG have approximately the same value of damping. MBE grown Pt/YIG has a much larger Gilbert damping parameter.

These results show that the best choice for the SHE measurements is the MBE grown Pt. For the next measurement, 9 nm Pt layer is deposited on the 30 nm YIG film by MBE. Results of the SHE measurements for this sample are shown in the figure below.

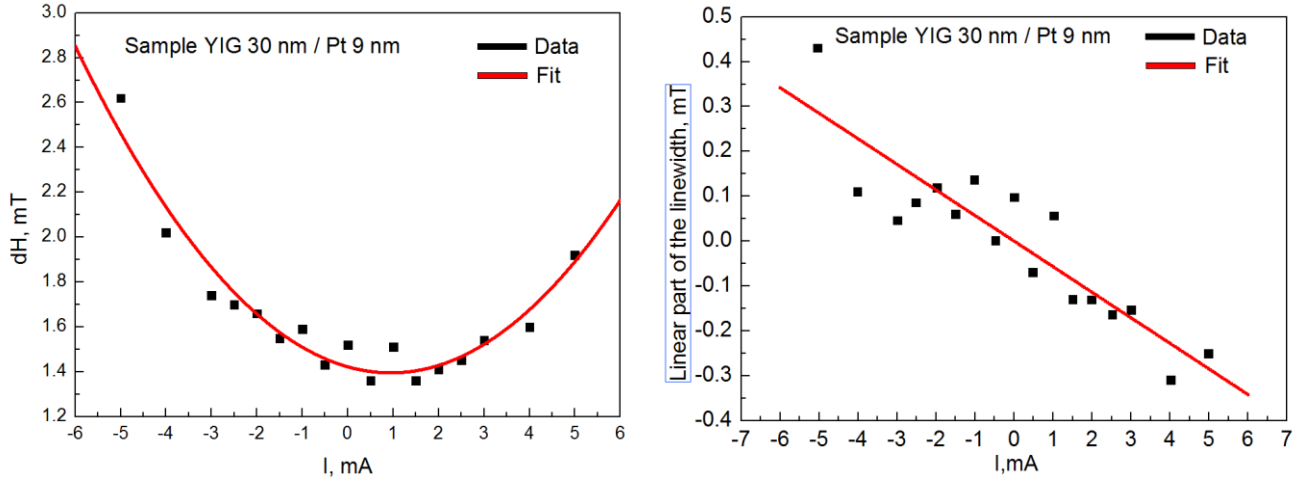

Fig 5.4.3 Measurement of the SHE on the 30 nm YIG with 9 nm of the MBE grown Pt. The linear part of the parabola is significantly larger which makes the curve more asymmetric.

The fit of the dependence with second order polynomial and calculations of the Spin Hall angle are provided in the table below.

Quadratic part of the polynomial *A*	0.03 mT/mA^2
Linear part of the polynomial *B*,	0.057 mT/mA
Polynomial offset $C \equiv dH_0$	1.42 mT
Spin Hall angle, θ	0.088
Interface transparency *T*	0.57
Intrinsic spin Hall angle, $\theta_{in} = \theta/T$	0.152

The measured value of the spin Hall θ angle is much larger than in the previous case. Its value is consistent with the values reported in literature. The intrinsic spin Hall angle is approximately the sample as in the case of the evaporated Pt. Its value is also close to the reported values[56]. Unfortunately, the heat contribution is still very high. The last attempt to get rid of the heating is measuring in the pulsed current mode.

5.5 Spin Hall effect measurements in the pulsed current mode

The idea of the experiment is very simple. Switching from the DC current to current pulses allows reducing the heat formation. To realize the measurements in the pulsed current mode we use a current source that can be triggered by external signal. In our MOKE setup the oscilloscope is triggered by the laser. This triggering signal is splitted into 2 parts. The first part triggers the oscilloscope and the second part triggers the current generator. Thus, the current pulses become synchronized with the probing laser pulse. The laser repetition rate is 80 MHz which means that the new pulse arrives every 12.5 ns. The minimum width of the current pulse wherein it retains a rectangular shape is 2 ns. Thus, the maximum duty cycle that can be reached in our experiment is 6.25. Unfortunately, this value is small and probably is not enough to reduce the heat contribution significantly. Another problem is the impedance mismatch. The output of the current generator is matched to 50 ohm. The resistance of the film is 86 ohm. That means that some part of the applied current will be reflected back to the current generator. This complicates the calculation of the exact current density flowing through the sample. Results of the measurements are presented in the figure below. We do not fit this dependence since we can not convert the applied voltage into a current.

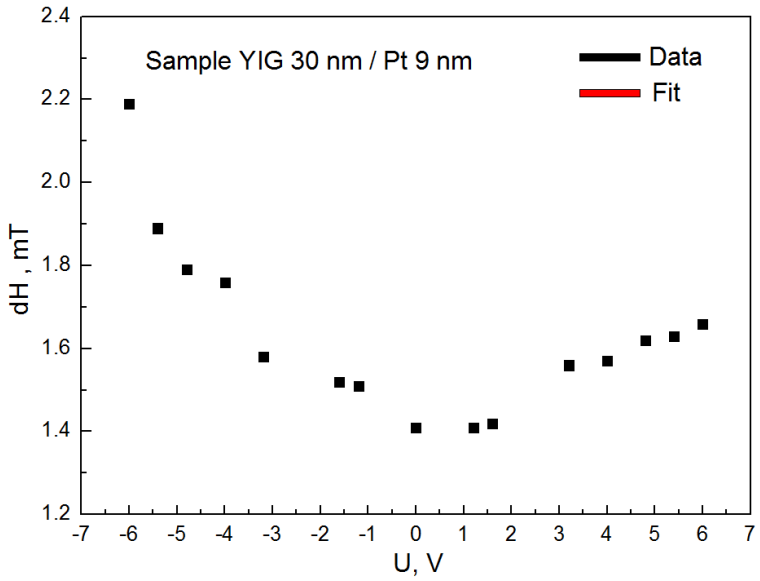

Fig 5.5.1 Measurement of the SHE in a pulsed mode. The parabolic dependence becomes even more asymmetric.

As expected we are not able to reduce the heating contribution significantly.

5.6 Spin Hall effect measurements of the thick LPE YIG, with a cavity method

In this sub-chapter experimental data measured using the cavity setup is presented. These measurements were performed in the University of Kiev. YIG films with thicknesses of 2 μm are grown on GGG by LPE. Thereafter, Pt with thickness of 13 nm was evaporated on top of the films. For comparison measurements 40 nm Ag film was grown on another YIG film of the same thickness. The cavity is adjusted on the frequency of 9200 MHz. The microwave pulse with pulse width is 300 microseconds and the current pulse width is 50 microseconds. The duty cycle is 10000 to reduce the heating effects. The Q-factor of the unloaded cavity is 300 and the input power is 21 dB.

Results of the cavity reflected power on the current amplitude are shown in the figure below

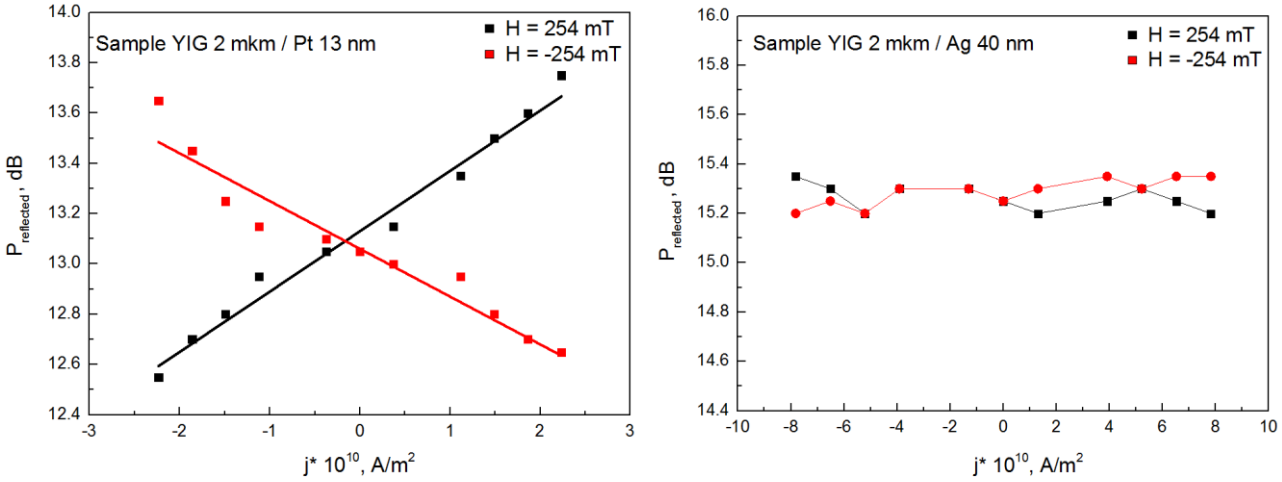

Fig 5.6.1 Dependence of the cavity reflected power on the applied current for different bias field polarities. As expected, no effect is observed for the YIG/Ag sample, since Ag has small spin-orbit coupling.

The cavity reflected power can be recalculated in the relative Gilbert damping change due to SHE (α_{SHE}).

$$\pm\alpha_{SHE} = \frac{4\pi\gamma M_0}{\omega_{res}} \frac{V_f}{V_c} \left(\frac{Q_0 Q_{FMR(I\pm)}}{(Q_{FMR(I\pm)} - Q_0)} - \frac{Q_0 Q_{FMR}}{(Q_{FMR} - Q_0)} \right) \tag{5.12}$$

where M_0 is the saturation magnetization, γ the gyromagnetic ratio, ω_{res} the resonance frequency, V_f the volume of the ferromagnetic , V_c the volume of the cavity, Q_0 the Q-factor of the unloaded cavity. $Q_{FMR(I\pm)}$ and Q_{FMR} are the Q-factor of the cavity in FMR with and without applied current.

$$Q_{FMR} = Q_0 \frac{\sqrt{P_{inp}} - \sqrt{P_{refl\,0}}}{\sqrt{P_{inp}} + \sqrt{P_{refl\,0}}} \frac{\sqrt{P_{inp}} + \sqrt{P_{refl\,FMR}}}{\sqrt{P_{inp}} - \sqrt{P_{refl\,FMR}}} \quad (5.13)$$

$$Q_{FMR(I)} = Q_0 \frac{\sqrt{P_{inp}} - \sqrt{P_{refl\,0}}}{\sqrt{P_{inp}} + \sqrt{P_{refl\,0}}} \frac{\sqrt{P_{inp}} + \sqrt{P_{refl\,FMR(I)}}}{\sqrt{P_{inp}} - \sqrt{P_{refl\,FMR(I)}}} \quad (5.14)$$

$P_{refl\,FMR(I)}$ and $P_{refl\,FMR}$ are reflected cavity power with and without current application, measured in the experiment. P_{inp} is the input power and $P_{refl\,0}$ the cavity reflected power at zero bias field. The detailed derivation of the equations (5.12-5.14) is given in the Appendix. The change of the Gilbert damping due to SHE is shown in figure below.

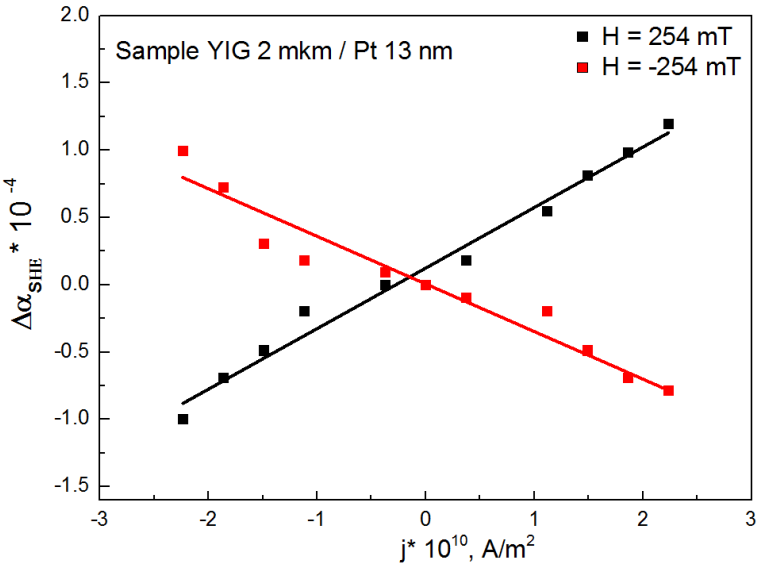

Fig 5.6.2 Dependence of the SHE based Gilbert damping term on the applied current density.

As it can be seen, the dependence of the damping term created by SHE has linear dependence on the applied current. This means that it is possible to exclude heat contribution even for very bad heat sink such as GGG. The only condition to be fulfilled is very high ($\approx 10^4$) duty cycle of the current pulses. Another important conclusion is that the heating of the YIG film occurs on rather large timescales. In the MOKE experiments we worked with 2ns current pulse running through the Pt film every 12.5 ns. Despite the current pulse width was rather small the heating effects were significant. In the cavity measurements the current pulse width is 50 μs but the heating contribution is negligibly small.

From the dependence (5.6.2) and equation (5.9) the spin Hall angle is calculated for two bias field polarities.

$$\theta = \frac{j_s}{j_e} = \frac{t\mu_0 M_s e\left(2H_{bias} + M_{eff}\right)}{\hbar}\frac{\Delta\alpha_{SHE}}{j_e} \qquad (5.15)$$

The obtained values are $\theta_+ = 1.09$ and $\theta_- = 0.86$. These results are not consistent with real values of the spin Hall angle. The reason for that is that the cavity method gives accurate results only when the electromagnetic field perturbations inside of the cavity are small. Apparently in case of thick YIG the condition of the small field perturbation is not fulfilled. YIG has a very high magnetic susceptibility and in the FMR it absorbs electromagnetic field shifting position of the electromagnetic field node from the cavity rare wall. More detailed explanation of inaccuracies of this method can be found in Appendix.

Despite the fact that these measurements don't allow us to calculate exact value of the spin Hall angle, observed effect is obviously tailored to the SHE. The key arguments are the absence of the effect on YIG/Ag films and of the sign change of the damping term for different bias field and current polarities for Pt film.

Conclusions

Broad study of magnetic properties of YIG films is performed. This thesis covers the whole path from YIG sample growth to characterization of magnetization dynamics. In the sub-chapter 5.1, full magnetic characterization of the thin sputtered YIG films is given. A batch of YIG samples with thicknesses of 19, 29, 38 and 49 nanometer is grown by magnetron sputtering for the spin waves experiment. The thickness and the surface roughness are controlled by XRR and AFM measurements. The obtained sample thickness differs by the value of about 1 nm from the planed sample thickness which means that the growth process is well established. Saturation magnetization of the samples is measured by SQUID. The value for the thickest 49 nm sample is 163 mT which is very close to the bulk value (175 mT). With decrease of the sample thickness the saturation magnetization drops up to 99 mT for 19 nm sample. We performed the FMR measurements of the samples to determine the Gilbert damping parameter. The Gilbert damping is 0.00024 for 49 nm sample and grows up to 0.0008 for 19 nm sample. Such dependence of the damping on the sample thickness is typical for the systems were two magnon scattering is a dominant relaxation mechanism. These values of damping are bigger than the values of the Gilbert damping reported in the literature for the samples grown by PLD and LPE techniques. Dependence of the resonance frequency on the resonance field is measured to determine the effective magnetization and subsequently to calculate the anisotropy constant. Our samples possess rather large out-of plane anisotropy which is the evidence of a good crystalline structure. Despite large Gilbert damping the samples are proper for spin waves measurements.

In sub-chapter 5.2 results of the spin wave measurements are provided. We performed TR-MOKE imaging of the spin waves in thin YIG films and extracted the mode structure of the spin waves. For quasi single mode excitation we were able to fit the SW decay with a damped oscillator function providing us with information about the attenuation length in the thin YIG film structures for the first spin wave mode. MUMAX simulations were performed to compare experimental and simulated modes. The MOKE data is in a very good agreement with these simulations. The physical origin of long propagating „edge modes“ is revealed during the measurements. The reason is the microwave current flowing in Ti/Au capping of the YIG film. This current is excited inductively by the CPW. Measurements of the spin wave attenuation length showed that the spin waves propagate as if the Gilbert damping is much higher ($\alpha \approx 0.002$) than measured for pure YIG. This occurs due to the presence of the spin pumping at the YIG/Ti interface. To check this, comparative measurements of spin wave

propagation on stripes capped with Ti/Au and Aluminum are performed. For Al capped films the decay length increases by roughly a factor of 2. These results make sense since the spin pumping should much smaller for such light metal as Al.

To make a double check of this hypothesis the separate measurements of the spin pumping at the YIG/Ti interface were performed. We measured the Gilbert damping on the YIG/Ti, YIG/AlOx/Ti, YIG/Au and YIG/AlOx/Au samples with FMR technique. Enhanced Gilbert damping with the value $\alpha = 0.0021$ is observed only in case of YIG/Ti interface. This confirms our hypothesis about the spin pumping. We calculated the spin-mixing conductance for YIG/Ti films. Obtained value is $4.1*10^{17}$ m^{-2} which is approximately three times smaller than for YIG/Pt interfaces.

We also studied the dependence of the Kerr signal on the thickness of the reflecting capping layer on top of the YIG film to find the optimal thickness for MOKE experiments. The optimal thickness lies in range between 6 and 10 nm. The unexpected result is that we are able to see the spin waves through rather thick (about 40 nm) Au layer. The question arises whether we probe directly the spin waves in YIG film with the laser through a thick metal layer, or it is a spin accumulation signal in Au layer created by the spin pumping from YIG film. This might become an object of the further study.

In sub-chapter 5.4 results of the spin Hall measurements are provided. Dependence of the FMR linewidth on the applied current has a form of asymmetric parabola. This is due to heating effects caused by the current running through the Pt films. Unfortunately, GGG substrate is a very bad heat sink which makes direct observation of the linear, spin Hall - based contribution rather difficult. Nevertheless we are able to extract linear part from parabolic dependence which is proportional to the spin Hall angle. For 30 nm YIG sample with 12 nm evaporated Pt film the value for the spin Hall angle is 0.026. The reason why the measured value is small is a very low interface transparency (T= 0.18). The intrinsic spin Hall angle is 0.141 correspondingly. This result is consistent with the values reported in literature. To improve the interface transparency we studied spin pumping of Pt films grown by different methods. MBE grown Pt turned out to be the best choice since it shows the largest spin pumping. For 30 nm YIG sample with 9 nm of MBE grown Pt the value of the spin Hall angle is 0.088. The interface transparency is indeed larger (0.57) and the value of the intrinsic spin Hall angle is 0.152. As expected the intrinsic value of the spin Hall angle is approximately the same for both experiments.

The attempt was made to reduce the heating by switching to the pulsed mode. Unfortunately, the MOKE experimental setup does not allow us to work with pulse duty cycle larger than 10. The pulsed mode measurements show that heat contribution still has a dominant influence on FMR linewidth.

The SHE effect measurements gave us correct values for the spin Hall angle. Unfortunately, they also showed that the sputtered YIG on GGG can not be considered as a candidate for auto oscillations measurements due to its large Gilbert damping and accumulation of the heat in the area of the current flow.

In sub-chapter 5.6 we show results measured with microwave cavity on thick LPE grown YIG. The cavity method gives accurate results only in the approach of weak electromagnetic field perturbation inside of the cavity. In our case the sample volume was to large, which made the accurate calculation of the spin Hall angle impossible. Nevertheless the observed effect is definitely tailored to the spin Hall angle. The cavity measurements showed that for very big ($\approx 10^4$) current pulse duty cycles the heating effect is negligibly small. They also showed that the heat that changes the FMR linewidth is accumulated on the large time scale (> 50 μs). The current pulse width is 50 μs and there is no measurable heating influence on the damping.

Appendix

CPW-FMR experimental setup

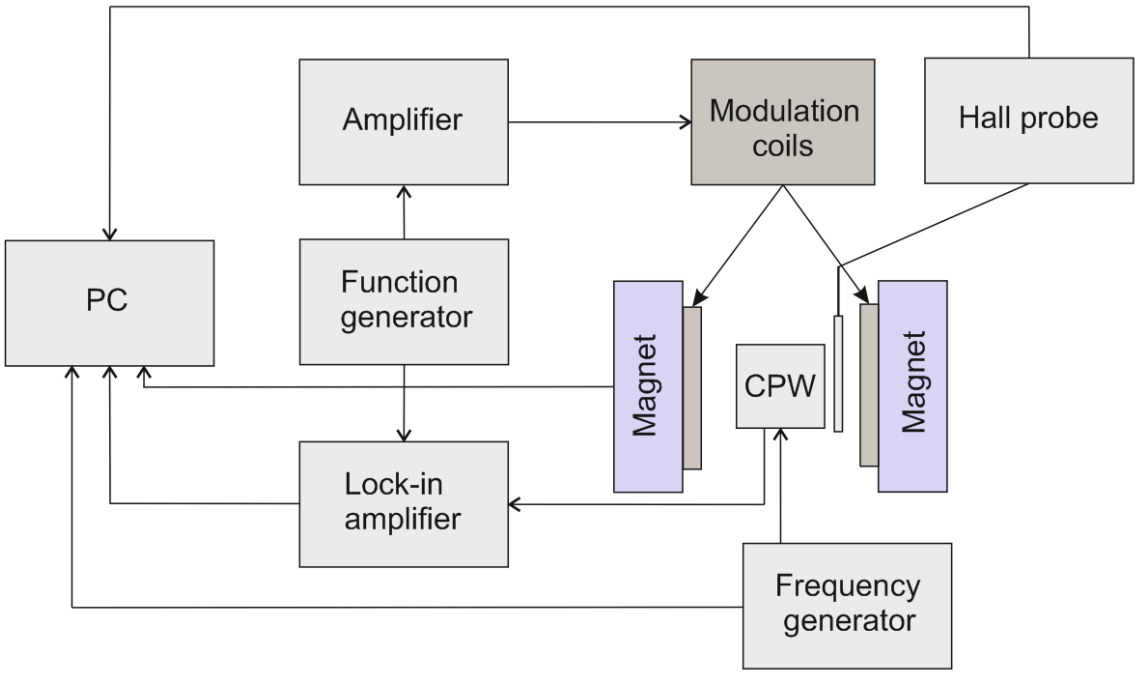

Fig 1 Block-diagram of CPW-FMR experimental setup.

The input rf-signal is created by the Anritsu frequency generator (0-20 GHz) and goes directly to the CPW (see Fig 4.1.2). The transmitted signal comes to the diode-based detector on the input of the Lock-in amplifier. The detector converts rf-power to volts, so that it can be measured by the Lock-in. To use Lock-in technique we modulate the magnetic field by using internal modulation coils. The modulation frequency is set by function generator and its value is 86 Hz. Since the function generator can not supply sufficient current the amplifier is used to increase the current in coils. The field is measured by the Hall probe placed near the experimental section. The Lock-in, frequency generator and magnet power supply are connected to the PC. The Labview program controls the measurement process and saves all the data to the hard drive.

Cavity-FMR experimental setup

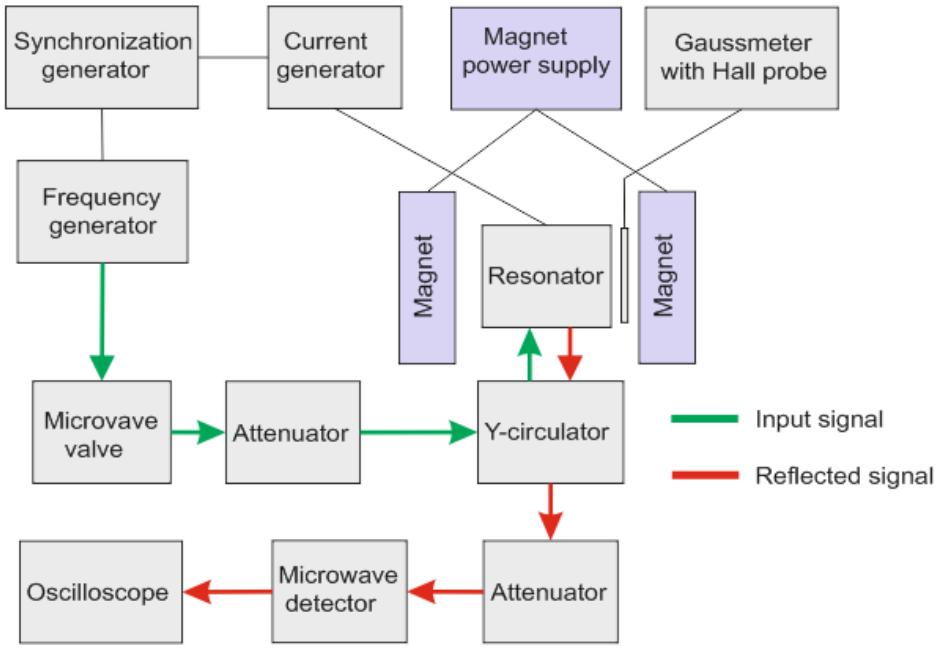

Fig.4.1.3 Block diagram of the FMR setup with resonator. Green and red arrows indicate the root of the input and the reflected microwave signal.

The microwave signal is created by the frequency generator which works in the range (4-16 GHz). The next element in the input signal tract is a microwave valve that protects the input of the generator from the reflected signals. After the valve, comes an attenuator to control the power that enters the cavity. From the attenuator the signal goes to the Y-circulator that separates the input signal from the reflected signal. Then the signal enters the resonator where the YIG sample is placed. The reflected signal already carries the information about the processes in the resonator. After the Y-circulator the signal goes to another attenuator, then to the microwave detector where it is converted to the voltage. The converted signal is read by the oscilloscope. For the SHE measurements the current through the Pt film is applied. This current pulse is created by the current generator. To reduce heating of the Pt film the measurements are performed in the pulsed mode. Both frequency and current generators are synchronized by the external synchronization generator. The resonator with the experimental sample is placed inside the magnet. The field is measured by the Gaussmeter with Hall-probe.

MOKE experimental setup

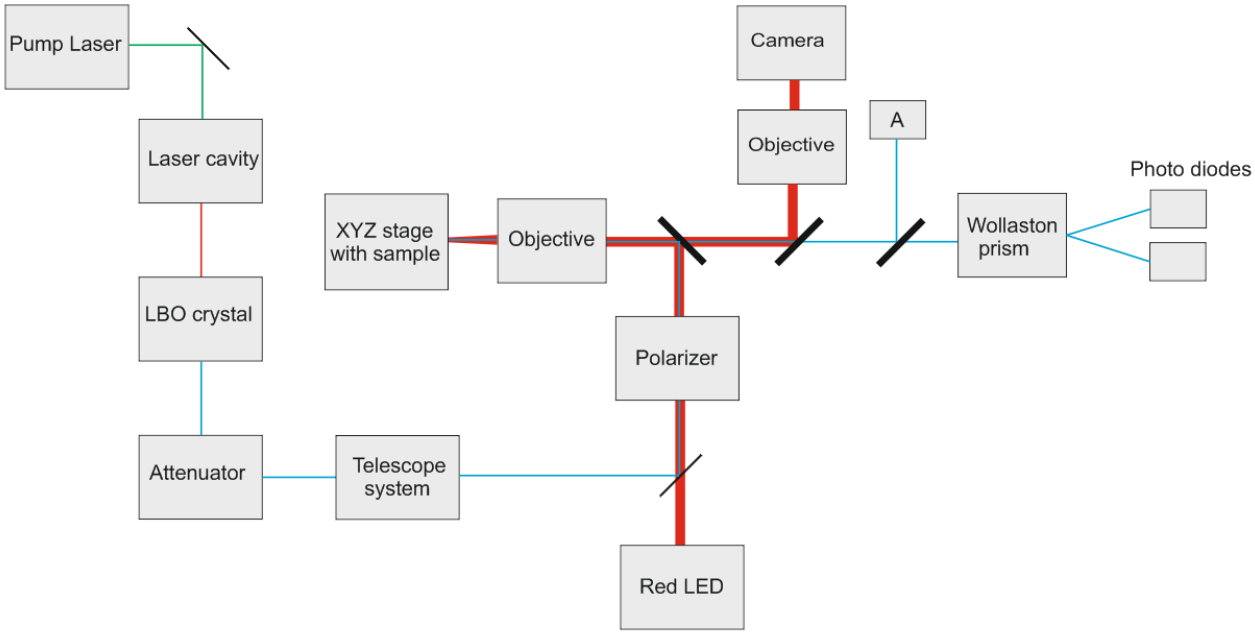

Fig 4.2.2 The block diagram of the optical part of the MOKE experimental setup.

The beam is generated in the pump system with wavelength of 532 nm. Having reflected several times it enters the cavity. Leaving the cavity the laser becomes a mode-locked with pulse width of 100 fs, repetition rate of 80 MHz and with wavelength of 830nm. From the cavity the light goes the Lithium Triborate crystal for frequency doubling. This is done to increase the spatial resolution by a factor of two and to increase the Kerr rotation. After the crystal the wavelength is $\lambda = 415$ nm. The next element is an attenuator system which consists of 2 sets of semi-transparent glasses. In each set glass attenuation can be varied from 4% to 250 %. The maximum attenuation for the beam is 625% correspondingly. Following the attenuator there is a telescope system used to control the size of the laser spot that goes to the objective. It consists of two lenses of different sizes. The distance between two lenses is equal to the sum of the focus distances of the lenses. The parallel beam is focused by the first lens and gathered in the spot in the focus distance. Then it enters the second lens. The outgoing beam is parallel to the main optical axis. However, if we slightly change the position of the second lens the outgoing beam becomes convergent or divergent depending on the direction of the shift. This results in increase or decrease of the beam diameter. Thereafter, the beam goes to the pellicle mirror that reflects it towards the polarizer.

From the rear side of the mirror the red light from the LED with wavelength λ = 600 nm enters the system. This light is needed for illumination of the sample, alignment and stabilization purposes. After the polarizer linearly polarized light enters the microscope. The objective focuses it on the sample surface. The sample is placed on the stage that allows moving the sample in XYZ directions. In the process of MOKE imaging, all the adjustments are kept unchanged except the position of focused beam on the sample surface. The topography of the sample is recorded by scanning a small area of the sample and measuring the reflected signal which is proportional to the reflectivity of the surface. The reflected laser beam together with the LED light goes back through the microscope to the pellicle mirror and then to the dichroic mirror. The dichroic mirror reflects the red LED light towards the camera and transmits the blue light of the laser. The camera is used for image stabilization program. The program saves the reference image of the sample surface and constantly compares it with the current images, adjusting the stage in such a way, that the images are closer to the reference. Thus, the setup is protected from the random shifts of the scanning position. The blue light goes further to almost transparent mirror that reflects a small part to the photodiode A, to measure the sum signal. The biggest part of the beam goes further to the Wollaston prism that splits the beam into the two orthogonal polarized components. Each component is detected by a separate photodiode B and C. The signal from each diode goes to the electronic circuit that outputs the voltage proportional to $(U_B - U_C)/ U_A$. The Wollaston prism is adjusted in the way, that the amplitudes of the signals on the diodes B and C are equal if the m_Z component of magnetization on the sample is absent. In this case the difference signal measured by lock-in is zero. The rotation of the polarization by θ_k leads to a non-zero difference signal. The difference signal is divided by a sum signal measured on diode A in order to make the measurement independent from the input laser power.

Microwave damping measurement with cavity method

In this experiment we measure reflection parameter Γ defined as $\Gamma^2 = \frac{P_{reflected}}{P_{input}} = \frac{P_{input}-P_{absorbed}}{P_{input}}$.

Reflection parameter can be also defined through Q-factor of the cavity and coupling coefficient of the cavity with the microwave tract[62].

$$\Gamma = \frac{2\beta}{\beta + 1 + i2Q_0\delta} - 1 \quad (1)$$

where $\beta = \frac{Q_0}{Q_{coupling}}$ – coupling parameter, Q_0 – Q–factor of the cavity, $\delta = \frac{\omega-\omega_0}{\omega}$ – cavity detuning factor , ω_0– resonance frequency of the cavity, ω – frequency of the input signal. This equation is fulfilled for the high Q-factors, $Q_0 \gg 1$. In our case the Q-factor of the cavity is 300.

$$\Gamma^2 = \frac{(\beta-1)^2 + 4Q_0\delta^2}{(\beta+1)^2 + 4Q_0\delta^2} \quad (2)$$

Equations 1 and 2 are valid for the empty cavity or for the cavity with a small ferromagnetic sample ($V_{Ferromagnet} \ll V_{Cavity}$) without applied magnetic field. If magnetic field is applied the system gets the magnetic susceptibility $\chi = \chi' + i\chi''$, due to the presence of the ferromagnetic sample. If ferromagnetic sample is attached to the rear wall of the cavity with TE_{110} oscillations type the shift in the resonance frequency and Q-factor of the cavity can be written as follows[12]:

$$\omega_{res} = \omega_0(1 - 4\pi\frac{V_{Ferr}}{V_{cavity}}\chi') \quad (3)$$

$$\frac{1}{Q_{Loaded}} = \frac{1}{Q_0} - 8\pi\frac{V_{Ferr}}{V_{cavity}}\chi'' \quad (4)$$

Here ω_0 and Q_0 are the resonance frequency and Q-factor of undisturbed cavity. χ'' is the imaginary part of magnetic susceptibility obtained from the equation (1.26) .

$$\chi'' = \frac{\gamma\omega\alpha M_0(\omega_{res}^2 + (1+\alpha^2)\omega^2)}{(\omega_{res}^2 - (1+\alpha^2)\omega^2)^2 + 4\alpha^2\omega^2\omega_{res}^2} \quad (5)$$

where $\omega_{res}^2 = \gamma^2 H_{res}(H_{res} + 4\pi M_0)$ is the resonance frequency of the in-plane magnetized film.

As it can be seen from equations (4) and (5) the change of the imaginary part of magnetic susceptibility is tailored to the change of Q-factor which can be measured in our experimental setup. In this experiment all measurements are performed in the ferromagnetic resonance. The FMR condition simplifies equations (3) and (5). Since the real part of magnetic susceptibility χ' is very small in the FMR and the ratio $\frac{V_{Ferr}}{V_{cavity}} < 10^{-6}$ we can neglect the shift of the cavity resonance frequency rewrite equation (3) as

$$\omega_{res} = \omega_0 \tag{6}$$

Equation (5) in the FMR condition becomes also very simple (see equation (1.27)).

$$\chi''_{res} = \frac{\gamma M_0}{2\alpha\omega_{res}} \tag{7}$$

Combining equations (4) and (7) we can calculate the Gilbert damping as follows:

$$\alpha = \frac{\gamma M_0}{2\chi''_{res}\omega_{res}} = \frac{\gamma M_0}{2\omega_{res}} \frac{8\pi Q_0 Q_{FMR} V_f}{(Q_{FMR} - Q_0)V_c} \tag{8}$$

Equation (8) shows the connection between the Gilbert damping of the ferromagnetic film inside of the cavity and Q-factor of the system in FMR. If we start running a current through the Pt film on top of the YIG film the total damping of the system will be changed due to the SHE. This will also result in a change of the resonance Q-factor of the system. In the first approach the heat influence on the magnetization is neglected. Equation (8) can be rewritten as follows:

$$\alpha_I = \alpha \pm \alpha_{SHE} = \frac{\gamma M_0}{2\omega_{res}} \frac{8\pi Q_0 Q_{FMR(I\pm)} V_f}{(Q_{FMR(I\pm)} - Q_0)V_c} \tag{9}$$

The sign $\pm$ means that the SHE can ether increase or decrease the total damping depending on the current polarity. Subtracting equation (8) from equation (9) we will get

$$\pm\alpha_{SHE} = \frac{4\pi\gamma M_0}{\omega_{res}} \frac{V_f}{V_c} \left(\frac{Q_0 Q_{FMR(I\pm)}}{(Q_{FMR(I\pm)} - Q_0)} - \frac{Q_0 Q_{FMR}}{(Q_{FMR} - Q_0)} \right) \tag{10}$$

According to (5.9) the spin Hall angle θ is calculated as follows:

$$\theta = \frac{j_s}{j_e} = \frac{t\mu_0 M_s e\left(2H_{bias} + M_{eff}\right)}{f\hbar} \frac{\gamma d H_{SHE}}{j_e} = \frac{t\mu_0 M_s e\left(2H_{bias} + M_{eff}\right)}{\hbar} \frac{\pm\alpha_{SHE}}{\pm j_e} \quad \Rightarrow$$

$$\theta = \frac{t\mu_0 M_s e\left(2H_{bias} + M_{eff}\right)}{\hbar j_e} \frac{4\pi\gamma M_0}{\omega_{res}} \frac{V_f}{V_c} \left(\frac{Q_0 Q_{FMR(I+)}}{(Q_{FMR(I+)} - Q_0)} - \frac{Q_0 Q_{FMR}}{(Q_{FMR} - Q_0)} \right) \quad (11)$$

Where Q_{FMR} and $Q_{FMR(I+)}$ can be calculated from equation (2).

$$Q_{FMR} = Q_{coupling} \frac{\sqrt{P_{inp}} + \sqrt{P_{refl\,FMR}}}{\sqrt{P_{inp}} - \sqrt{P_{refl\,FMR}}} \quad (12)$$

$$Q_{FMR(I)} = Q_{coupling} \frac{\sqrt{P_{inp}} + \sqrt{P_{refl\,FMR(I)}}}{\sqrt{P_{inp}} - \sqrt{P_{refl\,FMR(I)}}} \quad (13)$$

$P_{refl\,FMR(I)}$ and $P_{refl\,FMR}$ are reflected cavity power with and without current application, measured in the experiment. Parameter $Q_{coupling}$ can be calculated by measuring the cavity reflected power in the absence of magnetic field.

$$Q_{coupling} = Q_0 \frac{\sqrt{P_{inp}} - \sqrt{P_{refl\,0}}}{\sqrt{P_{inp}} + \sqrt{P_{refl\,0}}}$$

We should note that the cavity method gives an accurate result only in case of the weak perturbation of the electromagnetic field inside of the cavity. For instance equations (3) and (4) are derived for the field distribution corresponding TE_{10} mode with the field node on the cavity rear wall. If the sample volume is rather big, in FMR it starts to absorb the electromagnetic field shifting the field node to itself. This might result in a big error in calculations. In all the calculations we considered the term $4Q_0\delta^2$ in equation (2) equal to zero. Indeed in the absence of the magnetic field we adjust the frequency of the cavity exactly on the input signal frequency and the cavity detuning factor δ becomes very small ($\delta < 0.001$). However at FMR the resonance frequency of the cavity changes and the detuning factor δ increases. The value of the frequency shift depends on the amplitude of the FMR. And the amplitude depends on the sample volume. This effect is well known from the general oscillation theory. If we make two oscillators with close frequencies ω_1 and ω_2 to interact with each other, their frequencies will diverge. The figure below is called the Wien graph, illustrates this effect for the coupled oscillator system (cavity-ferromagnetic sphere). When the frequency of the FMR is far from the cavity resonance frequency the system is uncoupled (Both resonances can be simultaneously found in the system).When their frequency values become close to each other the system becomes coupled.

In the coupled state the system oscillates on the frequencies that are different from FMR and cavity resonance frequency.

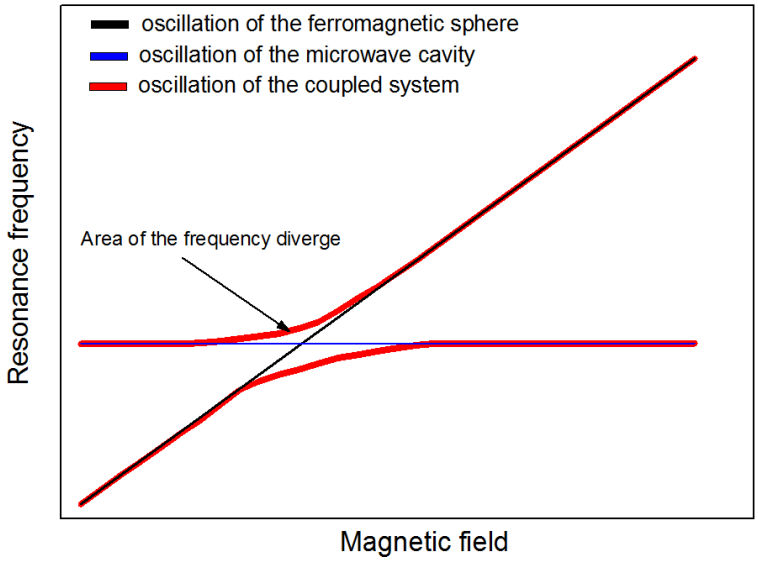

If the coupling is strong (which is most probably the case in our experiment) the cavity frequency shift can not be considered negligible. In that case the cavity detuning factor δ grows and the term $4Q_0\delta^2$ in equation (2) can not be equalized to zero. This can create another inaccuracy in the calculation of reflection coefficient.

Acknowledgment

I especially want to thank the following people:

• Prof. Christian Back for giving me the opportunity to write my PhD-thesis under his supervision at the University of Regensburg, having regular discussions of the obtained results and help with experiments planning. I have appreciated friendly and in the same time work motivating atmosphere created in his department. I am especially grateful to him for showing a lot of patience during reading and correcting numerous mistakes in the paper and in this thesis.

• Prof B.J. Hickey from the University of Leeds for good organization of the Spinicurr project, that allowed me to travel in the best European labs and always to learn something new. I appreciated his help with the paper and other assistance during my secondment in Leeds. Special thanks to Arpita Mitra for her introduction to the sputtering facility and for supply of YIG samples during all 3 years. Special thanks to Georgeous Stefanou for his help with X-Ray and VSM measurements and just for hospitality during my visits in Leeds.

• Prof G. Melkov , Y. Koblyansky , V. Malyshev and D. Bozhko from Kiev for their collaboration in Spin Hall effect experiments. Very big thanks to Prof G.Melkov who managed to consult me despite being extremely busy with his own P.h.D students.

• Martin Decker for investing enormous amount of time to give a comprehensive help in all the possible aspects, starting from sample preparation and ending with evaluation of experimental data. I greatly appreciate his help with planning of the experiments and discussion of the results. Special thanks for assistance during MOKE measurements and occasional help with bonder facility. I am grateful to him for being patient and deep thinking advisor for all this 3 years.

• Anatoly Shestakov for fruitful discussion of physical aspects, help with experimental section fabrication and with AFM.

• Johannes Stigloher for his help with MUMAX simulations and assistance during MOKE measurements.

• Dr Matthias Kronseder for growing the samples for spin waves and spin Hall measurements in the MBE chamber.

• Jean-Yves Chauleau and Martin Obstbaum for giving me introductions to different sample preparation facilities.

• Helmut Körner for SQUID measurements and comments to the paper.

• Markus Härtinger for fruitful discussions of the FMR results and theory of spin pumping.

• Markus Hollnberger for his help with designing a sample holder for MOKE experiment.

• Prof D.Weiss for giving me access to the clean room facilities.

• People from the chair of Christian Back for their nice attitude and for the feeling of being welcome in the group. I enjoyed all the time of my stay in Regensburg and I am glad to be a member of this great team. I am grateful for advices and tips you gave to me in the group meetings.

7. Bibliography

[1] R.W. Wood, A. Ellett, Phys. Rev. **24**, 243, (1924)

[2] J. Brossel, A. Kastler, C. R. Hebd. Acad. Sci. **229**, 1213, (1949)

[3] J. S. Moodera, L. R. Kinder, T. M. Wong et al., *Phys. Rev. Lett*. **74**, 3273–3276, (1995);

[4] T. Miyazaki and N. Tezuka,, *J. Magn. Magn. Mater*. **139**, L231–L234, (1995).

[5] Kato, Y. K., S. Mahrlein, a. C. Gossard, and D. D.Awschalom, 2004b, *Science* (80-.). **306** (5703), 1910.

[6] Wunderlich, J., B. Kaestner, J. Sinova, and T. Jungwirth,2004, *cond-mat*/0410295

[7] Saitoh, E., M. Ueda, H. Miyajima, and G. Tatara, 2006, *Appl.Phys. Lett*. **88**(18), 182509.

[8] Zhao, H., E. Loren, H. van Driel, and A. Smirl, 2006, *Phys.Rev. Lett*. **96**(24), 246601.

[9] Valenzuela, S. O., and M. Tinkham, 2006, *Nature* **442**(7099),176.

[10] Ando, K., S. Takahashi, K. Harii, K. Sasage, J. Ieda, S. Maekawa, and E. Saitoh, 2008, *Phys. Rev. Lett*. **101**(3), 036601.

[11] O. d'Allivy Kelly,A. Anane,R. Bernard,J. Ben Youssef,C. Hahn,A H. Molpeceres,C. Carrétéro,E. Jacquet,C. Deranlot,P. Bortolotti,R. Lebourgeois,J.-C. Mage,G. de Loubens,O. Klein,V. Cros and A. Fert, *Appl. Phys. Lett*.**103**, 082408, (2013)

[12] A.G. Gurevich and G.A. Melkov, Magnetization oscillation and waves. *CRC Press*, 1996.

[13] K. Uchida, T Kikkawa, A Miura, J Shiomi, and E Saitoh, *Phys.Rev*. **X4**, 041023, (2014)

ISBN 9780849394607

[14] Kajiwara et al, *Nature* **464**, 262-266, (2010)

[15] M. C. Onbasli, A. Kehlberger, D. H. Kim, G. Jakob , M. Kläui , A. V. Chumak, B. Hillebrands and C. A. Ross, *APL Mater*. **2**, 106102, (2014)

[16] O. d'Allivy Kelly, A. Anane, R. Bernard, J. Ben Youssef, C. Hahn, A H. Molpeceres, C. Carrétéro, E. Jacquet, C. Deranlot, P. Bortolotti, R. Lebourgeois, J.-C. Mage, G. de Loubens, O. Klein, V. Cros and A. Fert, *Appl. Phys. Lett*. **103**, 082408, (2013)

[17] B Heinrich, C. Burrrowes, E. Montoya, B. Kardasz, E. Girt, Young-Yeal Song, Yiyan Sun and Mingzhong Wu *Phys.Rev.Lett* **107**,066604, (2011)

[18] Yiyan Sun, Young-Yeal Song , Houchen Chang ,Michael Kabatek , Michael Jantz , William Schneider, Mingzhong Wu, Helmut Schultheiss and Axel Hoffmann, *Appl. Phys. Lett*. **101**, 152405, (2012)

[19] Yiyan Sun, Houchen Chang, Michael Kabatek, Young-Yeal Song, Zihui Wang, Michael Jantz, William Schneider, Mingzhong Wu, E. Montoya, B. Kardasz, B. Heinrich, Suzanne G. E. te Velthuis, Helmut Schultheiss, and Axel Hoffmann *Phys.Rev.Lett* **111**, 106601, (2013)

[20] M. B. Jungfleisch, A. V. Chumak, A. Kehlberger, V. Lauer, D. H. Kim, M. C. Onbasli, C. A. Ross,M. Klaui, and B. Hillebrands, *Phys. Rev B* **91**, 134407, (2015)

[21] Young-Min Kang, Sung-Hun Wee, Seong-Il Baik, Seong-Gi Min, Seong-Cho Yu, Seung-Hyun Moon, Young-Woon Kim and Sang-Im Yoo , J. *Appl. Phys*.**97**, 10A319,(2005)

[22] Tao Liu, Houchen Chang, Vincent Vlaminck, Yiyan Sun, Michael Kabatek, Axel Hoffmann, Longjiang Deng and Mingzhong Wu, *J. Appl. Phys*. **115**, 17A501, (2014)

[23] S. R. Marmion, M. Ali, M. McLaren, D. A. Williams, and B. J. Hickey *Phys. Rev. B*. **89**, 220404, (2014)

[24] Sclömann E, *Sol.state.physics* , **3,** p 322, (1960)

[25] L.R. Walker , *Phys Rev* , **105,** p 390, (1957)

[26] Damon R W,Eshbach J R, *J. Phys.Chem.Sol* ,**19,** 308, (1961)

[27] Mizukami, S., Y. Ando, and T. Miyazaki, 2001, J. *Magn. Magn. Mater*. **230**, 1640

[28] Mizukami, S., Y. Ando, and T. Miyazaki, 2002, *Phys. Rev. B*,**66**(10), 104413.

[29] Urban, R., G. Woltersdorf, and B. Heinrich, 2001, *Phys. Rev.Lett*. **87**(21), 217204

[30] Tserkovnyak, Y., A. Brataas, and G. E. W. Bauer, 2002a, *Phys. Rev. Lett*. **88**(11), 117601.

[31] Tserkovnyak, Y., A. Brataas, and G. E. W. Bauer, 2002b, *Phys. Rev*. B **66**(22), 224403

[32] Tserkovnyak, Y., A. Brataas, and B. I. Halperin, 2005, *Rev. Mod. Phys*. **77**(October), 1375.

[33] Brouwer, P. W., 1998, **58**(16), 135.

[34] Buttiker, M., H. Thomas, and A. Pretre, 1993, *Phys. Rev.Lett*. **70**(26), 4114.

[35] A Bratas, Y Nazarov, and G Bauer , *The European Physical Journal B - Condensed Matter and Complex Systems* **22**, p. 99.(2001)

[36] M. Dyakonov. *Physical Review Letters*, **99**:126601, (2007)

[37] M. I. Dyakonov. Spin Hall Effect. *eprint arXiv:*, 1210.3200, (2012).

[38] Nagaosa, N., J. Sinova, S. Onoda, A. H. MacDonald, and N. P. Ong, *Rev. Mod. Phys*. **82**(2), 1539 (2010).

[39] Mott, N. F., *Proc. R. Soc. A Math. Phys. Eng*. Sci.124(794), **425**.(1929)

[40] Mott, N. F., Proc. R. Soc. *A Math. Phys. Eng*. Sci.135(827), **429**. (1932)

[41] M.I. Dyakonov, *Spin Physics in semiconductors* (2008)

[42] Smit, J., 1955, *Physica _Amsterdam_* **21**, 877

[43] Smit, J., 1958, *Physica _Amsterdam_* **24**, 39

[44] Berger, L., 1970, *Phys. Rev. B* **2**, 4559.

[45] G. Y. Guo, Y. Yao, and Q. Niu, Phys. Rev. Lett. 94, 226601, (2005).

[46] Nagaosa, N., J. Sinova, S. Onoda, A. H. MacDonald, and N. P. Ong, 2010, *Rev. Mod. Phys*. **82**(2), 1539.

[47] Haldane, F. D. M., 2004, *Phys. Rev. Lett*. **93**, 206602.

[48] Wang, X., D. Vanderbilt, J. R. Yates, and I. Souza, 2007, *Phys.Rev. B* **76**, 195109.

[49] Guo, G., S. Murakami, T.-W. Chen, and N. Nagaosa, 2008,*Phys. Rev. Lett*. **100**(9), 096401.

[50] J. E. Hirsch. Spin Hall Effect. *Physical Review Letters*, **83**:1834, 1999.

[51] J. C. Slonczewski, J. *Magn. Magn. Mater*. **159**, L1 (1996).

[52] S. Petit et al., *Phys. Rev. Lett*. **98**, 077203 (2007).

[53] L.Liu, T. Moriyama, D.C. Ralph and R.A. Buhrman *Phys Rev Lett* **106**, 036601 (2011)

[54] A. Vansteenkiste, J. Leliaert, M. Dvornik, M. Helsen, F. Garcia-Sanchez, and B. Van Waeyenberge, *AIP Adv*.**4**, 107133 (2014).

[55] Z. Qiu, K. Ando, K. Uchida, Y. Kajiwara, R. Takahashi,H. Nakayama,T. An,Y. Fujikawa,E. Saitoh *Appl. Phys. Lett*. **103**, 092404 (2013)

[56] Z. Wang, Y. Sun, Y Song, M. Wu, H. Schultheiß, J. Pearson and A Hoffman, *Appl Phys Lett* **99**, 162511, (2011)

[57] V. E.Demidov, S. U . Urazhdin, H. Ulrichs, V. Tiberkevich, A. Slavin, D. Baither, G. Schmitz and S. O. Demokritov, *Nature Materials* **11,** (2012)

[58] A.Slavin and V. Tiberkevich, *Phys Rev Lett* **95**, 237201, (2005)

[59] M.B Jungfleisch, W. Zhang, J. Ding, W.Jiang, H.Chang, F.Y. Fradin, J.E. Pearson, J.B. Ketterson, V Novosad, M. Wu and Hoofman. *Phys Rev Lett* **116**, 057601, (2016)

[60] Weifeng Zhang,Wei Han, Xin Jiang, See-Hun Yang and Stuart S. P. Parkin, *Nat Phys*, **11,** 3304, (2015)

[61] H.Jiao, G.Bauer, *Phys. Rev. Lett*. **110,** 217602, (2013).

[62] E.L. Ginzton, *Measurements in the centimeter wave range* (1960)